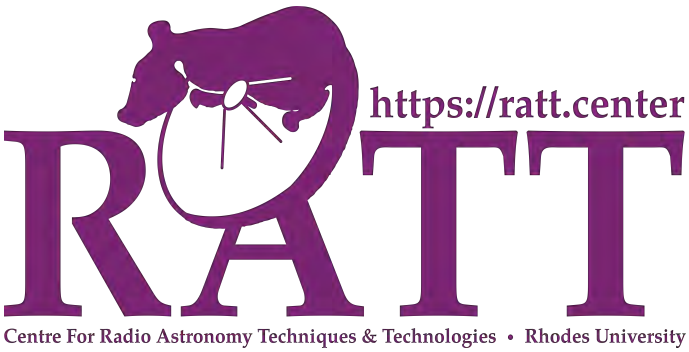


# M3: Mining Mini-Halos with MeerKAT

by

**Keegan Somerset Trehaeven**

Supervised by Prof. Oleg Smirnov and Dr Viral Parekh

*A research project submitted in fulfilment of the academic requirements for the Master of Science degree at the*

*Centre for Radio Astronomy Techniques & Technologies (RATT), Department of Physics & Electronics, Rhodes University*

*Makhanda, Eastern Cape, South Africa*

December 2022

*"Authenticity and Livity"*

*my Brother*

# Abstract

This work aims to showcase the MeerKAT telescope's capabilities and related calibration and imaging software in studying the emission of radio mini-halos. These diffuse radio synchrotron sources surround a Brightest Cluster Galaxy (BCG) in relatively relaxed clusters out to a few 100 kpc in size. They are difficult to image because of their relatively low surface brightness and small angular size. Hence, they could not be studied in great detail by previous generations of radio telescopes and much about their nature, particularly the exact production mechanism, is not yet fully understood.

Thus, for the first time, MeerKAT observed a sample of five galaxy clusters to investigate the central radio mini-halo in each. Studying these sources requires the deepest images generated from the data and the effective subtraction of any projected sources obscuring or contaminating the underlying diffuse emission. Therefore, I describe the data reduction used to create third-generation calibrated, primary beam corrected, point source subtracted Stokes *I* L-band continuum images of these clusters. For first- and second-generation calibration, I use the CARACal pipeline, which implements software optimised explicitly for MeerKAT data. For third-generation calibration, I use the faceted approach of killMS and DDFacet, and then I perform visibility-plane point source subtraction to disentangle the compact and diffuse emissions. I then measured the size, flux density, in-band spectral properties, and radio power of the central mini-halos. I present the first new mini-halo detection by MeerKAT (MACS J2140.2-2339, Trehaeven et al. accepted), the first spectral index maps of these mini-halos, which show very interesting distributions, and a ∼100 kpc

southern extension to the ACO 3444 mini-halo previously unseen in archival VLA data. Thereafter, I present a multi-wavelength case study for two complementary mini-halos from our sample and show via a radio-to-X-ray spatial correlation test that they might be caused by different particle (re)-acceleration mechanisms.

Through these initial science results, I have shown that future observations of radio mini-halos with MeerKAT are an exciting prospect that can lead to a better understanding of the fundamental physics behind these sources.

# Acknowledgements

I would like to thank the many kind individuals without whom this work would not be possible.

I am eternally grateful for the guidance, advice, support, assistance, motivation and mentorship in both the academic and personal spheres from Prof. Oleg Smirnov, Dr Viral Parekh and the rest of the RATT galaxy clusters group; each of whom has shown unwavering patience and understanding for which I am eternally thankful.

Thank you to Dylan for your amazing friendship and acceptance; you are a beautiful human.

Last but not least, thank you to my family, my mom, dad and brother, without whom I would not be the person I am proud to be today. Thank you.

# Declaration

I, **Keegan Somerset Trehaeven**, fully understand the meaning of plagiarism and hereby declare that all of the work in this document, unless stated otherwise through source acknowledgement, is my original research.

# Declaration of Publications

Publications that form part and/or include research presented in this thesis:

**K S Trehaeven**, V Parekh, N Oozeer, B Hugo, O Smirnov, G Bernardi, K Knowles, C Tasse, K M B Asad, S Giacintucci, *Mining mini-halos with MeerKAT I. Calibration and imaging*, Monthly Notices of the Royal Astronomical Society, Volume 520, Issue 3, April 2023, Pages 4410–4426, https://doi.org/10.1093/mnras/stad391

# Contents

# List of Figures

# List of Tables

# List of Abbreviations

| | |
|---|---|
| **LSS** | **L**arge **S**cale **S**tructure |
| **ICM** | **I**ntra**C**luster **M**edium |
| **BCG** | **B**rightest **C**luster **G**alaxy |
| **AGN** | **A**ctive **G**alactic **N**ucleus |
| **CC** | **C**ool-**C**ore |
| **nCC** | **n**on-**C**ool-**C**ore |
| **SKA** | **S**quare **K**ilometre **A**rray |
| **MeerKAT** | *Meer* **K**aroo **A**rray **T**elescope |
| **RFI** | **R**adio **F**requency **I**nterference |
| **CR** | **C**osmic **R**ays |
| **CRe** | **C**osmic **R**ay **e**lectrons |
| **CRp** | **C**osmic **R**ay **p**rotons |
| **VLA** | **V**ery **L**arge **A**rray |
| **GMRT** | **G**iant **M**eterwave **R**adio **T**elescope |
| **LOFAR** | **LO**w **F**requency **AR**ray |
| **FoV** | **F**ield **o**f **V**iew |
| **PSF** | **P**oint **S**pread **F**unction |
| **MFS** | **M**ulti-**F**requency **S**ynthesis |
| **RIME** | **R**adio **I**nterferometer **M**easurement Equation |
| **DI** | **D**irection-**I**ndependent |
| **DIE** | **D**irection-**I**ndependent **E**ffect |
| **DD** | **D**irection-**D**ependent |
| **DDE** | **D**irection-**D**ependent **E**ffect |
| **1GC** | **First G**eneration **C**alibration |
| **2GC** | **Second G**eneration **C**alibration |
| **DR** | **D**ynamic **R**ange |
| **rms** | **r**oot **m**ean **s**quare |
| **3GC** | **Third G**eneration **C**alibration |
| **lsm** | **l**ocal **s**ky **m**odel |
| **HR** | **H**igh-**R**esolution |
| **SRC-SUB** | **S**ou**RC**e-**SUB**tracted |
| **LLS** | **L**argest **L**inear **S**ize |
| **LR** | **L**ower **R**esolution |

# List of Symbols

| | |
|---|---|
| $\nu$ | Frequency |
| $S_\nu$ | Flux density at frequency $\nu$ |
| $\alpha$ | Spectral index |
| $\theta$ | Angular resolution |
| $\lambda$ | Wavelength |
| $D$ | Aperture diameter |
| $t_g$ | Geometric delay |
| $b$ | Baseline length |
| $c$ | Speed of light in vacuum |
| $V(u,v)$ | Visibility as a function of $u$ and $v$ |
| $I_\nu(l,m)$ | Sky/surface brightness distribution |
| $\mathscr{F}$ | Fourier transform |
| $\mathscr{F}^{-1}$ | Inverse Fourier transform |
| $S$ | Sampling function |
| $I_\nu^D$ | Dirty image |
| $*$ | Convolution |
| $s$ | Point spread function/dirty beam |
| $J$ | Generic Jones term |
| $B$ | Brightness matrix |
| $G/E$ | Chained DI/DD Jones matrices |
| $z$ | Redshift |
| $\Delta A$ | Uncertainty to measurement A |
| $uv_{min}$ | Lower bound of $uv$-cut |
| $scale$ | Angular-to-linear scale |
| $kpc$ | Kilo-parsec |
| $\sigma_{MH}$ | Mini-halo flux density uncertainty |
| $\sigma_{cal}$ | Calibration/fluxscale uncertainty |
| $N_{beam}$ | Number of beams |
| $\sigma_{sub}$ | Point source subtraction uncertainty |
| $I_{MH,s}$ | Mini-halo surface brightness within region $s$ |
| $N_{beam}$ | Number of beams within region $s$ |
| $D_{MH}$ | Mini-halo diameter/largest-linear-size |
| $D_{min}/D_{max}$ | Mini-halo minimum/maximum diameter |
| $P_{1.4GHz}$ | Power at 1.4 GHz |
| $D_L$ | Luminosity distance |
| $k$ | Spatial correlation slope |

# Chapter 1

# Introduction

The large-scale structure (LSS) of the Universe is called the 'Cosmic Web'; it is described as such because most of the Universe's mass and energy is contained within filamentary-like structures, with nodes connecting different filaments and voids separating them, just like a spider's web. This structure builds via the hierarchical gravitational capture (or merging) of larger systems with smaller systems. The largest gravitationally bound structures in the Universe are galaxy clusters formed at the nodes of the Cosmic Web. Most of their baryonic mass is hosted by the hot, tenuous, intra-cluster medium (ICM), which is the gas and particles that occupy the space between the member galaxies of the cluster. This medium can be studied in many ways to inform on many aspects of cluster formation, evolution, dynamics and composition. Of particular interest in this work is the observation of diffuse radio emission located in and around the cluster core, which ultimately probes this environment's dynamic state and evolutionary stage.

In this Chapter, I give context to the research objectives of this work. I introduce galaxy clusters and the ICM, concentrating on the emission mechanisms that create the sources of interest. I also describe why the MeerKAT telescope is the best instrument for studying the current research topic. After that, I outline the research objectives and structure of this thesis.

## 1.1 Galaxy clusters

Galaxies are gravitationally bound collections of stars and gas. They were serendipitously discovered in the late 1700s when Charles Messier was studying comets but were unknown objects at the time (Messier, 1781). About ~150 years later, Edwin Hubble discovered that galaxies exist outside our own Milky Way (Hubble, 1926). Galaxies are the building blocks of galaxy clusters, which are gravitationally bound collections of galaxies and gas and contain 100s of galaxies and/or galaxy groups. Clusters grow mainly by merging with other (usually smaller) systems and can usually be divided into two categories depending on their merging state. Clusters that have undergone a merger event with a system of comparable mass (a major merger) are *disturbed* because most of the energy released in such an event dynamically disturbs the ICM. In contrast, those that have not experienced such a turbulent event are *undisturbed* or *relaxed*. The term *massive* in this context is reserved in the literature for those clusters with mass $M_{500} \gtrsim 5 \times 10^{14} M_{\odot}$, where $M_{500}$ is the cluster mass within the radius enclosing a mean density of 500 times the critical density at the cluster redshift (Planck Collaboration et al., 2014). A centrally dominant (cD) galaxy is usually found in the cluster core. This galaxy is usually the brightest in the optical regime, referred to as the Brightest Cluster Galaxy (BCG), and hosts an Active Galactic Nucleus (AGN) from which large amounts of multi-wavelength electromagnetic radiation is emitted.

## 1.2 ICM

Most of the baryonic mass of a cluster lies within its ICM (~80%, Riseley et al., 2022a). Cluster mergers are some of the most energetic events in the Universe, releasing $\sim 10^{64}$ ergs over a timescale of a few Gyrs, of which most is transferred to the ICM via shocks and turbulence; the ICM is then heated/energised as a result. The ICM is a very rich environment, with many different phenomena occurring within due to different radiative processes (Rybicki & Lightman, 1986). The distinction between the thermal and non-thermal components of the ICM is important for understanding the work presented later. The term 'thermal' describes any emission mechanism

that depends only on the temperature of the surrounding environment, e.g. blackbody radiation. 'Non-thermal' describes any mechanism that depends on other physics in its environment, e.g. the presence of magnetic fields and relativistic charged particles.

### 1.2.1 X-ray

The thermal component of the ICM consists of a hot ($\sim 10^{7-8}$ K) and tenuous ($\sim 10^{-3}$ particles.cm$^{-3}$) plasma of charged particles that permeates the cluster volume. This plasma emits bright ($\sim 10^{44}$ erg/s) extended X-ray radiation produced via *bremsstrahlung* (German for *braking radiation*), also called free-free radiation (van Weeren et al., 2019). This radiation occurs when a high-energy (keV) free charged particle is decelerated by the electric field of another charged particle such that an X-ray photon is emitted. However, the incident particle remains free after the interaction (e.g., Forman & Jones, 1982). Figure 1.1 shows a schematic diagram of the process. Galaxy clusters are one of the only extended X-ray sources in the sky. The intensity of the extended emission reveals the energy density of the thermal ICM plasma, which is a direct probe of the gas dynamics and overall intra-cluster environment. The thermal properties of the ICM have been well modelled and understood by studying its diffuse X-ray emission (e.g., Laganá et al., 2019; ZuHone & Su, 2022).

Without any major disturbances, the radiative losses cause a pressure gradient in the cluster environment resulting in a cooling flow that channels the hot gas from the periphery towards the centre of the cluster. This central gas of relaxed clusters often remains much cooler than that of disturbed clusters. This central region of low-entropy gas ($K_0 \leq 50$ keV cm$^2$) is called a *cool-core* (CC) and is usually centred around the cluster's peak density, with a radius $\lesssim 300$ kpc and is surrounded by ambient higher entropy gas (Markevitch & Vikhlinin, 2007). However, the cool gas does not remain completely undisturbed. Often, a sub-cluster, galaxy group or an individual member galaxy will fall into the potential well of the core; such events would have high mass ratios and are called *minor mergers*. The gravitational interaction can transfer angular momentum to the dark matter and core gas such that the gas oscillates (or sloshes) around the potential minimum, often in a spiral pattern, and creates a series of contact discontinuities or *cold-fronts* up to the CC

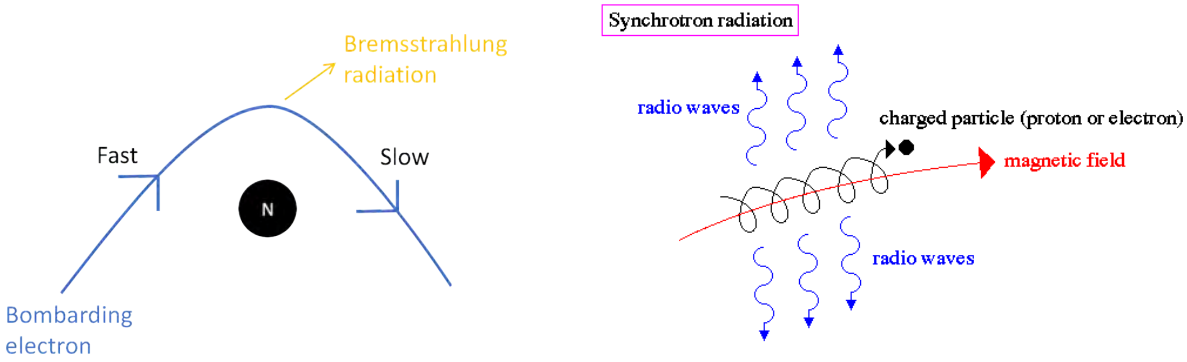


Figure 1.1: ICM emission mechanisms. *Left:* Bremsstrahlung radiation. A free charged particle (electron) is decelerated by the electric field of another charged particle (either a proton or atomic nucleus) such that the loss of kinetic energy is emitted as an X-ray photon. Source `https://www.radiologycafe.com/frcr-physics-notes/X-ray-imaging/production-of-X-rays/` *Right:* Synchrotron radiation. A free charged particle (predominantly an electron) is accelerated into a spiral motion around a magnetic field line. The increase in angular momentum produces a photon with a wavelength in the radio regime. Source `http://abyss.uoregon.edu/~js/glossary/synchrotron_radiation.html`

boundary (Ascasibar & Markevitch, 2006). It is important to note that the line between CC and non-cool-core (nCC) clusters can be blurred. Heating processes such as AGN feedback and even the gas sloshing can cause the core gas to increase beyond the given threshold such that the cluster is both dynamically relaxed but possesses an nCC (e.g., Leccardi et al., 2010; Laganá et al., 2019; Raja et al., 2020).

### 1.2.2 Diffuse radio emission

The free-free radiation mechanism can result in the emission of radio photons if the scattering of the incident electron is very small. This is also a type of thermal radiation but does not contribute towards the radio emission observed from the ICM because the temperatures and energies are too high for such interactions to occur. The observed radio emission from the ICM is non-thermal. This emission is produced when a cosmic ray (CR) is accelerated by the magnetic field that permeates the cluster volume. The increase in momentum releases a radio-wavelength photon (Brunetti & Jones, 2014; van Weeren et al., 2019, respectively give comprehensive theoretical and observational discussions concerning diffuse radio emission within galaxy clusters). CRs are

ultra-high-energy (GeV) free charged particles such as electrons (CRe), protons (CRp) and heavier nuclei travelling at relativistic speeds; these particles are not in thermal equilibrium with their surrounding environment. The electrons are the lightest and so are accelerated the most by the ICM magnetic fields, such that they emit electromagnetic radiation in the radio regime – called *synchrotron radiation*. Figure 1.1 shows a schematic diagram of the process. The power radiated is calculated by the relativistic Larmor formula (F.R.S., 1897), given by

$$P = \frac{e^2}{6\pi\epsilon_0 c^3}\gamma^6 \left[\left(\dot{\beta}\right)^2 - -\left(\beta \times \dot{\beta}\right)\right] \tag{1.1}$$

where $e$ the charge of an electron, $\epsilon_0$ is the vacuum permittivity, $c$ the speed of light, $\gamma = \sqrt{1 - v/c}$ is the Lorentz factor, $\beta = v/c$ represents the speed of the particle and $\dot{\beta}$ its acceleration. We can see that the intensity is proportional to the speed and acceleration of the particle. Hence, studying the diffuse radio emission directly probes the dynamics of the ICM environment independently of X-ray studies (Feretti et al., 2012).

The ICM sources of synchrotron radiation are generally classified into three broad phenomena: radio halos, shocks (or relics), and revived AGN fossil plasma, each with sub-classes that have their unique combination of production mechanism, location, size, polarisation (van Weeren et al., 2019). The brightness intensity of such sources is measured in units of Jansky (1 Jy = $10^{26}$ W/m$^2$/Hz) and describes the flux density, $S_\nu$, of a source (Brunetti & Jones, 2014). They are usually very weak ($\sim$ 1 uJy/arcsec$^2$), hence why they have been studied only in recent years with the construction of more powerful radio telescopes. The flux density has a power-law dependence on frequency, $\nu$, described as

$$S_\nu \propto \nu^{-\alpha}, \tag{1.2}$$

where $\alpha$ is the spectral index. This value can be calculated by measuring the brightness of a source at various frequencies and fitting the data to a power-law in log-log space so that $\alpha$ represents the slope of the resulting straight line, where the steepness of the slope has implications on the underlying physics and emission mechanism. When this is performed in 1D, measuring the total

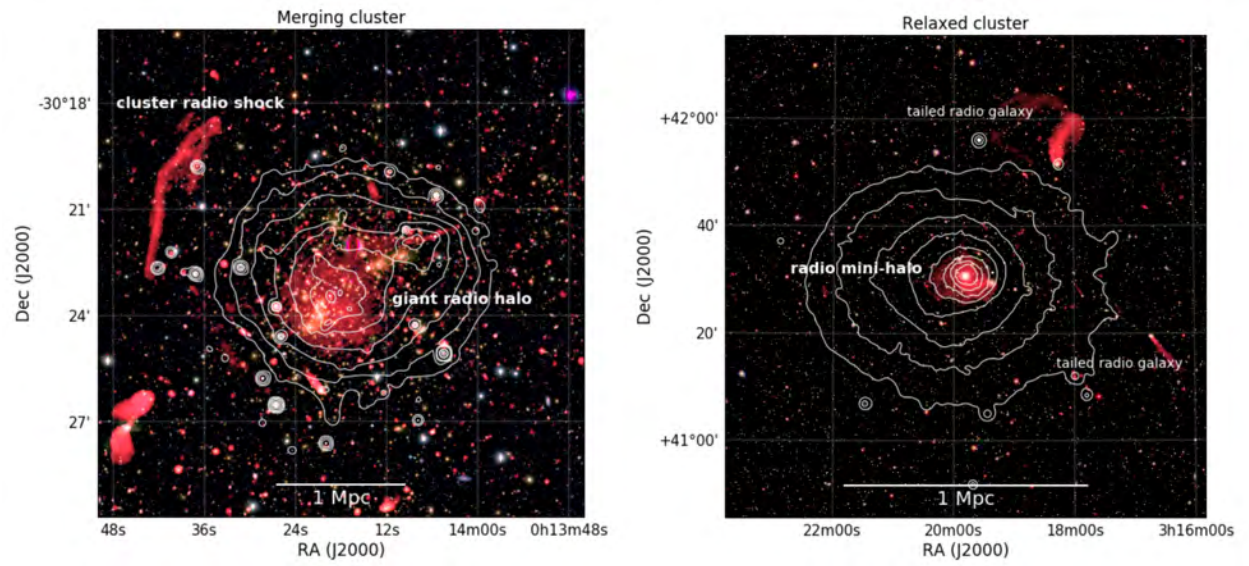


Figure 1.2: ICM multi-wavelength images. Radio surface brightness is shown in red, and X-ray surface brightness is in white contours. These emissions are overlaid onto optical images centred on the cluster core. *Left:* VLA 1–4 GHz and Chandra 0.5–2.0 keV images of the merging galaxy cluster Abell 2744 with different source classes labelled, from Pearce et al. (2017), overlaid on a *Subaru BRz* image (Medezinski et al., 2016). This cluster hosts a luminous giant radio halo and a cluster radio shock. *Right:* VLA 230–470 MHz and XMM-Newton 0.4–1.3 keV images of the relaxed CC Perseus cluster from Gendron-Marsolais et al. (2017), overlaid on an SDSS *gri* optical image (Abolfathi et al., 2018). The Perseus cluster hosts a radio mini-halo and two prominent tailed radio galaxies. Source: van Weeren et al. (2019).

source brightness across each frequency, the result is an integrated spectrum that describes the average spectral index across the spatial extent of the source. However, when performed on a per-pixel basis, the result is a 2D spectral index map that shows how the spectral index varies spatially across the source. A zero index is termed 'flat' and denotes that the source intensity does not depend on frequency–this is characteristic of thermal free-free radio emission. Synchrotron emission is characterised by a steep spectrum ($\alpha \gtrsim 1.3$), so these ICM sources are more powerful at lower radio frequencies.

The first detected diffuse radio emission source was a giant radio halo at the centre of the Coma cluster (Large et al., 1959; Willson, 1970). Since then, technological advancements, radio telescopes, and interferometry have expanded our capacity to capture such sources. The ever-growing number of diffuse sources has reached over 300 detections of different source sizes, shapes, and locations (van Weeren et al., 2019). These numbers will grow even more with next-generation

telescopes (Gitti et al., 2015, 2018). A combined X-ray and radio cluster environment analysis can inform the relationship between its thermal and non-thermal components.

As a visual example, Figure 1.2 shows multi-wavelength images of a merging and relaxed cluster with different diffuse radio sources in each. Such images are useful in highlighting the relative intensities and morphologies of the different emissions and understanding the underlying physics responsible. The merging cluster shows diffuse radio emission on larger scales and an irregular X-ray distribution because the ICM has been dynamically disturbed, and an elongated radio shock is evident that is thought to trace the merger shock-wave. In contrast, the only diffuse radio emission in the relaxed cluster is centred around the cluster core, and with no major-merger event, the X-ray distribution is more uniform.

**Magnetic fields**

Diffuse radio emission indicates the existence of Mpc-scale magnetic fields in the ICM. The radiative lifetime and intensity of synchrotron emission, particle acceleration and transport processes directly depend on the magnetic field strength and configuration. However, few details are known about these fields' precise origins and properties since they are difficult to measure (van Weeren et al., 2019). It is thought that they originated from weak (∼nG) primordial fields and have been amplified due to structure formation (Donnert et al., 2018). Through the assumption of *equipartition*–where the total energy in radio-emitting regions of the ICM is equally distributed between its independent components, i.e. cosmic rays and magnetic fields–estimates of the ICM magnetic field strength of 0.1–10 μG have been found (Govoni & Feretti, 2004; Brüggen et al., 2012). The strength and structure of these fields can be studied via the analysis of the Faraday rotation, changes in the radio wave's intrinsic polarisation angle, of radio galaxies located inside and behind the cluster (e.g., Di Gennaro et al., 2021). However, such analyses are difficult because of the limited number of polarised radio sources. Alternatively, the differential Faraday rotation between different lines of sight can incorporate the more numerous unpolarised radio sources to estimate upper limits on the polarization fraction (Osinga et al., 2022). Simulations show that the

fields are turbulent with coherence lengths of a few 10 kpc (Vazza et al., 2018), the field strength decreases in the outer regions of the cluster, and the CC of relaxed clusters have a higher central magnetic field strength than merging clusters ($\sim$10 $\mu$G as opposed to $\sim$1 $\mu$G) (van Weeren et al., 2019). The greater strength in CC regions is expected since many models explain the apparent CC vs non-CC bimodality by different cluster magnetic field configurations (Ruszkowski & Oh, 2010; ZuHone et al., 2013). Future radio instruments such as the Square Kilometre Array (SKA) will provide large samples of polarised radio sources for such studies and enable a detailed classification of magnetic fields (Johnston-Hollitt et al., 2015; de Gasperin et al., 2022).

## 1.3 The MeerKAT telescope

The MeerKAT telescope (Jonas & MeerKAT Team, 2016; Camilo et al., 2018; Mauch et al., 2020), located in the Karoo desert of South Africa, consists of 64 parabolic dishes, each 13.5-m in diameter using offset Gregorian optics. Most of its antennas (approximately three quarters) lie within a dense core region of diameter 1 km, with the shortest baseline of 29 m. The remaining dishes spread to a maximum baseline of 7.6 km, giving a maximum and minimum angular scale of $\sim$0.5° and $\sim$5″ at L-band, respectively. The many short baselines allow MeerKAT to observe large-scale diffuse emissions, while the longer baselines simultaneously resolve compact sources. Each antenna currently is equipped with UHF-band (544-1088 MHz), L-band (856-1712 MHz) and S-band (1750-3500 MHz) receivers. The correlator supports either 4096 (4k) or 32768 (32k) frequency channelisation, and integration times of 2, 4 or 8 seconds. The average system temperature is very low ($\sim$20 K) and induces very little thermal noise to the receiver systems. The fine channalisation allow for the precise removal of radio frequency interference (RFI) from the observation data. All these attributes make MeerKAT an exceptionally sensitive telescope to both small- and large-scale low surface brightness continuum emission, which is particularly important in studying diffuse radio emission. Any compact sources (often only a few arcseconds in size) projected along the line-of-sight need to be disentangled from the diffuse emission in order to pre-

cisely image and study the underlying target of interest (such as in Knowles et al., 2016; Bonafede et al., 2022; Pasini et al., 2022).

## 1.4 Thesis outline

This work presents the calibration, imaging and initial science results of a sample of radio mini-halos observed by the MeerKAT telescope. These are the first MeerKAT mini-halo observations. I aim to produce valid scientific data products and results to show that further investigation of many more mini-halos with MeerKAT is a very exciting prospect and could lead to a much better understanding of the physics behind these sources. The thesis is structured as follows. In Chapter 2 and Chapter 3, I offer a comprehensive theoretical background to radio mini-halos and the techniques needed to analyse them. Chapter 4 then describes the MeerKAT observations and the details of our data reductions and analyses that turned the raw data into meaningful scientific images. Chapter 5 describes the mini-halo flux densities, powers, spectral indices and sizes. Chapter 6 then describes these sources in the context of the current sample of known mini-halos. Thereafter, in Chapter 7, I give a point-to-point spatial correlation analysis for two complementary sources of our sample and discuss the results in the context of possible mini-halo production mechanisms. Finally, Chapter 8 gives our summary and conclusions of this work and details some future work.

# Chapter 2

# Literature survey: Mini-Halos

Here, I provide a thorough overview of the physics and open questions of radio mini-halos.

Mini-halos are clouds of diffuse low surface brightness synchrotron emission that are found to surround the Brightest Cluster Galaxy (BCG) at the centres of massive CC galaxy clusters, often extending radially outwards to a few 100 kpc in size. The current sample consists of some 30 confirmed objects and 10 uncertain or candidate cases, all having a broad range of morphology, spectral behaviour and host environment (e.g., Giacintucci et al., 2019; Richard-Laferrière et al., 2020; Knowles et al., 2022; Riseley et al., 2022a). The current scientific definition describing a mini-halo is outlined in Giacintucci et al. (2017) and is summarised as follows: a diffuse radio source at the cluster centre that (1) does not consist of or have any morphological connection to any emission directly associated with any embedded galaxies, and (2) has a radius between 50 kpc-$0.2R_{500}$[1]. Smaller sources can plausibly be explained by diffusion from the central AGN (e.g., Giacintucci et al., 2014b), while $0.2R_{500}$ is the typical boundary of the cluster core in which non-gravitational processes like AGN feedback and cooling flows become important (McDonald et al., 2017).

Mini-halos are a sub-class of radio halos but are thought to trace a different particle (re)-acceleration mechanism than their giant counterparts (van Weeren et al., 2019). The embedded

[1] $R_{500}$ is the radius that encloses a mass density 500 times the critical density of a flat Universe at the cluster redshift

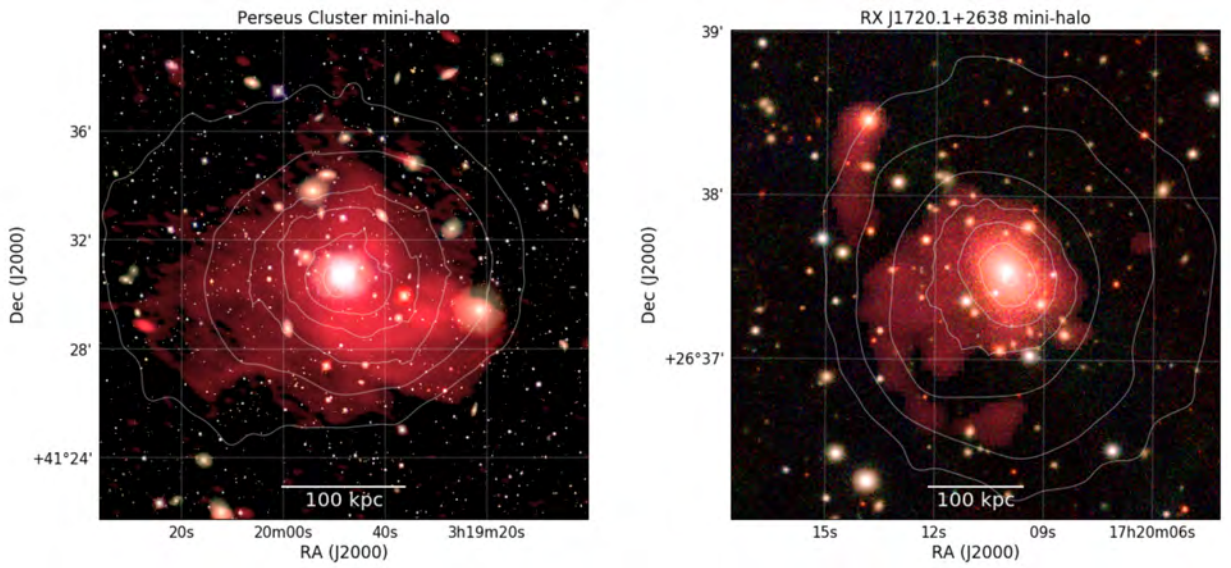


Figure 2.1: Mini-halo multi-wavelength images. The different emissions are described in Figure 1.2. *Left:* a central cutout of the right panel of Figure 1.2 showing the Perseus mini-halo. *Right:* GMRT 617 MHz and *Chandra* 0.5–2.0 keV images (Giacintucci et al., 2014a; Andrade-Santos et al., 2017) of the cluster RX J1720.1+2638, overlaid on a Pan-STARRS *grz* image (Chambers et al., 2016). Source: van Weeren et al. (2019).

AGN can eject CRe (and other particles that decay to CRe) that interact with the cluster magnetic field and produce synchrotron radiation. However, CRe radiate their energy as they travel within the thermal plasma of the ICM; thus, they have a finite radiative lifetime of $\sim 10^{7-8}$ years (van Weeren et al., 2019) after which they do not have enough energy to emit such radiation. This lifetime is too short for a CRe to diffuse from the BCG to the typical length-scales of a mini-halo via a single acceleration event, which would take $\sim 10^{9}$ year (Taylor et al., 2002; Giacintucci et al., 2014a). Hence, some in-situ particle (re)-acceleration needs to be invoked to reconcile the theory with the observed mini-halo sizes. The exact mechanism that (re)-accelerates the CRe up to synchrotron-emitting energies is still under debate. However, it is thought to be closely linked to the cluster thermal component and/or the AGN (Giacintucci et al., 2019). Figure 2.1 gives examples of known mini-halos, those in the Perseus cluster and RX J1720.1+2638; both of which display some substructure in the radio, such as a spiral arm in RX J1720.1+2638, which suggests a complex formation mechanism.

## 2.1 Particle (re)-acceleration mechanisms

There are two main trains of thought when considering the exact production mechanism of mini-halos, namely that of hadronic collisions and turbulent (re)-acceleration (Brunetti & Jones, 2014; van Weeren et al., 2019). Simulations of both (ZuHone et al., 2013, 2015) can explain the current mini-halo observables, but each has shortcomings.

### 2.1.1 Hadronic collisions

The first possibility is inelastic collisions between populations of CRp and ICM thermal protons in which a population of CRe can be produced as a by-product (Pfrommer & Enßlin, 2004; Jacob & Pfrommer, 2017a,b). CRp have much longer radiative lifetime than their electron counterparts and can diffuse out to a typical mini-halo radius while continuously providing a population of fresh CRe at a range of energies which would thereafter produce synchrotron emission (van Weeren et al., 2019). The central AGN is a clear candidate for the origin of the CRp population and supernovae and shocks associated with cosmological structure formation, which could have accelerated some of the thermal protons to relativistic energies. As an additional by-product, a gamma-ray counterpart to the mini-halo should exist, but none have been observed thus far; however, derived gamma-ray upper-limits on the Perseus mini-halo do not yet allow for the elimination of this model (Ackermann et al., 2014; Ahnen et al., 2016).

### 2.1.2 Turbulent (re)-acceleration

In (re)-acceleration models, a population of seed electrons is (re)-accelerated by some ICM turbulence (Brunetti et al., 2001; Pinzke et al., 2017). This mechanism is invoked for giant halos where major mergers induce the turbulence (e.g., Donnert et al., 2010b,a, 2013). In the case of mini-halos, the embedded AGN is a clear candidate for the origin of the seed electrons (Giacintucci et al., 2014a). However, the open question is how they are (re)-accelerated – the answer may be AGN feedback processes (Gitti et al., 2015; Richard-Laferrière et al., 2020) and/or the gas sloshing

indicative of X-ray CCs (Mazzotta & Giacintucci, 2008; Ignesti et al., 2022). Many mini-halos are contained within the sloshing regions of CCs; however, some spill over (e.g., Giacintucci et al., 2014a; Savini et al., 2019; Biava et al., 2022), leading many to suggest that some combination of AGN processes and gas sloshing is responsible. For example, Richard-Laferrière et al. (2020) suggested that gas sloshing contributes to the overall shaping of the mini-halos while the underlying turbulence is driven by AGN feedback.

## 2.2 Simulations of mini-halo formation

ZuHone et al. (2013) simulated the sloshing motions induced by a minor merger in which a massive CC galaxy cluster with magnetised gas interacts with an infalling subcluster to produce sloshing motions in the core. The resulting turbulent velocities (re)-distributed and (re)-accelerated the pre-existing population of CRe, which were initialised to a variety of physically reasonable spatial and spectral configurations. The resulting faint extended radio sources closely resembled the spatial and spectral properties of some observed mini-halos. The emission traced the spatial features of the X-ray emitting gas and was confined to the spirals of the sloshing cold-fronts with a steep-spectrum of $\alpha \sim 1-2$. However, the simulations could not replicate the extra radio emission that spills over the cold-fronts as seen in some observations, see Section 2.5.

Thereafter, ZuHone et al. (2015) performed similar simulations to test the hadronic model. They used the same setup as their previous simulations. However, they replaced the pre-existing CRe population with a time-dependent injection of CRe that would originate from hadronic interactions and undergo radiative and Coulomb energy losses due to interactions with the thermal gas and magnetic field amplification. They find that the resulting radio emission has slightly different spectral indices and spatial extents from the previous simulations. Specifically, the electron spectra lie within a narrower range than that determined for the turbulent (re)-acceleration simulations, with slopes $\alpha \sim 1.0-1.3$ and the maxima occurring at the cold-fronts where the magnetic field is strongest. Some mini-halos have been observed with much steeper spectra than this (e.g., those

mentioned in Section 2.5), putting tension on the hadronic model. However, they also find that the radio emission extends over the cold-fronts in certain directions, similar to those mentioned in Section 2.5. They find that this occurs where the magnetic field strength changes more smoothly across the cold-front surface.

The above authors say that the parameter spaces explored were necessarily limited. More detailed simulations with different initial conditions and configurations of the thermal and non-thermal components need to be conducted if any more theoretical constraints on mini-halo characteristics are to be derived (e.g., Vazza et al., 2021). A natural extension that ZuHone et al. (2015) suggest is to incorporate the dynamics of the CRp population in a self-consistent manner to determine the role they play in mini-halo morphologies and the damping of turbulence. Nevertheless, the differences in electron spectra and mini-halo extent seen in the simulations can be compared to observational results to discriminate between the two models.

## 2.3 Correlations between mini-halo radio power

Although the number of known mini-halos is limited, the sample is large enough to perform rudimentary statistical studies and test specific physical correlations. Such studies provide information about mini-halos as a population and may hint towards their underlying physics. Potential bias must be considered when conducting such tests. Since each correlation tested has been performed with the entire sample of known mini-halos at the time, the only significant source of bias should be that of observational limitations (i.e. correspond to the brightest mini-halos because they are the easiest to discover). Perhaps the most obvious connection is that most mini-halos are hosted by massive CC clusters. Giacintucci et al. (2017) studied a sample of massive galaxy clusters and found that most (80%) possessing a CC also possessed a mini-halo, suggesting that mini-halos are common in massive CC clusters. Only one mini-halo has been discovered in an nCC cluster, ACO 1413 (Savini et al., 2019), leading to the assertion that they are closely related to the cluster thermal component. Below I describe some of the correlations discussed in the literature.

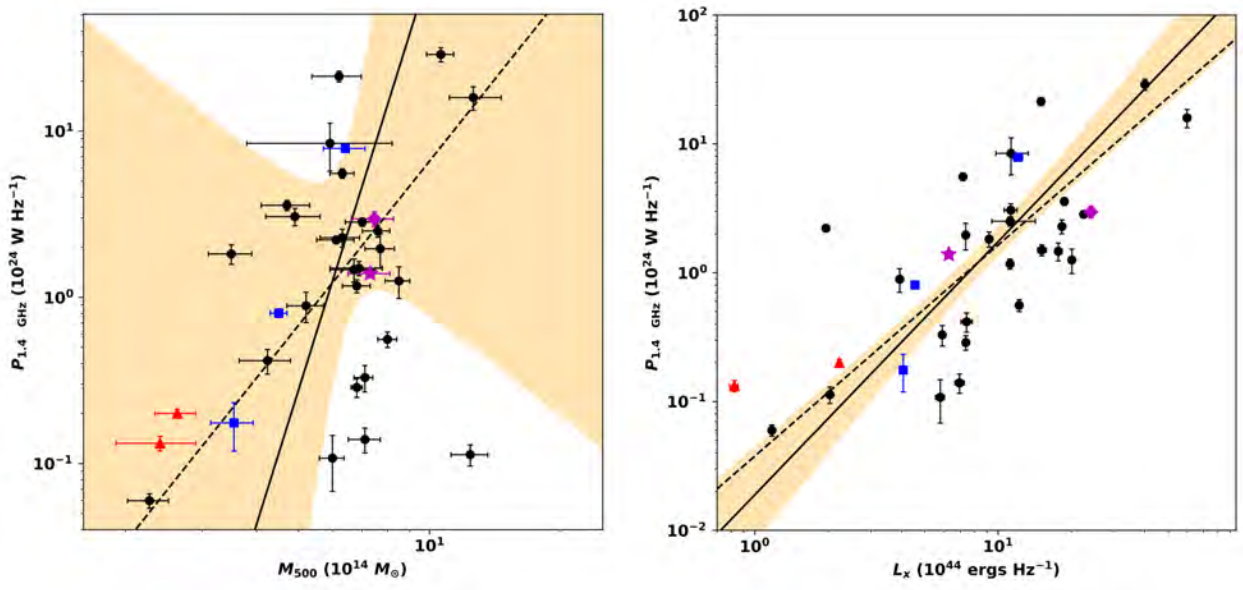


Figure 2.2: Mini-halo radio power correlations. *Left:* The 1.4 GHz radio power of the 33 mini-halos is plotted against the mass of the host cluster. Candidate and uncertain mini-halos are shown as blue squares and red triangles, respectively. The magenta star and diamond show the confirmed and new mini-halo detections discussed in the cited work. The best-fit lines of two different methods are shown as a solid and dashed line, and the shaded region corresponds to the 95% confidence interval on the solid line. *Right:* Same but plotted against the X-ray luminosity inside a radius of 600 kpc. Source: Richard-Laferrière et al. (2020).

### 2.3.1 Cluster mass

All known mini-halos are hosted by a massive cluster. However, Giacintucci et al. (2014a, 2019) found no evidence for any correlation between the mini-halo radio power and cluster $M_{500}$ mass for the known population, contrary to what is found for giant halos (e.g., Cassano et al., 2013). Nevertheless, Richard-Laferrière et al. (2020) does find a general trend where more powerful mini-halos are hosted by more massive clusters, albeit with significant scatter as shown in the left panel of Figure 2.2. This may suggest that mini-halos can also form in less massive clusters but are too faint to detect with previous radio telescopes. They find a similar result when the radio power is compared to the mini-halo radius.

### 2.3.2 X-ray luminosity

Giacintucci et al. (2019) found a moderate correlation between mini-halo radio power and total X-ray bolometric luminosity measured within $R_{500}$. However, in CC clusters, a significant fraction of the total X-ray luminosity is found within the cluster core (Maughan et al., 2012). Hence, Giacintucci et al. (2019) and Richard-Laferrière et al. (2020) found that the correlation is stronger when compared against the X-ray luminosity of the inner-most part of the cluster. Richard-Laferrière et al. (2020) found a similar correlation, as depicted in the right panel of Figure 2.2, suggesting that the mini-halo radio power closely linked to the thermal properties of the CC.

### 2.3.3 BCG power

Govoni et al. (2009) first noted a possible correlation between the mini-halo radio power and that of the embedded BCG. Giacintucci et al. (2019) find a moderate correlation, but one that is weaker than that of the mini-halo power vs core X-ray luminosity, suggesting that the mini-halos are more directly affected by the thermal properties of the host core than AGN feedback. (Richard-Laferrière et al., 2020) finds a slightly stronger correlation against both the radio power of the past (associated with the jets/lobes) and ongoing (associated with the core) AGN activity, perhaps suggesting that the AGN may impact the mini-halo evolution.

### 2.3.4 Cavity power

If an AGN launches powerful relativistic jets, the mechanical energy displaces the thermal component of the ICM and creates cavities of reduced X-ray power. However, only about half the available sample of mini-halos possess X-ray cavities. Nevertheless, Richard-Laferrière et al. (2020) finds a tentative correlation between the mini-halo radio power and the X-ray cavity power for the 14 mini-halos with well-characterised cavities. Unsurprisingly, they also find a moderate correlation between the power of the past AGN activity and X-ray cavities.

## 2.4 Radio-X-ray point-to-point analyses

In recent years, with the coming of high-resolution images in both radio and X-ray observations, point-to-point analyses have become popular to test spatial correlations between the non-thermal and thermal components of the ICM (e.g., Rajpurohit et al., 2021b; Sikhosana et al., 2022). The relative surface brightness distributions of these components can be studied by calculating the slope of the power-law relation between the radio and X-ray emission, which is explained in detail in Chapter 6.

The spectral analysis of mini-halos is limited in the literature due to the need for high-quality, high-resolution images observed at different frequencies. However, such studies are the focus of many recent works (e.g., Riseley et al., 2022a; Rajpurohit et al., 2022). Additionally, exploring the radio spectral index/X-ray surface brightness plane in linear-log space and so-called colour-colour diagrams (Carilli et al., 1991; Katz-Stone et al., 1993) could shed light on possible spectral ageing models and magnetic field configurations. Such studies have been performed on several other diffuse radio sources and some tension has been found with competing correlations (e.g., Botteon et al., 2020; Rajpurohit et al., 2021a).

## 2.5 Unification

Recent observations of unusual (mini-) halos question the division between mini- and giant halos. Despite the differences, they may be physically related to each other. Bonafede et al. (2014) discovered a giant halo of size 1.1 Mpc in the CC cluster CL1821+643. If a merger event causes this halo, the cluster should be in an evolutionary stage where the merger has not (yet) disrupted the CC (as also noted by Kale & Parekh, 2016). Therefore, the halo could be a transitional object where the mini-halo is converting into a giant halo. A similar notion is suggested by Kale et al. (2019) for the cluster RXC J0232.2-4420. Savini et al. (2018, 2019) found secondary components of ultra-steep-spectrum (USS) emission surrounding the mini-halos in the CC clusters RX J1720.1+2638 and PSZ1 G139.61+24.20, respectively. They suggest that the emission outside the

core is produced by turbulent re-acceleration from a minor merger event that has not disrupted the CC. This would then suggest that mini- and giant halos could co-exist. Several other clusters have been detected that host both a mini-halo and larger-scale diffuse radio emission (e.g., Venturi et al., 2017; Raja et al., 2020; Biava et al., 2021; Riseley et al., 2022a,b). Deep, low-frequency radio observations are required to test if other known mini-halos have similar USS secondary components.

# Chapter 3

# Radio Interferometry and Techniques

In the previous sections, I described the physical phenomena and objects that this work focuses on and why it is essential to present such work. This section gives the technical details about the radio astronomy techniques needed to observe, image and analyse the astrophysics I am interested in.

When most people think of a *telescope*, they usually think of an amateur optical telescope, with a cylindrical tube for a body, mirrors inside, and a small lens for an aperture. This design is practical for optical light but not for the radio regime, which has a much longer wavelength. This is because the resolution of a telescope depends directly on the wavelength of light observed and the diameter of the telescope's aperture. The resolution is the smallest angular scale at which the telescope can distinguish between discrete point-like sources and, for a circular aperture, is given by Rayleigh's criterion:

$$\theta = 1.22\frac{\lambda}{D}, \tag{3.1}$$

where $\theta$ is the angular resolution achievable (in radians), $\lambda$ is the wavelength of the observed light and $D$ is the diameter of the telescope's aperture (F.R.S., 1879). Putting this into perspective, for an amateur telescope described above to resolve an angular distance of one arcsecond (i.e. able to distinguish discrete sources that are an arcsecond apart) of optical light would require an aperture of only ∼15 cm in diameter. However, to resolve radio light in the same manner at the same

resolution would require an aperture upwards of ∼40 km in diameter.

Building a single radio 'telescope' of the above size and design is impractical. Instead, radio astronomers usually build large antenna dishes. Then, analogous to optical telescopes, the electromagnetic wave is reflected to a single focal point, where instead of a human eye, a receiver is placed that digitizes the signal into electrical voltages. This is called single-dish radio astronomy. The limiting sensitivity (or thermal noise) in units of brightness temperature (Kelvin) for any observation on such a telescope is given by the radiometer equation:

$$\sigma_T = \frac{2T_{sys}}{\sqrt{\Delta\nu \times \tau}}, \tag{3.2}$$

where $T_{sys}$ is the telescope system temperature in Kelvin, $\Delta\nu$ is the frequency range of the observations in Hz (called the bandwidth), and $\tau$ spent in seconds observing the object (called the integration time). Hence, a better signal-to-noise ratio (SNR) can be achieved if the system temperature is as small as possible, and the bandwidth and integration time is as large as possible. However, single-dish astronomy still suffers from limited angular resolution at low radio frequencies. For example, the world's largest steerable single-dish radio telescope is the Green Bank Telescope (GBT). It is a 100-m metre dish achieving a resolution of ∼0.2° at ∼1 GHz. To conduct the science introduced in Chapter 2, we require better resolution at this observing frequency. Hence, radio astronomers used interferometry to develop aperture synthesis (Pearson & Readhead, 1984).

Interferometry is the technique of using the interference of superimposed waves to extract information. A radio interferometer is an instrument consisting of an interconnected array of radio antenna dishes (often called elements) that observe the radio sky, where each is separated from the others by a distance called a baseline. Aperture synthesis is the technique of digitally combining the signals from the individual array elements into a single coherent signal analogous to the signal from a single element with an aperture the size of the longest baseline projected onto the sky. Hence, an interferometer discretely samples the collecting area of a single telescope with an aperture the size

of the maximum distance between any two antennas (projected onto the sky). Thus, increasing array size improves the resolution, and increasing the number of elements improves the sampling and, thus, the sensitivity of the synthesised telescope. Examples of interferometers are the Karl G. Jansky Very Large Array (VLA), Giant Meter wave Radio Telescope (GMRT), Low-Frequency Array (LOFAR), Australian SKA Pathfinder (ASKAP) and MeerKAT. Each of these telescopes has arrays of different sizes and configurations depending on their native science goals.

A schematic of a basic two-element interferometer is shown in Figure 3.1. The radio antennas are labelled 1 and 2, are separated by baseline vector **b** and observe the sky in the direction of $s_0$. The source inclination causes the radio waves to arrive at element 2 earlier than element 1, described by the geometric delay:

$$t_g = \frac{b \cos\theta}{c}. \tag{3.3}$$

The antenna receivers convert the radio waves into electrical voltages denoted by $V_1$ and $V_2$, each being a 2-vector with components describing the propagation along the x and y directions. The system electronics delay voltage $V_2$ by $t_g$ with respect to $V_1$ so that both signals arrive at the correlator (denoted by the 'X') at the same time. The correlator then multiplies these components in a complex pairwise manner to produce four cross-correlations or coherences. These cross-correlations are then time and frequency averaged within a finite integration time, or dump rate, and frequency range, or bandwidth, and put into a complex 2x2 matrix, denoted by $V_1V_2$, and from here onwards $V$. This correlation matrix is commonly called the 'visibility' and is precisely what the interferometer measures. Since visibilities consist of complex values, each correlation consists of an amplitude and phase. The former is connected to the observed source shape and intensity, and the latter to the source position. The sum of the diagonal (parallel-hand) correlations is called the Stokes $I$ parameter. It describes the total (polarised and unpolarised) signal from the source, while the off-diagonal (or cross-hand) terms only become important when the source is intrinsically polarised.

An $N$-element interferometer works in the same manner as the basic two-element interferometer but possesses $N(N-1)/2$ independent baselines and therefore measures that many independent

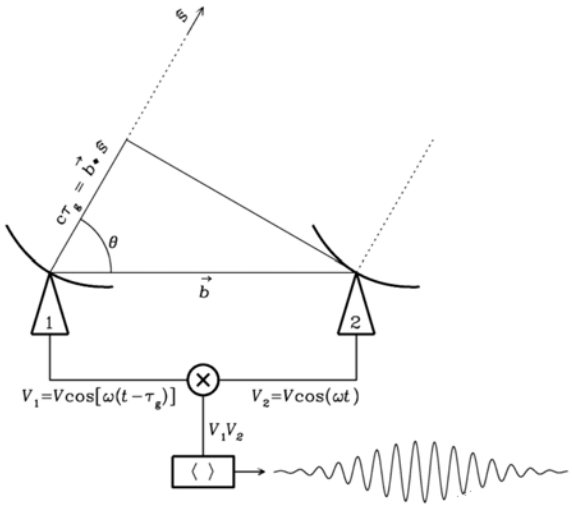


Figure 3.1: Example of a two-element interferometer. The electromagnetic plane wave from an astrophysical source reaches elements 1 and 2 (after some delay) and the resulting electrical voltages are then cross-correlated at the correlator producing a visibility.
https://www.cv.nrao.edu/ sransom/web/Ch3.html

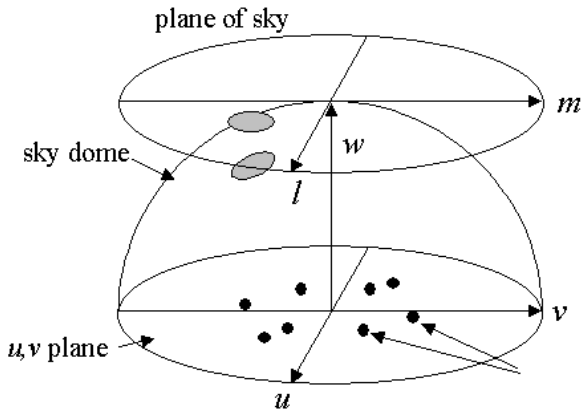


Figure 3.2: Visibility ($uv$) and image ($lm$) planes. The interferometer lies in the $uv$ plane over which the sky dome (or celestial sphere) rotates. The $lm$ plane is tangent to the sky dome and represents the image plane.
https://web.njit.edu/ gary/728/Lecture6.html

visibilities per correlation. The corresponding theoretical noise is similar to that of a single-dish telescope, but scaled by the root of the number of baselines and surface area of a single element ($A_e$) as

$$\sigma_T = \frac{2kT_{sys}}{A_e\sqrt{N(N-1)\Delta\nu \times \tau}}, \tag{3.4}$$

where $k$ is the Boltzmann constant.

## 3.1 The visibility and image domains

Fourier theory is essential in interferometry. I saw above that the measured quantity during interferometric observations is called the visibility and describes the sky brightness distribution (what the sky looks like). Mathematically, the sky brightness distribution is described by the visibility function. Firstly, let us define coordinate systems as in the diagram below and assume the flat-sky approximation: the interferometer is co-planar and/or observes a small field of view (FoV), such that it lies entirely in the *uv* plane and measures the visibility function $V(u, v)$, where $u$ and $v$ are in units of observing wavelength, and the sky-image similarly lies entirely in the *lm* plane, representing positions on the plane tangent to the curved sky, and its sky brightness distribution is denoted by $I_\nu(l, m)$. Then, the van Cittert–Zernike theorem states that the visibility function is the 2D Fourier transform of the sky brightness distribution (Zernike, 1938). Thus I have in the Fourier/visibility domain (uv plane):

$$V(u, v) = \int_{-\infty}^{\infty}\int_{-\infty}^{\infty} I_\nu(l, m)e^{-i2\pi(ul+vm)}dldm = \mathscr{F}\{I_\nu(l, m)\}, \tag{3.5}$$

and in the image domain (lm plane):

$$I_\nu(l, m) = \int_{-\infty}^{\infty}\int_{-\infty}^{\infty} V(u, v)e^{i2\pi(ul+vm)}dudv = \mathscr{F}^{-1}\{V(u, v)\}, \tag{3.6}$$

where $\mathscr{F}$ and $\mathscr{F}^{-1}$ represent the forward and inverse Fourier transforms respectively. Hence, we can directly see that the Fourier and inverse Fourier transforms transpose the visibilities to and from the visibility and image spaces, respectively.

A single baseline measures a point in the *uv* plane, and the visibility obtained gives a single Fourier component of the sky brightness distribution. By stacking baselines of different lengths, I can measure more and more Fourier components until an adequate measure of the sky brightness distribution can be obtained by Fourier inversion. Due to the inverse relationship of Fourier conjugate variables, longer baselines measure the smaller angular scales of the sky, while shorter

baselines measure the larger scales. By discretely sampling the *uv* plane with individual baselines and utilising the Earth's rotation so that each baseline traces a path in the *uv* plane, I can gradually build up enough Fourier components to accurately image the sky.

As explained above, interferometers measure or sample the visibility function at discrete points in the *uv* plane. If I could continuously sample the entire *uv* plane, I would have infinitely many Fourier components and be able to reproduce the sky exactly; unfortunately, this is not physically possible. I hence describe the sampled visibilities by V(u,v)S(u,v), where S(u,v) is some weighted sampling function and depends on the array configuration, among other things. The weights applied to the sampling function interpolate the visibilities in the unsampled regions of the *uv* plane in different ways in order to achieve particular science goals. Commonly used weighting schemes are `natural`, `uniform`, or `Briggs` (Briggs, 1995). `Natural` weighting gives equal weight to all sampled visibilities. However, since interferometers usually sample the larger angular scales more densely (i.e. have more short baselines than long), this scheme gives the best sensitivity to large angular scales (and hence diffuse emission) but the poorest angular resolution and largest PSF sidelobes. `Uniform` weighting gives equal weight to each angular scale irrespective of sample density and results in the smallest possible angular resolution; however, the sensitivity worsens because densely sampled angular scales are down-weighted to make the weights uniform with respect to the under-sampled scales. `Briggs` weighting provides a tunable parameter called the `Robust` value that smoothly varies from almost uniform at a value of -2 to almost natural at +2. A `Robust` value close to zero is often used as a compromise sensitivity, resolution and sidelobe levels. An additional type of weighting can be achieved through *uv-tapering*, where a Gaussian function is convolved with the visibilities of particular angular scales to down-weight them relative to the rest; the effect suppresses artefacts arising from poorly sampled scales.

The 2D inverse Fourier transform of the sampled visibility function results in a distorted version of the sky brightness distribution called the dirty image $I_\nu^D(l,m)$:

$$\mathscr{F}^{-1}\{V(u,v)S(u,v)\} = I_\nu^D(l,m). \tag{3.7}$$

Now, the convolution theorem states that the product in one domain is the convolution in the other. Therefore, the dirty image is equivalent to convolving the true sky brightness distribution with the Fourier transform of the sampling function:

$$I_\nu^D(l,m) = I_\nu(l,m) * s(l,m), \tag{3.8}$$

where $s(l,m) = \mathscr{F}\{S(u,v)\}$. The Fourier transform of the sampling function is called the point spread function (PSF) or the dirty beam of the array and is specific to the interferometer and weighting scheme used. A 2D sinc-like function describes it in the image-space (or a rectangular-like function in the *uv*-space) and describes the instrument's response to a point source, where the sinc's positive and negative *sidelobes* are artefacts resulting from the incomplete sampling. Since the sky brightness distribution can be decomposed into the sum of individual point sources, the dirty beam gives a PSF to each observed source, whereas brighter sources usually have larger sidelobes. From the above equations, it can be seen that the 2D Fourier transform of the sampled visibility function results in the true sky brightness distribution convolved with the dirty beam:

$$\mathscr{F}\{V(u,v)S(u,v)\} = I_\nu(l,m) * s(l,m). \tag{3.9}$$

The dirty image is named as such because it depicts the sky brightness distribution corrupted by the dirty beam (the discretised sampling). The dirty beam is fitted and subtracted from the dirty image to correct for (or *clean*) the artefacts and noise caused by the PSF sidelobes through a process called deconvolution. Usually, some variant of the CLEAN algorithm, e.g. the Hogbom, Clark or Cotton-Schwab algorithms (Högbom, 1974; Clark, 1980; Schwab, 1984), is used to iteratively subtract the dirty beam until its effects are adequately removed. This algorithm assumes that the radio sky can be represented by many point sources, described by indiviual delta functions, in an otherwise empty field. For example, the Cotton-Schwab algorithm is used in the popular imaging software WSClean (Offringa et al., 2014), and its logic is as follows:

1. Compute the dirty beam (PSF) and dirty image. Set the initial model (or clean component

list) to be empty.

2. Predict a set of model visibilities by applying the inverse Fourier transform to the above, essentially inverting equation 3.9. This step is skipped during the first major cycle, since the initial model is empty.

3. Subtract the predicted model visibilities from the original ones to obtain residual visibilities. Fourier transform these visibilities to obtain a residual image which represents all the flux not yet deconvolved by the algorithm (i.e. not in the model), plus calibration artefacts and thermal noise. This step is skipped during the first major cycle, since at that point the residual image is simply the dirty image itself.

4. Identify the peak of the residual image. Add this peak value, multiplied by a small number (~0.1) called the *loop gain* to the model (or equivalently the clean component list), and subtract the dirty beam times the loop gain, centred on the location of the peak, from the residual image. In effect, this transfers a fraction (given by the loop gain) of the flux from the residual image into the model. This step is called the *minor cycle* and is repeated until some minor cycle stopping criterion is reached (typically, when the peak value drops below a certain fraction, 10-15%, of the initial peak value).

5. Steps (2)-(4) are called the *major cycle*. The major cycle is repeated until some major cycle stopping criterion is reached.

6. The final model image is convolved with an elliptical Gaussian. The Gaussian is called the fitted, clean or restored beam. Its size (typically obtained by fitting a Gaussian to the main lobe of the dirty beam) is determined by the uv coverage of the observation and imaging weights and describes the image resolution. This convolved model image is added to the final residual image to give the final restored image.

Several techniques have been developed to improve the computational efficiency and accuracy of the above imaging logic. One such technique is multi-frequency synthesis (MFS, Conway et al., 1990; Sault & Conway, 1999) which entails breaking the total bandwidth into a number of sub-

bands, forming an image per sub-band and combining them at the very end to give the restored image at the central bandwidth frequency. The effect is to increase the relative *uv* coverage in each sub-band frequency range so that the combined image has an overall greater signal-to-noise. The sub-band images can be used to perform an in-band spectral analysis of the sources in the FoV. Other techniques include multi-scale cleaning and auto-masking of the 'real' sources to improve the deconvolution (Offringa & Smirnov, 2017).

The final image should represent the true sky brightness distribution to within our stopping criteria. A source precisely the size of the restored beam is called a 'point source', while a source smaller is termed 'resolved' and any larger is termed 'unresolved' (a Gaussian function can describe a resolved source, but an unresolved source may not be. However, the true sky brightness distribution contains several effects that bias the measurements of the science targets/cases of interest.

## 3.2 The Radio Interferometer Measurement Equation (RIME)

The electromagnetic waves measured by the interferometer are not the original waves emitted by the astrophysical source. Instead, the original signal is contaminated by successive layers of propagation effects as it makes its way to the interferometer, such as from the intervening media like the interstellar medium and atmosphere and system electronics and RFI. An efficient way to correct these effects is needed to obtain accurate sky images and measurements of the astrophysical sources.

Jones calculus (Jones, 1941) is a mathematical framework that describes these propagation effects. The Radio Interferometer Measurement Equation (RIME) is then derived using this framework to describe how these effects corrupt the original signal into that which I observe (Hamaker et al., 1996). I then solve the RIME to unravel the true astrophysical signal of interest. In its general form, the RIME is given as

$$V_{pq} = J_p B J_q^H, \tag{3.10}$$

where $V_{pq}$ is the visibility matrix that contains the voltages measured between antennas $p$ and $q$, $B$ is the brightness matrix which contains the intrinsic properties of the source (e.g., flux and polarisation), and $J_p$ and $J_q$ denote a chain of generic Jones matrices multiplied together to represent the cumulative corruption along the signal paths to antennas $p$ and $q$, respectively. Some Jones terms depend on the direction in the sky from which the astrophysical signal originates, while some are not. The direction-independent (DI) terms include the $P$, $K$, $D$, $B$ and $G$ Jones matrices. Respectively, they describe the parallactic angle rotation, geometric delay, polarisation leakage, bandpass gains and receiver gains that the signal experiences, termed DI effects (DIEs). Direction-dependent (DD) terms include $F$, $Z$ and $E$ matrices, which respectively describe the Faraday rotation, ionospheric phase delay and the effect of the telescope's primary beam (described as DD effects, DDEs). In the limiting cases of a small FoV and/or a co-planar array (i.e. flat-sky approximation), the DD terms can be neglected so that the RIME takes the form of a 2D Fourier transform between $V_{pq}$ and $B$, multiplied by the chain of DI Jones matrices. However, the non-coplanarity and wide FoV of modern radio telescopes break these limiting cases and introduce significant direction-dependence to the observations so that the full DD RIME is given as:

$$V_{pq} = G_p \left( \int_m \int_l \frac{1}{n} E_p B(l,m) E_q^H(l,m) e^{-i2\pi(u_{pq}l + v_{pq}m + w_{pq}(n-1))/\lambda} dl dm \right) G_q^H, \tag{3.11}$$

(see e.g., Smirnov, 2011a,b,c,d, for exercises in the practical application thereof). Here, $G$ and $E$ denote the chained DI and DD Jones terms, respectively; n and w denote the orthogonal planes to the $lm$ and $uv$ planes. This equation is not a Fourier transform and is very computationally expensive to calculate explicitly. This is the so-called 'calibration problem' of wide-field, wide-band imaging.

## 3.3 Calibration–Theory

Calibration is the process of correcting and solving for the individual Jones terms in the RIME to unveil the intrinsic properties of the science targets – $B(l,m)$ in equation 3.11. Calibration starts

in the instrument design stage and ends in the final data presentation. Calibration specific to the science case is required before any meaningful measurements can be undertaken. Two kinds of calibration are essential in this work: DI and DD calibration. Cross-calibration (first-generation calibration, or 1GC) and DI self-calibration (second-generation calibration, 2GC) address the former. DD self-calibration tries to correct the errors incurred when neglecting the DDEs during the previous calibration stages (i.e. tries to solve equation 3.11). Below I describe each generation of calibration, focusing on only what is needed to understand the data reduction in Chapter 4.

### 3.3.1 Cross-calibration (1GC)

Along with the target source, calibrator sources are observed for the purpose of cross-calibration. Here, primary and secondary calibrators are observed and compared to models of themselves to derive baseline-frequency-time dependent delay, complex gain and complex bandpass corrections to the observational data, which are then applied to the target data. The primary calibrator is usually a well-characterised source that the observatory monitors over time to maintain a robust local sky model (lsm) for it, for example, J1934-6342[1], and is used to set all data onto the same absolute flux scale.

Since the RIME terms are complex, they require a correction for both amplitude and phase. Delay calibration solves the $K$-Jones term and corrects the baseline-frequency dependent geometric and signal-processing temporal delays across the array. These manifest as a gradient in phase as a linear function of frequency and can be caused by, for example, inaccurate antenna positions. Gain calibration solves the $G$-Jones term and corrects the effect of baseline-time-dependent antenna electrical gains on the signal, of which phase is more variable than the amplitude. Such inconsistencies in the gains can be caused by, for example, receiver power level settings and changing atmospheric conditions. Bandpass calibration solves the $B$-Jones term and corrects the baseline-frequency-dependent dispersion of signals at different frequencies relative to each other over the observing bandwidth – caused by, for example, system electronics and poor atmospheric condi-

[1] https://skaafrica.atlassian.net/wiki/spaces/ESDKB/pages/1481408634/Flux+and+bandpass+calibration

tions. As mini-halos are generally unpolarised, I have omitted any discussions about the polarisation of an astrophysical signal. Polarisation calibration is a fascinating and complicated topic but not necessary in our case, so I focus only on the Stokes *I* signal. The standard Common Astronomy Software Applications (CASA McMullin et al., 2007) tasks `setjy, gaincal, bandpass, fluxscale, applycal` are used to derive and apply the calibration solutions.

### 3.3.2 DI Self-calibration (2GC)

After 1GC, the target data is ready for imaging. However, significant calibration and imaging artefacts are usually still present because of some remaining bad data, unmodelled sources that were not captured by the 1GC, or DDEs. The 'depth' (or quality) of a continuum image can be expressed as its dynamic range (DR), often calculated as the maximum pixel value divided by the global root mean square (rms) noise or the absolute value of the minimum pixel value. The rms describes the level at which I cannot discern noise from physical emission and is calculated as the square root of the mean squared with respect to each pixel value in the residual image. A high DR value indicates that the image has a low noise level and well-characterised PSF sidelobes despite having strong sources present to amplify these impurities, indicating a better or 'deeper' image. Self-calibration is the process of iteratively using the target data itself to further refine the calibration solutions and thus reduce the image artefacts and obtain a deeper image with less noise in each iteration.

Self-calibration is first performed in a direction-independent manner, addressing only the DI terms of the RIME. An imaging software, such as WSClean (Offringa et al., 2014) is used to generate an initial image of the cross-calibrated target data and a corresponding clean components list (or sky model) in which the brightest pixels are included to represent a model of the 'real' sky. A mask of the initial image is generated with a threshold scaling with the image noise. A threshold relative to the global or local noise can be defined. The latter is usually needed for images of high DR so that bright artefacts are not masked while the fainter emission in a different region is masked. The pixels included in the mask are considered part of any 'real' sources, and all artefacts

are excluded. The cross-calibrated data is re-imaged with the mask so that the corresponding sky model traces the masked pixels and is stored in its own column in the MS, usually called `MODEL_DATA`. This column is fed into a self-calibration software (such as CubiCal, Kenyon et al., 2018) that fits the observed visibilities to match the sky model so that the data corresponding to DI errors can be corrected/flagged out. The resulting `CORRECTED_DATA` is stored in a new column and imaged – ending the first round of DI self-calibration. A tighter and more accurate source mask can then be generated and applied to re-image and generate a more accurate sky model so that more accurate calibration solutions can be derived and imaged again; this is the second round of DI self-calibration. Two to three rounds of such calibration are often needed before the improvement plateaus, usually with the solution intervals defined for deriving the corrections being reduced (in time and frequency) in each round to derive finer and finer corrections. Auto-masking techniques (such as described in Offringa & Smirnov, 2017) can reduce the number of imaging runs needed.

Different types of solutions can be derived for specific cases – correcting for the amplitude and phase of each Jones term is not always necessary. For example, suppose only minimal artefacts are present after 1GC, and there are no bright sources in the field; in that case, solving only for the phase component of the *G*-Jones term is usually sufficient – and further improvements would need to be found in a DD manner. However, in the presence of a very bright source, the visibility correlations can bleed into each other causing second-order polarisation leakage. If a high DR is required in this case, i.e. a low noise despite the presence of the strong corrupting source, then second-order leakage effects become non-negligible. In such a case, solving for the complex 2x2 matrix that describes both the amplitude and phase of each correlation would be necessary. Often the 1GC bandpass corrections are enough for that type of calibration, so only the G-Jones (and optionally *K*-Jones, if there are significant artefacts in the field) corrections are usually solved.

### 3.3.3 DD Self-calibration (3GC)

With modern radio telescopes becoming increasingly sensitive, our calibration and imaging techniques have needed to expand to deal with the added complications. DD self-calibration can

produce multi-directional solutions that correct for the DDEs found in the RIME, thereby reducing residual artefacts and creating deeper images so that lower surface brightness emission can be detected. The procedure is analogous to 2GC, image a rigorous model, derive calibration solutions and apply solutions in further imaging rounds. However, explicitly solving for the DD terms is computationally expensive and has only become functionally viable in the last few years.

Several algorithms have been developed to try to tackle the problem (see, for example, Yatawatta et al., 2008; Intema et al., 2009; Noordam & Smirnov, 2010). However, most perform poorly on low signal-to-noise data, giving non-physical results, and are ill-conditioned (very sensitive to changes in the input values, leading to solution instability). However, Tasse (2014a,b) describes an algorithm that addresses these issues, called the Kalman Filter Calibration Algorithm (KAFCA). Most of the previous algorithms were iterative sequences based on the least squares method, i.e. minimising the sum of the squares of the error between the model fit and data. However, KAFCA implements recursive non-linear Kalman filters (Kalman, 1960; Julier & Uhlmann, 1997; Wan & Van Der Merwe, 2000) to directly estimate the physical DD RIME terms by minimising the mean of the square of the error on the fitted model itself, thereby 'tracking' the error rather than solving for it.

Further, it exploits Wirtinger complex differentiation to perform the computations relatively cheaply. Wirtinger complex differentiation is an application of partial differentiation to complex numbers and variables that becomes analogous to the ordinary differentiation of real-valued functions (Wirtinger, 1927; Kreutz-Delgado, 2009). They packaged their technique in the calibration software killMS[2], and Tasse et al. (2018) then developed an accompanying imager called DDFacet[3]. This imager breaks the FoV into smaller facets, computing a dirty beam per facet, all on a single plane tangential to the sky. It approximates the wider FoV with these many narrow-field images while taking kMS solutions into account to perform wide-band, wide-field DD spectral deconvolution. I use this two software in our data reduction to produce the deepest possible images from the available observations.

[2]https://github.com/saopicc/killMS
[3]https://github.com/saopicc/DDFacet

A known issue with 3GC is that it can worsen the effect of flux suppression/absorption: flux from faint unmodelled sources may be absorbed by the antenna gains and often transferred to the brighter modelled sources, thereby decreasing the observed flux density of the faintest sources and increasing that of the brighter ones (see, e.g., Sob et al., 2019; Grobler et al., 2014; Wijnholds et al., 2016). For further generalized discussions on DDEs and 3GC, see e.g., Noordam & Smirnov (2010); Smirnov (2011a,b,c,d); Smirnov & Tasse (2015).

**Primary beam correction**

Of particular importance in modern wide-field, wide-band interferometers is the concept of primary beam correction. It is the first non-trivial DDE in the calibration problem. The primary beam can be thought of as the telescope's response or sensitivity as a function of direction from the pointing centre its effect is basically to attenuate the astrophysical signal. The exact response function depends on the array elements and configuration. In principle, due to real-world effects such as slight surface defects and antenna pointing offsets, each antenna will have a slightly different directional response; however, it is assumed that for a heterogeneous array (where all antennas have exactly the same design) such as MeerKAT, the effective primary beam response can be approximated by that of an average element. As an example, the primary beam response for the parallel-hand cross-correlations of the MeerKAT telescope has a form similar to that of a 2D sinc function when projected onto the sky. The diameter of the primary beam can be determined by equation 3.1, using the central observing frequency and the diameter of a single dish. The MeerKAT primary beam is $\sim 1^{\circ}$ in diameter at L-band and corresponds to the main lobe of the 2D sinc-like function. de Villiers & Cotton (2022) gives detailed measurements that characterise the MeerKAT L-band primary beam.

In the direction of the pointing centre, the effect of the primary beam is negligible. However, further out, the primary beam induces a frequency and angular distance dependence on the spectral structure of the brightness of modelled sources. These dependencies are modelled by the obser-

vatory, which is then made publicly available to users[4]. Image-plane primary beam correction consists of simply dividing this model out of the sky brightness distribution during the convolution/deconvolution imaging steps to ensure the image's fluxscale across the bandwidth within the primary beam region has not been biased by the instrument's directional response (effectively a form of normalisation). This means that any regions imaged outside the primary beam can't be reliably used for science other than to study imaging techniques. By convention, in this work, whenever primary beam correction has been applied, the images are referred to as being in the *intrinsic* fluxscale, otherwise in the *apparent* flux scale. Additionally, the primary beam rotates as a function of time due to parallactic angle rotation and is made more complex by antenna pointing errors. Pointing errors occur when the correlator is thought to be pointing in a certain direction but is slightly offset, which can exacerbate DDEs. To account for the rotation, DDF evaluates the primary beam per facet and kMS derives model corrections within a given time and frequency interval.

## 3.4 Source subtraction

Point source subtraction is an important aspect in the study of diffuse radio emission because point-like sources can obscure the view and bias the measurements of the emission of interest. In fact, source subtraction is arguably even more critical when considering mini-halos than any other diffuse emission because a larger fraction of the emission is contaminated by the point-like sources. In addition, only for mini-halos is there discussion about the production mechanism involving the embedded sources as some major roleplayer. Thus, accurately and precisely separating the compact and diffuse emission in mini-halo studies is of paramount importance if a firm grasp of the production mechanism (and the other properties of the mini-halo, e.g. morphology, flux density and spectral index) is to be had. I use the terms 'source subtraction' and 'point source subtraction' interchangeably because any emission other than the mini-halo itself, be it resolved or unresolved, is intended to be subtracted.

[4] `https://archive-gw-1.kat.ac.za/public/repository/10.48479/wdb0-h061/index.html`

As mini-halos are found in the cores of galaxy clusters, the embedded source is often a BCG and often has radio flux comparable to that of the surrounding mini-halo itself. It, and any associated jets or lobes, needs to be removed in order to obtain an uncontaminated and unbiased image of the mini-halo. Source subtraction can be done either in the image plane or the visibility plane. I choose the latter because it conserves the flux density of the underlying diffuse emission. This approach involves subtracting the modelled compact sources that are imaged at a high resolution directly from the MS visibilities and then re-imaging the remaining data at the original resolution (examples of this approach in the context of mini-halo studies are Biava et al., 2021; Riseley et al., 2022a). However, any form of subtraction will inevitably introduce some measurement bias based on whether the compact emission was under or over-subtraction for a given source. To account for this, I include a subtraction uncertainty in our physical measurements which will be described in Chapter 4.

# Chapter 4

# MeerKAT Observations: Data Reduction and Analysis

We describe the set of observations that I work on, the data reduction and point source subtraction, the resulting images and physical measurements and how they fit into the context of current mini-halo literature. This Chapter is based on the work presented by Trehaeven et al. (accepted, manuscript ID MN-22-3893-MJ).

## 4.1 Sample selection

A sample of five galaxy clusters was selected from the literature and observed by MeerKAT during its first OpenTime Call in 2019 (proposal ID: SCI-20190418-KA-01). I present the first analysis of these data.

The clusters were chosen based on two criteria; first, the status of the hosted diffuse emission at the time of proposal submission, being either a newly confirmed, candidate or uncertain detection. Second, the declination of the host cluster, ranging from the MeerKAT's latitude of $-30°$ to $+30°$ to allow for possible future synergy with northern hemisphere interferometers like LOFAR and the uGMRT, particularly in mini-halo studies. However, this work focuses on the calibration and imaging of these observations, and any synergy between individual radio telescopes is beyond

the scope of this work. Table 4.1 summarises the known physical properties of each gathered from the literature. ACO 3444 was chosen because Giacintucci et al. (2019) confirmed the presence of a mini-halo via the analysis of archival VLA L-band observations, and more diffuse emission was expected to be detected with MeerKAT because of its denser coverage of short baselines. Additionally, this cluster is located at a declination similar to the longitude of the MeerKAT telescope ($\sim -30°$). This will result in the widest possible uv-coverage and hence the best sensitivity for a given observation duration. The central diffuse emission within ACO 1413, ACO 1795 and MACS J1115.8+0129 were classified as candidate mini-halos at the time. The first two are located at a declination near the northern limit of MeerKAT's observing range, and the latter is near the celestial equator. These targets were proposed with the intention of confirming the nature of the hosted diffuse radio emission. However, since proposal submission, the first and last of these candidates have been confirmed by Savini et al. (2019) and Giovannini et al. (2020), respectively. The last of these, MACS J2140.2-2339, was chosen because it is a massive CC cluster within the optimal MeerKAT observing range and had no prior radio observations. Giacintucci et al. (2017) studied a mass-limited sample of galaxy clusters and concluded that most (∼80%) of the massive CC clusters possessed a mini-halo; hence, this last cluster was identified with its mass and southerly declination to have the potential to be the first new mini-halo detection with MeerKAT. This was presented in Trehaeven et al. (2023). Finally, ACO 1413 had already been observed by LOFAR in Savini et al. (2018), and Riseley et al. in prep aim to provide an in-depth MeerKAT+LOFAR study of the diffuse radio emission in this exciting cluster. The sample varies in redshift from 0.06 to 0.35 and has mass $M_{500} \gtrsim 5 \times 10^{14}\ M_{\odot}$, all within the typical range of the confirmed mini-halo sample.

The observations considered were conducted in mid-2019, with the entire array, a total bandwidth of 856 MHz centred at 1283 MHz (L-band), full 4096 channelisation, and an 8-second dump rate – except for MACS J1115.8+0129 which had a 2-second dump rate (reason not given in the proposal or observation logs). A higher dump rate can be beneficial when high-resolution imaging is required (SARAO time smearing simulation report). However, I treat all clusters to the same

Table 4.1: Physical properties of the cluster sample. Columns: cluster name, redshift, angular-to-physical scale calculated for our cosmology, cluster mass is taken from Planck Collaboration et al. (2014) unless stated otherwise, core X-ray morphology, core radio morphology and literature references. Taken from Trehaeven et al. (accepted).
MH = mini-halo, cMH = candidate mini-halo.
* Taken from Piffaretti et al. (2011).
** New detection from this work.
Ref.: (1) Savini et al. (2019); (2) Giacintucci et al. (2017), (3) Kokotanekov et al. (2018); (4) Giacintucci et al. (2019); (5) Giovannini et al. (2020)

| Name | z | Scale (kpc/″) | $M_{500,\mathrm{SZ}}$ ($10^{14} M_{\odot}$) | X-ray morphology | Radio morphology | Ref. |
|---|---|---|---|---|---|---|
| ACO 1413 | 0.143 | 2.51 | $5.98^{+0.38}_{-0.40}$ | nCC | MH | 1, 2 |
| ACO 1795 | 0.062 | 1.20 | 4.54±0.21 | CC | cMH | 2, 3 |
| ACO 3444 | 0.254 | 3.96 | $7.6\ ^{+0.5}_{-0.6}$ | CC | MH | 2, 4 |
| MACS J1115.8+0129 | 0.350 | 4.94 | 6.4 ±0.7 | CC | MH | 2, 5 |
| MACS J2140.2−2339 | 0.313 | 4.59 | 4.7* | CC | MH** | 5 |

Table 4.2: Observation details. Columns: cluster name, RA, Dec, observation date, and observation time on-target. Taken from Trehaeven et al. (accepted).

| Name | RA (h:m:s, J2000) | DEC (d:m:s, J2000) | On target time (minutes) | Observation date |
|---|---|---|---|---|
| ACO 1413 | 11:55:19.40 | 23:24:26.0 | 117 | 10 August 2019 |
| ACO 1795 | 13:48:55.00 | 26:36:01.0 | 240 | 16, 17 June 2019 |
| ACO 3444 | 10:23:54.80 | -27:17:09.0 | 228 | 20, 26 July 2019 |
| MACS J1115.8+0129 | 11:15:54.90 | 1:29:56.0 | 93 | 2 August 2019 |
| MACS J2140.2-2339 | 21:40:15.20 | -23:39:40.0 | 87 | 30 June 2019 |

reduction procedures unless otherwise stated. The observation details are summarised in Tables 4.2 and 4.3. The primary calibrators (used for bandpass calibration and flux-scaling) were scanned once at the start of each observation block for 10 minutes. The secondary calibrators (used for the delay and gain calibration) and targets were then scanned alternately for 2 and 15 minutes, respectively. Observations for ACO 1795 and ACO 3444 were split between two equal-time observation blocks on consecutive days and weeks, respectively.

Table 4.3: Observation details continued. Columns: cluster name, primary calibrator, secondary calibrator. Taken from Trehaeven et al. (accepted).

| Name | Primary calibrator | Secondary calibrator |
|---|---|---|
| ACO 1413 | J0408-6545 | J1120+1420 |
| ACO 1795 | 3C286 | 3C286 |
| ACO 3444 | J0408-6545 | J1051-2023 |
| MACS J1115.8+0129 | J0408-6545 | J1058+0133 |
| MACS J2140.2-2339 | J1939-6342 | J2152-2828 |

## 4.2 Calibration in Practice

Here I describe the practical application of the calibration techniques discussed in Section 3.3. All raw radio data processed in this project were downloaded from the SARAO archive[1] and remain publicly available. The KATDAL[2] (Karoo Array Telescope Data Access Library) package is used to convert early MeerKAT data into an easily accessible form. I used its `mvftoms.py` script to download and convert the data from the native MeerKAT Visibility Format (MVF) to the standard CASA Measurement Set (MS) format. While downloading, I applied the 'cam' and 'ingest_rfi' flagging strategies, which were generated by the telescope's control and monitoring system for early continuum data. During the observations, the calibrator sources J0408-6545 and J1939-6342, respectively, had a positional offset of 0.52″ and 2.00″ with respect to where the antennas were pointed and the correlator phased. This issue of poor calibrator positions is known in early MeerKAT observations[3]. The problem was corrected immediately after download by parsing each MS and the correct source coordinates into CASA's `fixvis` task so that it could shift the visibilities to the correct phases. In order to spot obvious errors in the data, I plotted the auto-correlation amplitudes (the antenna voltages multiplied by itself) versus both time and antenna using CASA's `plotms` but did not identify any significant abnormalities. I then proceeded to calibrate the data.

[1] `https://archive.sarao.ac.za`
[2] `https://github.com/ska-sa/katdal`
[3] `https://skaafrica.atlassian.net/wiki/spaces/ESDKB/pages/1481015302/Astrometry`

### 4.2.1 1GC + 2GC: CARACal

We used the Containerized Automated Radio Astronomy Calibration (CARACal Józsa et al., 2020))[4] pipeline to streamline the 1GC and 2GC procedures. CARACal is a Python-based pipeline developed to reduce spectral and continuum MS data, optimised specifically for MeerKAT data, and calls on specific software to perform the reduction. Users interact with CARACal via a configuration script, where instructions for each part of the calibration process are neatly and sequentially contained. Before any meaningful calibration is performed, the pipeline first copies all sources into separate 'calibrators' and 'targets' MS files so that the original data is always kept as a backup and then flags the calibrator data. CARACal was told to use CASA's `flagdata` task to flag the known problematic ranges of the spectral window (856~880 MHz, 1658~1800 MHz, 1419.8~1421.3 MHz), auto-correlations and any shadowed antennas, and Tricolour[5] (Hugo et al., 2022) for persistent RFI. Tricolour is an automated flagging software developed specifically for MeerKAT data. Here, I used a particularly strict default flagging strategy from the CARACal MeerKAT files[6] to ensure that all calibrator data carried into the calibration process was as clean as possible. In order to improve image DR and the detection of faint diffuse emission, I perform 3GC on all data, even if there are no major artefacts left in the field after 2GC. Below I describe our calibration process applied to each observation in the sample.

#### 1GC

As explained in Section 3.3, calibrator sources are used to derive corrections for various instrumental and propagation effects that corrupt the underlying astrophysical signals (e.g., antenna gain fluctuations and atmospheric conditions). These corrections are applied to the target to mitigate the observational errors, known as cross-calibration. I told CARACal to perform its default

[4] `https://github.com/caracal-pipeline/caracal`

[5] `https://github.com/ska-sa/tricolour`

[6] `https://github.com/caracal-pipeline/caracal/blob/master/caracal/data/meerkat_files/stalin.yaml`

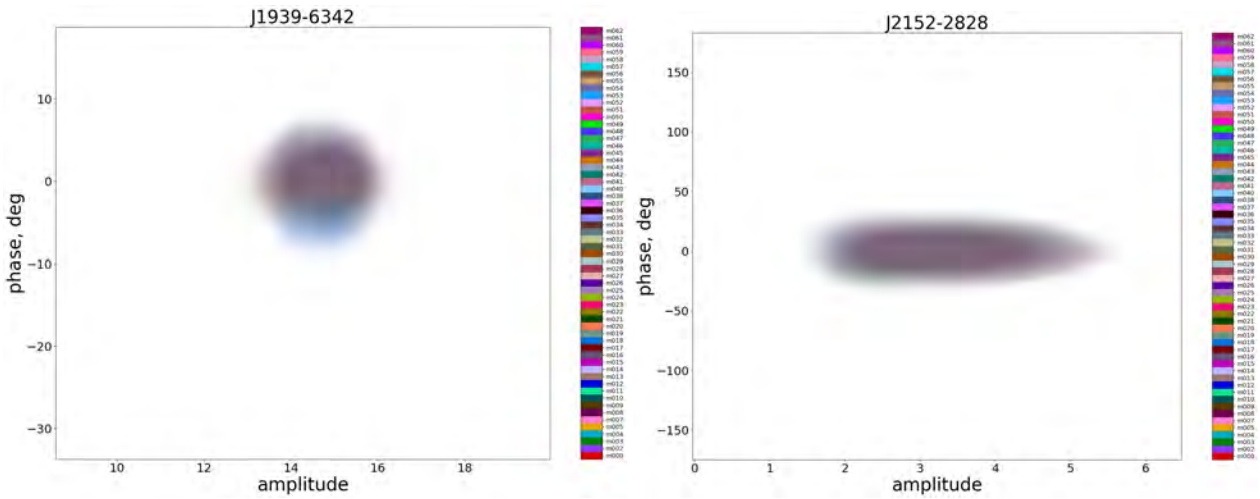


Figure 4.1: Phaseball plots for the MACS J2140.2-2339 calibrators. The corrected visibilities of each calibrator are plotted in the phase vs amplitude plane for the XX correlation, coloured per antenna. Amplitudes are in units of Jy. *Left:* primary calibrator J1939-6342. *Right:* secondary calibrator of J2152-2828.

continuum cross-calibration recipe[7], and exact parameters are listed in Table A.1 in the Appendix. Thus, CARACal loaded the respective lsm into the MS and used CASA's `gaincal` and `bandpass` tasks to derive delay, complex-gain and complex-bandpass corrections to get the measured primary calibrator visibilities as close as possible to the lsm. The bandpass solutions were applied to the secondary calibrator while its delay and complex-gain corrections were calculated. The above was repeated after a mild automated flagging with `flagdata`. A single calibration solution was calculated for each calibration term (delay, gain, bandpass) for each calibrator in each round, except for the primary's second round of delay and gain corrections, which had a solution interval of 60 s each. The secondary gain solutions were scaled with reference to the primary calibrator's flux using CASA's `fluxscale` task.

Before the cross-calibration solutions were applied to the target, I inspected them and the corrected calibrator data to ensure they were as expected. To this end, CARACal can output many diagnostic plots using different plotters. I used `shadeMS`[8] to plot the corrected calibrator visibilities. A very useful partner software to CARACal is the (Radio) Python Astronomy Data Reduc-

[7] `https://github.com/caracal-pipeline/caracal/blob/master/caracal/sample_configurations/meerkat-continuum-defaults.yml`

[8] `https://github.com/ratt-ru/shadeMS`

tions Examiner `radiopadre`[9], which is a custom Jupyter kernel that allows for quick and easy visualisation of radio astronomy data products in a notebook web browser tab. I used this software to display and inspect the outputted diagnostic plots. Figure 4.1 shows the corrected amplitude vs phase (the so-called 'phaseball' plot) of a single parallel-hand correlation (XX), for the primary and secondary calibrators of MACS J2140.2-2339, for each antenna. I expect these plots to depict tight balls centred around a zero phase and an amplitude equal to the calibrator's known flux density; any significant scatter would mean that something went wrong in the derivation of the calibration solutions. MeerKAT gives information on all its designated calibrator sources[10]. It is known that this primary calibrator has an L-band flux density of $\sim$ 14.5 Jy with almost no dependence on frequency in the MeerKAT band and the secondary has a flux density of $\sim$ 3 Jy but with a relatively steep dependence on frequency. In Figure 4.1, the corrected visibilities of both the primary and secondary calibrators are tightly centred around the fiducial values in amplitude, and zero in phase, with minimal scatter (the elongation of the secondary's amplitudes is expected and is due to its frequency dependence); thus, I can safely say that the calibrator data was also sufficiently corrected.

Finally, the complex-bandpass solutions of the primary and the delay and flux-scaled complex-gain solutions of the secondary were applied to the target data. This target data was then frequency-averaged over five channels to save on storage space and future processing time. This is justified as I am only interested in continuum science and not any specific spectral lines, and the resulting channel width of $\sim$1 MHz is still much too small to cause significant bandwidth smearing–the result of spectrally averaging interferometric data too coarsely such that sources are radially distorted/elongated in the image plane (Bridle & Schwab, 1999). The cross-calibrated target data was flagged similarly to the calibrator data but with a slightly more relaxed flagging strategy[11]. At the end of 1GC, approximately 65-75% of the target data was flagged which is high for MeerKAT but not unreasonable (perhaps our flagging strategies were too strict). The only exception to this

[9] https://github.com/ratt-ru/radiopadre

[10] `https://skaafrica.atlassian.net/wiki/spaces/ESDKB/pages/1452310549/Calibration`

[11] `https://github.com/caracal-pipeline/caracal/blob/master/caracal/data/meerkat_files/gorbachev.yaml`

procedure was ACO 1795, whose primary and secondary calibrators were both 3C286 – which does not have an lsm yet. In this case, I used CASA's `setjy`, externally from CARACal, to set the model using the polarisation information from Perley & Butler (2017) and the updated polarimetry properties from Table 7.2.7 from the NRAO website[12]. Thereafter, I proceeded similarly to the rest of the clusters.

**2GC**

Direction-independent self-calibration is the process of using the target data itself to refine the calibration solutions and hence reduce imaging artefacts. This is done by imaging the cross-calibrated target data and deriving finer and finer gain solutions using the modelled visibilities. I used the CARACal defaults of imaging with WSClean[13] (Offringa et al., 2014) and producing self-calibration solutions with CubiCal [14] (Kenyon et al., 2018). I performed three rounds of phase-only gain self-calibration (GainDiagPhase, Table A.1). In each iteration, I imaged a 2.5° squared area spanning 6000 pixels (scale 1.5″/pixel). I used MFS with five sub-band images, `Robust 0` weighting, a 2nd-order spectral polynomial fit, and WSClean's multi-scale cleaning and auto-masking routines. The auto-masking thresholds decreased in each iteration, set to 30, 15, 8, and 3 times the residual image noise calculated by the routine, into which the absolute cleaning threshold was 0.5 times this noise. Normally, cleaning below the noise level is not recommended as it could lead to mistaking noise or artefacts for real emission. However, WSClean auto-masking is scale-dependent, estimating the noise and generating masks in a set of automated scales, allowing us to clean below the noise without confusion, resulting in reliably lower residuals (Offringa & Smirnov, 2017). The deconvolution was terminated either after 1,000,000 minor iterations or once the absolute cleaning threshold was reached, whichever came first. After each imaging round, I fed the model data into CubiCal to produce phase-only self-calibrated corrected data. The solutions were solved with decreasing time intervals per calibration round (30-, 15-, 3-seconds) over the

[12] `https://science.nrao.edu/facilities/vla/docs/manuals/obsguide/modes/pol`
[13] `https://gitlab.com/aroffringa/wsclean`
[14] `https://github.com/ratt-ru/CubiCal`

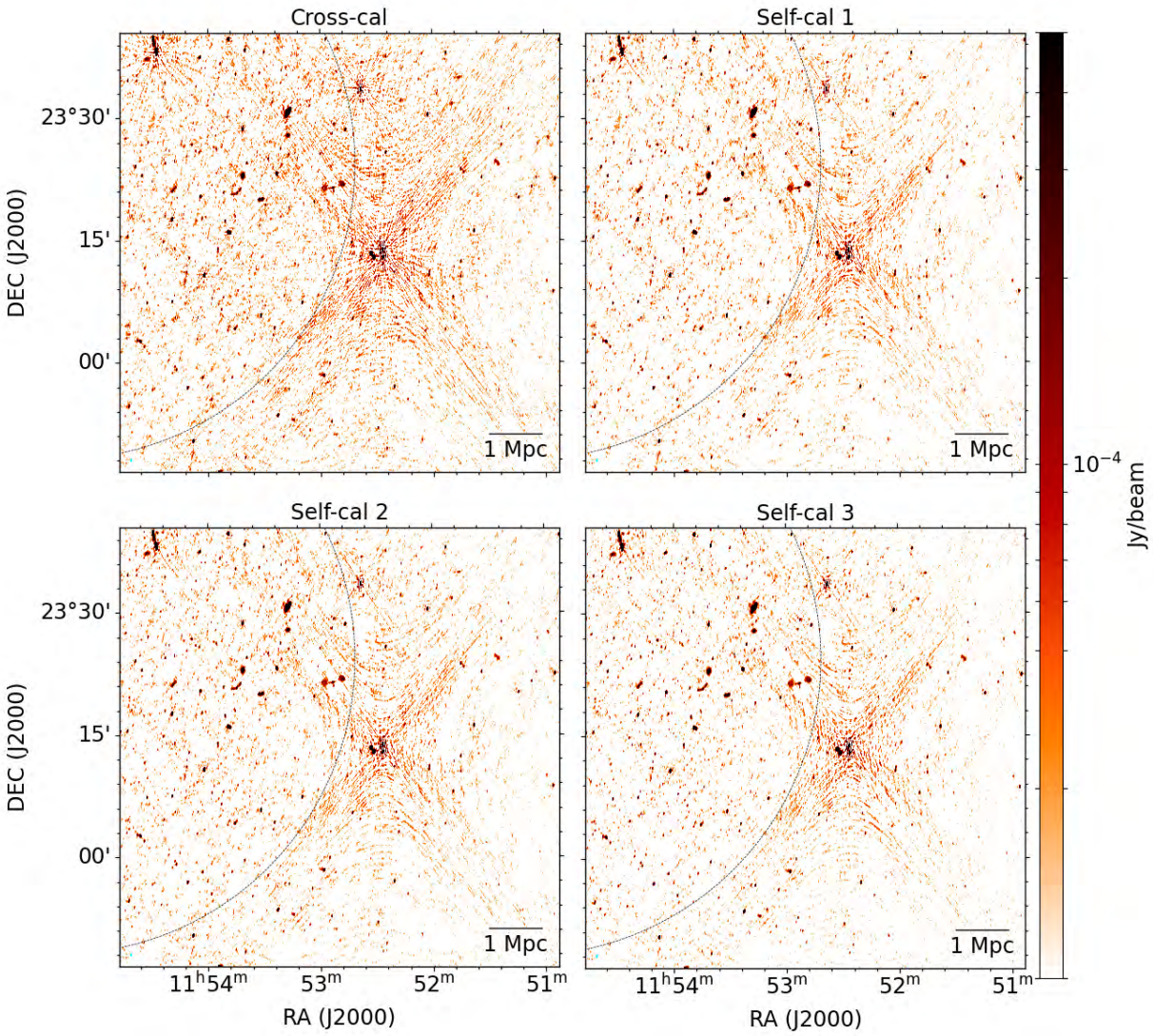


Figure 4.2: ACO 1413 2GC image artefacts. The panels show from *top left* to *bottom right* the progression of the 2GC imaging for a portion of the ACO 1413 field that highlights a major DDE artefact. The black dashed line shows the MeerKAT primary beam. The beam size in each panel is (13.5″, 6.1″, 171.4°). The global apparent rms noise from Cross-cal to Self-cal 3 is: 15.0, 11.7, 10.5, 7.9 $\mu$Jy/beam, respectively.

entire bandwidth. At the same time, the visibilities were flagged per baseline and correlation using a (median absolute residual) MAD filter with default thresholds. Figure 4.2 shows the progression of the ACO 1413 field during 2GC imaging. The global image noise (calculated as the root mean square, rms, of the entire residual image) steadily improved. However, the reduction in severe artefacts seen from the second to third rounds was limited, suggesting that DDEs cause these

artefacts. Similar results were found for all other clusters. Hence, 2GC was stopped at this point, and I ended our use of CARACal.

### 4.2.2 3GC: killMS + DDFacet

After 2GC, I used the calibration and imaging software of killMS[15] (kMS, Tasse, 2014a,b) and DDFacet[16] (DDF, Tasse et al., 2018) mentioned in Section 3.3.3 for 3GC; the process of using the modelled DI target data to correct for the DD terms of the RIME. In the context of MeerKAT, its large FoV and bandwidth cause direction-dependent effects to be significant contaminants of the astrophysical signal. The main effects are primary beam rotation and antenna pointing errors. These manifest as radial artefacts around bright sources located near the primary beam sidelobes and worsen with the strength of the affected source – a few 10s of sources can present such artefacts in a single field, and a clear example is highlighted in Figure 4.2. It is possible to consider each affected source individually using the differential gain calibration or 'source peeling' of CubiCal (Kenyon et al., 2018). However, to streamline the calibration process, I choose to instead calibrate over the entire FoV via the facet-based calibration and imaging of killMS and DDFacet. Tasse et al. (2018) showed that these two software work well in partnership to produce various types of 3GC images. The deconvolution algorithms of DDF and WSClean are very different, so although the same data is imaged, the two software give 2GC images with slightly different beam shapes and noise profiles. However, the overall image quality is comparable, and for the sake of a like-to-like comparison, I re-image the 2GC data with DDFacet and proceed with 3GC.

Asad et al. (2021) modelled the MeerKAT L-band primary beam attenuation using astro-holography (AH). AH is a technique in which a well-known target is observed with a subset of stationary antennas, while another subset drifts over the field to capture the voltage response of each antenna to that source. I make use of their models via the `eidos`[17] package, which generates the telescope's primary beam intensity, shape and spectral behaviour as image cubes out to a dis-

[15] `https://github.com/saopicc/killMS`
[16] `https://github.com/saopicc/DDFacet`
[17] `https://github.com/ratt-ru/eidos`

tance of three sidelobes on the sky (∼10°), where the third axis steps in frequency. These models can be used by kMS+DDF to correct for the primary beam attenuation and rotation. I imaged a $6° \times 6°$ square with 256 pixels and steps of 10 MHz in frequency.

killMS requires the user to supply a tessellation of the FoV to define the directions in which the DD terms are solved. The `MakeModel.py`[18] script of the DDFacet repository is used to make this tessellation file. The script can take a ds9 regions file and generate an optimised tessellation pattern around the locations specified, where the total flux of the field is divided equally between the tiles. The optimal number of tiles (or, equivalently, sources or directions) depends on the specific data. Through trial and error, in each cluster case, I experimented with the number of directions to use and found that 4-6 directions per field gave good improvements in the global rms and the level of severe artefacts. Hence, 4-6 bright problematic sources (clearly responsible for extended DDE-style radial artefacts) in each field were parsed to the script to each be the centre of a tessellation tile. Figure 4.3 shows the tessellation pattern used for ACO 1413, overlaid on its DDFacet 2GC restored image. During the derivation of the solutions, I used the KAFCA solver to make both amplitude and phase corrections within five-minute time and ten-channel frequency intervals while all other parameters were set to mirror that of DDF. The exact parameter values used are listed in Table A.3.

DDF offers a deconvolution algorithm called subspace deconvolution, SSD, which jointly and independently deconvolves distant sub-spaces/islands of pixels (defined using a mask) very efficiently, making it excellent for studying extended emissions in large images. I use the SSD2 deconvolver throughout the 3GC imaging process, which adds to the original functionality to choose the order of the fitted spectral polynomial and some other lesser deconvolution parameters. To produce images with the highest DR possible, I split the imaging into an auto-masked initial deconvolution from which a robust external mask was generated and then applied this mask in a direct continuation of the deconvolution. This way, as much of the 'real' emission as possible was deconvolved and imaged while the artefacts were cleaned out. The continuation of a previous de-

[18] `https://github.com/saopicc/DDFacet/tree/master/SkyModel`

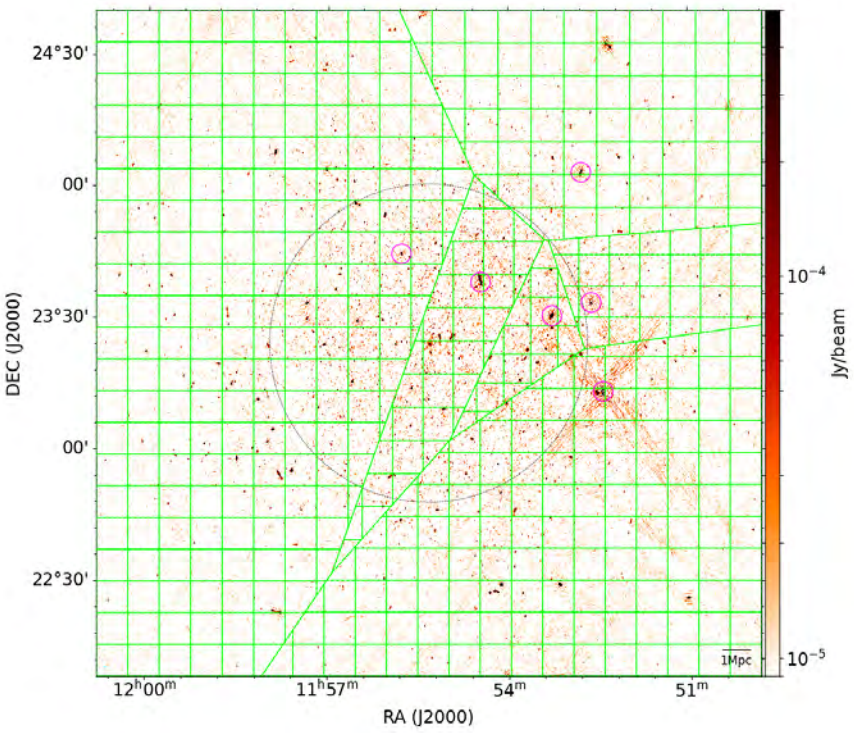


Figure 4.3: ACO 1413 tessellation pattern. The ACO 1413 DDFacet 2GC image is shown with the tessellation+facet pattern overlaid in green. The magenta circles show the sources given to the `MakeModel.py` script to tesselate the field; the irregular polygons show these tessellation tiles. A 20x20 grid of square facets were superimposed for primary beam correction. The black dashed circle shows the MeerKAT primary beam at 1.28 GHz.

convolution is easily performed in DDF when the `Predict--InitDicoModel` parameter is used. Each initial deconvolution ran for two major cycles and all emission above $5\sigma$ (five times the internally derived dirty image noise) was auto-masked. Each subsequent deconvolution ran for a single major cycle. The minor cycle stopping threshold was set to the maximum between three times the residual rms or one-hundredth of the peak residual found at the start of a major cycle. The SSD minor cycle algorithm is genetic in nature and targets the minimum absolute value of the residual in each sub-space and so converges very quickly. After each deconvolution, an updated mask was generated with the `breizorro` tool[19] using the tightest possible threshold (visually inspected to ensure only real sources were masked) and applied in the next step. This tool estimates a local (not

[19] `https://github.com/ratt-ru/breizorro`

global) image noise so that a deeper mask can be achieved on smaller scales. The external masks had thresholds of 6-8$\sigma$ (where $\sigma$ is the local image noise mentioned above), depending on the field, which was made slightly tighter after the 3GC solutions were applied due to the reduction in artefacts. All images were produced with the same size and scale as 2GC; now using 10 sub-bands for MFS, `Robust 0` weighting, fitting a 4th-order spectral polynomial, superimposing a 20x20 square facet grid onto the tessellation pattern, using the `eidos` primary beam models and re-evaluating the beam correction every five minutes in each facet to produce both apparent and intrinsic images throughout the process. The exact parameter values used are listed in Tables A.4,A.5. The resulting images had a roughly $\sim 8''$ resolution.

The basic procedure is summarised as follows:

1. *Tessellate the field,*
2. *Initial deconvolution,*
3. *Deeper deconvolution,*
4. *Derive kMS solutions,*
5. *Apply kMS solutions in deconvolution, and*
6. *Final deconvolution*

## 4.3 Improvements after 3GC

Figures 4.4-4.7 show comparisons between the DDF 2GC and 3GC FoVs for each of the remaining observations, focusing on the large-scale image artefacts. Table 4.4 gives a few simple qualitative statistics for the images. It is evident that the global image noise improved after 3GC for all standard-resolution images. Hence, the dynamic range quantities, $DR^{(1)}$ and $DR^{(2)}$ (defined as the maximum pixel value divided by the global image noise and the absolute value of its minimum pixel, respectively) of these images improved as well. The 3GC improved the global noise by an average of 7% without significantly affecting the maxima values; hence, the $DR^{(1)}$ values also

Table 4.4: 2GC vs 3GC image statistics. Taken from Trehaeven et al. (2022). Columns: cluster name, image type (all at `Robust 0`), global root mean square, and global dynamic ranges calculated with respect to the root mean square and minimum pixel values of the unsubtracted images.

| Cluster | RMS ($\mu$Jy/beam) | | DR$^{(1)}$ (max/rms) | | DR$^{(2)}$ $\|\|max/min\|\|$ | |
|---|---|---|---|---|---|---|
| | 2GC | 3GC | 2GC | 3GC | 2GC | 3GC |
| ACO 1413 | 8.3 | 7.4 | 10024 | 11284 | 87 | 354 |
| ACO 3444 | 6.4 | 5.9 | 26828 | 29017 | 110 | 319 |
| MACS J1115.8+0129 | 8.2 | 7.6 | 4902 | 5224 | 92 | 265 |
| MACS J2140.2-2339 | 7.2 | 7.1 | 12208 | 12394 | 198 | 386 |

improved by 7%. The $DR^{(2)}$ values improved by just under a factor of three, meaning that the kMS solutions significantly constrained the deep negative PSF sidelobes of the strongest sources in the fields. I note that the 2GC image of MACS J2140.2-2339 was largely absent of any artefacts, so 3GC was not expected to improve this field significantly.

Below I describe the improvements in each field except for ACO 1795. I used the SIMBAD[20] catalogue to identify individual sources of interest unless otherwise stated – and this holds for the remainder of this thesis. To determine individual source flux densities, I used CASA `imstat` after calculating a local rms noise value from a cutout of the corresponding residual image and parsing a region file describing the source isocontour that was three times this value.

### 4.3.1 ACO 1413

A comparison between the ACO 1413 2GC and 3GC FoV is shown in Figure 4.4. A significant snowflake-like artefact is in the 2GC image, spanning ∼0.5°. It is centred around a bright double radio source located just outside the primary beam, ∼40′ from the phase centre, at (RA, DEC) = (11:52:26.5, +23:13:47.3) and (11:52:26.2, 23:12:54.6), designated as NVSS J115226+231347 and NVSS J115226+231255, with respective flux densities measured consistently across the final 2GC and 3GC intrinsic images to be ∼260 mJy and ∼175 mJy. The 3GC dramatically reduced the intensity of these artefacts, with much of the spikes going down to noise level, and improved the global rms noise by 11% from 8.3 $\mu$Jy/beam to 7.4 $\mu$Jy/beam. The insets show a zoom of an FR-II

[20] `http://simbad.cds.unistra.fr/simbad/`

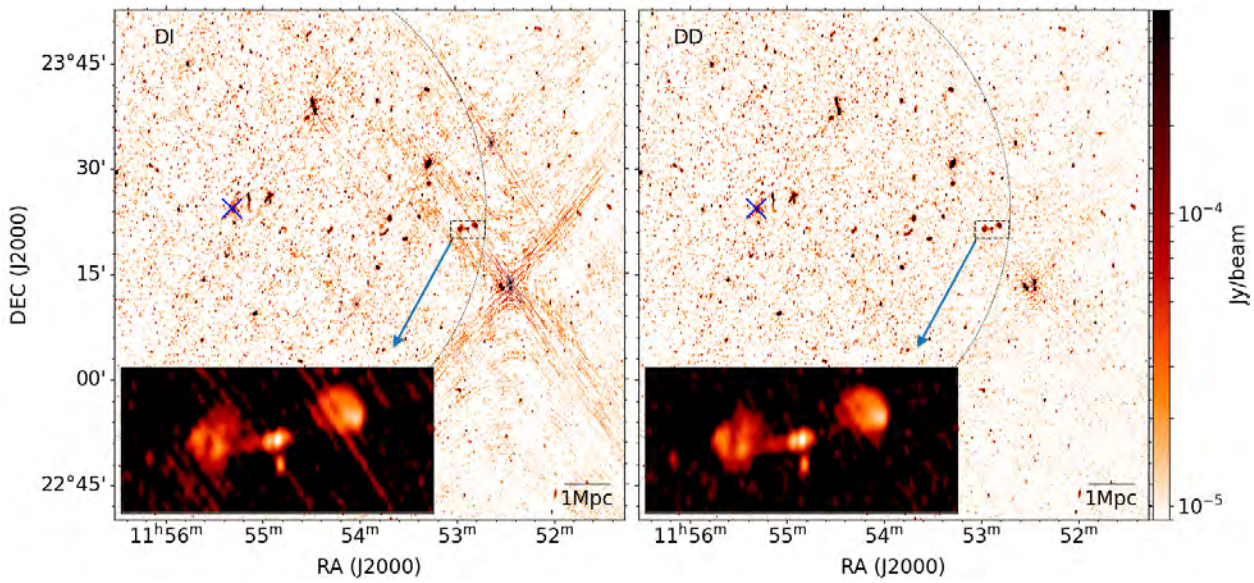


Figure 4.4: ACO 1413 2GC vs 3GC artefacts. *Left:* 2GC image, beam size (12.3″, 5.9″, -4.6°), global rms noise 8.3 $\mu$Jy/beam. *Right:* 3GC image, beam (12.2″, 5.9″, -4.5°), global rms noise 7.4 $\mu$Jy/beam. A blue cross marks the phase centre of the images. The thin dashed black arc indicates the primary beam of the telescope. The bold dashed black rectangle marks an FR-II galaxy contaminated by an artefact with an arrow pointing to a zoomed inset of this source displayed in the inverse colour bar. The local rms of this source decreased by just under a factor of 2 in the 2GC to 3GC images. Taken from Trehaeven et al. (accepted).

radio source affected by the artefacts. The 2GC inset displays a snowflake spike piercing the radio lobes and nucleus; however, they have disappeared in the 3GC inset, clearly depicting the source morphology and showing how valuable 3GC can be to a potential source of interest. The local rms near this source improve by just under a factor of two from 22.3 $\mu$Jy/beam to 12.0 $\mu$Jy/beam.

### 4.3.2 ACO 3444

A comparison between the ACO 3444 2GC and 3GC FoVs is shown in Figure 4.5. A set of three bright point-like sources located ~30′ from the phase centre (just inside the primary beam) cause significant concentric artefacts that extend to ~10′ in radius. The set of sources is positioned, from left to right as seen in Figure 4.5, at (10:22:29.4, -26:47:34.5), (10:23:27.1, -26:50:09.7), (10:24:07.4, -26:44:17.5), and are designated as WISEA J102407.38-264417.8 (NASA/IPAC Extragalactic Database, NED[21]), NVSS J102327-265009 and NVSS J102229-264734, respectively.

[21] `https://ned.ipac.caltech.edu/`

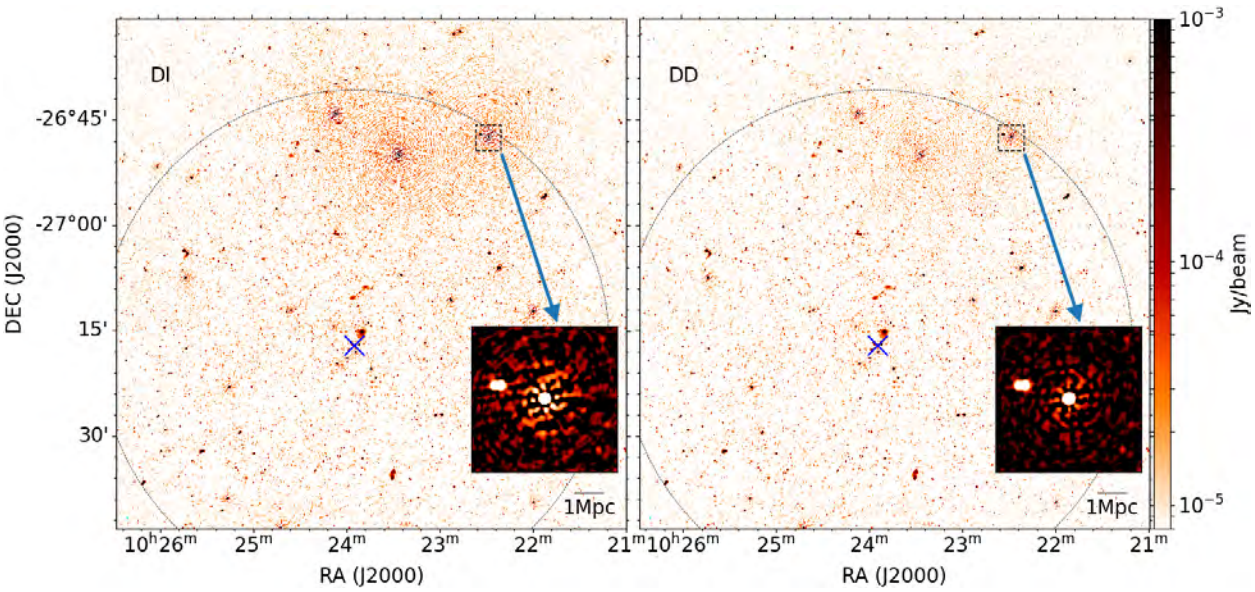


Figure 4.5: ACO 3444 2GC vs 3GC artefacts. *Left:* 2GC image, beam size (7.4″, 6.0″, -10.3°), global rms noise 6.4 $\mu$Jy/beam. *Right:* 3GC image, beam (6.8″, 5.9″, -16.0°), global rms noise 5.9 $\mu$Jy/beam. A blue cross marks the phase centre of the images. The thin dashed black arc indicates the primary beam of the telescope. The bold dashed black rectangle marks a bright point source with an arrow pointing to a zoomed inset of this source displayed in the inverse colour bar. The local rms decreased by just over a factor of two. Taken from Trehaeven et al. (accepted).

They have a maximum flux density of ~270 mJy. The kMS gain solutions reduced the PSF side-lobes and further propagating effects such that now much of the artefacts are almost at the background noise level. The 3GC improved the global noise rms by 8% from 6.4 $\mu$Jy/beam to 5.9 $\mu$Jy/beam. The insets show a zoom of the last contaminating source mentioned above. Its local rms improved by just over a factor of two from ~52 $\mu$Jy/beam to ~24 $\mu$Jy/beam.

### 4.3.3 MACS J1115.8+0129

Figure 4.6 shows a comparison between the 2GC and 3GC FoVs for this cluster. The image artefacts are less severe than in the previous two cases; nevertheless, some minor artefacts are present around several sources inside the primary beam, such as GB6 B1114+0136 located ~22′ south-east of the phase centre, highlighted by the insets. The comparison shows the extending artefacts reduced after 3GC such that its local rms value improves by just under a factor of two, from 21.7 $\mu$Jy/beam to 12.6 $\mu$Jy/beam. Similar minor improvements are seen throughout the FoV

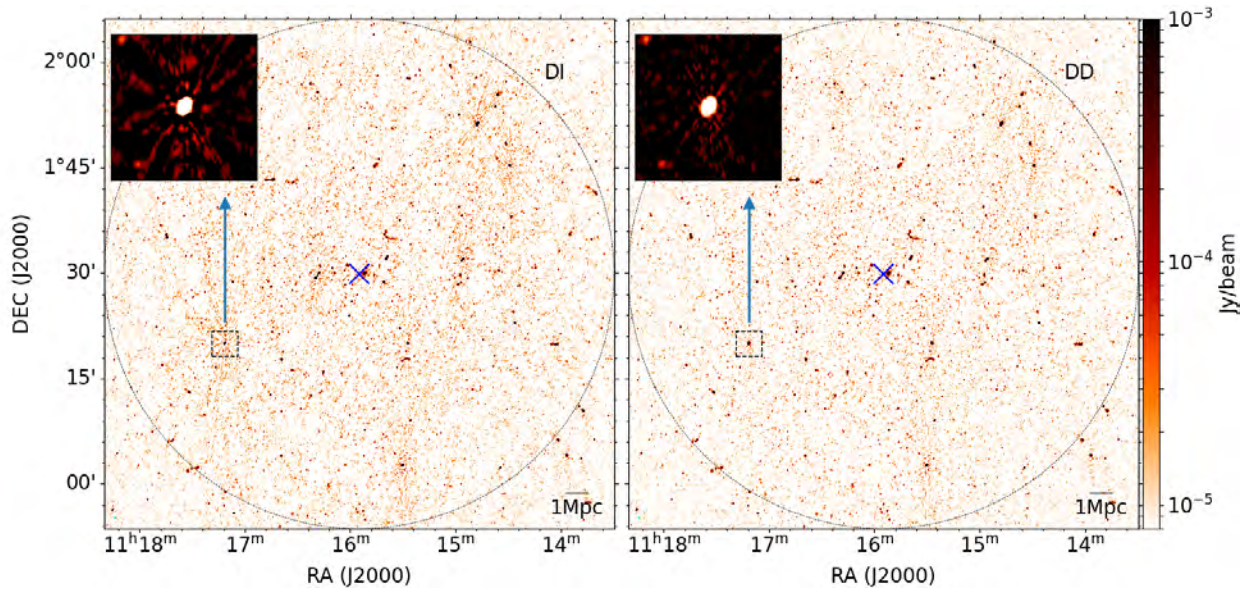


Figure 4.6: MACS J1115.8+0129 2GC vs 3GC artefacts. *Left:* 2GC image, beam size (8.6″, 6.6″, -16.7°), global rms noise 8.2 $\mu$Jy/beam. *Right:* 3GC image, beam (8.5″, 6.5″, -16.2°), global rms noise 7.6 $\mu$Jy/beam. A blue cross marks the phase centre of the images. The thin dashed black arc indicates the primary beam of the telescope. The bold dashed black rectangle marks a bright point source with an arrow pointing to a zoomed inset of this source displayed in the inverse colour bar. The local rms decreased by just under a factor of two. Taken from Trehaeven et al. (accepted).

and add to reduce the global noise level by 7% from 8.2 $\mu$Jy/beam to 7.6 $\mu$Jy/beam.

### 4.3.4 MACS J2140.2-2339

A comparison between the 2GC and 3GC images is shown in Figure 4.7. The 2GC field is largely clear of any significant artefacts, so 3GC was not expected to improve the imaging results by any significant amount. The only source responsible for any artefacts of note is highlighted by the inset, identified as PMN J2142-2329 from the NED catalogue. Its local rms improved by a factor of 1.75, from 32.9 $\mu$Jy/beam to 18.8 $\mu$Jy/beam, but otherwise, 3GC did not significantly improve upon the 2GC image.

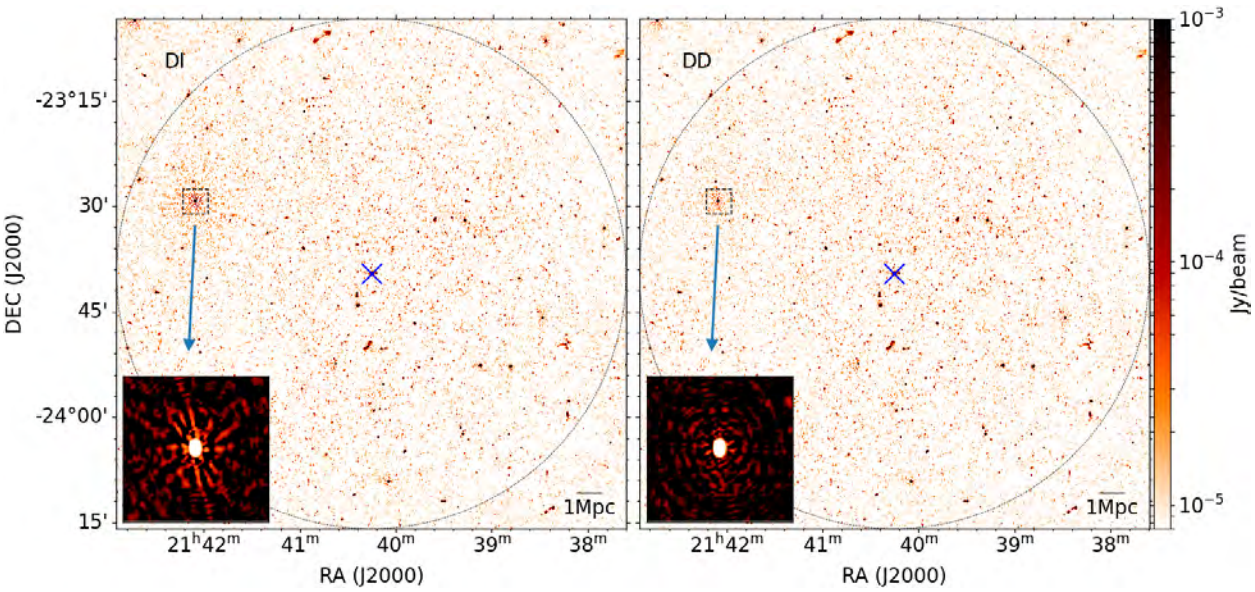


Figure 4.7: MACS J2140.2-2339 2GC vs 3GC artefacts. *Left:* 2GC image, beam size (7.9″, 6.3″, -9.7°), global rms noise 7.2 $\mu$Jy/beam. *Right:* 3GC image, beam (7.8″, 6.2″, -8.6°), global rms noise 7.1 $\mu$Jy/beam. A blue cross marks the phase centre of the images. The thin dashed black arc indicates the primary beam of the telescope. The bold dashed black rectangle marks a bright point source with an arrow pointing to a zoomed inset of this source displayed in the inverse colour bar. The local rms decreased by just under a factor of two. Taken from Trehaeven et al. (accepted).

## 4.4 ACO 1795

ACO 1795 was an exceptional case in our sample. Unfortunately, strong artefacts centred around its BCG limited the local image quality and prevented us from detecting any nearby diffuse emission. The calibration was expected to be difficult because the only calibrator source observed, 3C286, is not a recommended MeerKAT primary calibrator. This source is highly polarised and without a well-characterised MeerKAT local sky model. Nevertheless, I describe the calibration of this target and show that the corrupting artefacts are not direction-dependent in nature.

It is known that this BCG is quite strong, Giacintucci et al. (2014a) measured a flux density of $S_{1.4\,\mathrm{GHz}}$ = 917 ± 46 mJy from its FIRST (Becker et al., 1995) image, and I measure a similar value of $S_{1.28\,\mathrm{GHz}}$ = 975 ± 97.5 mJy from our best 2GC image shown in the top right panel of Figure 4.8. The cluster's high northern declination (+26°) relative to the MeerKAT's southern declination (−31°) results in a very asymmetric *uv*-sampling distribution and PSF, which may have

caused the strong BCG sidelobes to be indistinguishable from real emission during deconvolution. Interestingly, ACO 1413 and ACO 1795 lie at a similar declination PSF[22], but the images of the former do contribute to our science case. The difference is likely due to second-order leakage effects in the ACO 1795 field caused by its strong BCG (and its central location on top of any possible diffuse emission), which is approximately three times brighter than the brightest source in the ACO 1413 field.

After the standard CARACal processing described in Section 4.2.1, I tried to improve the calibration by solving for different solution types during 2GC in CARACal, listed in Table A.1. I performed two rounds of delay self-calibration (Fslope) and a final round determining the real and imaginary components of the gain amplitude and phase (Gain2x2); the former refines the delay solutions derived from 1GC and the latter refined the gains and is typically used when second-order leakage is expected. However, a significant improvement over the usual phase-only self-calibration could not be found. I then tried CubiCal's successor, QuartiCal[23], designed to make the chaining of Jones terms in a single self-calibration round very accessible and efficient. This means that QuartiCal can solve for one Jones term, apply it and then solve for another term and so on without having to image the corrected data in between, thus deriving more accurate calibration solutions. QuartiCal had not been officially released then, so much experimentation was had. In each round of self-calibration, I solved for a single delay solution over the entire bandwidth, applied it and solved for complex-gain solutions per channel, applied these and repeated. Hence, QuartiCal could calculate solutions in a single self-calibration round that would be analogous to the entire three rounds of CubiCal solutions. I performed three rounds of such self-calibration, solving for a complex gain (per channel) over the entire time axis in the first round, then for 30 equal time intervals in the second, and finally, 60 equal time intervals in the last round. The exact QuartiCal parameters used are listed in Table A.2. I imaged with WSClean, with similar parameters to the standard 2GC procedure used for the other clusters. However, I split the imaging similar to 3GC to deconvolve as deeply as possible, i.e. an auto-masked initial deconvolution and a manually

[22] ACO 1413 at +23° is among the most northern sources published with MeerKAT data
[23] `https://github.com/ratt-ru/QuartiCal`

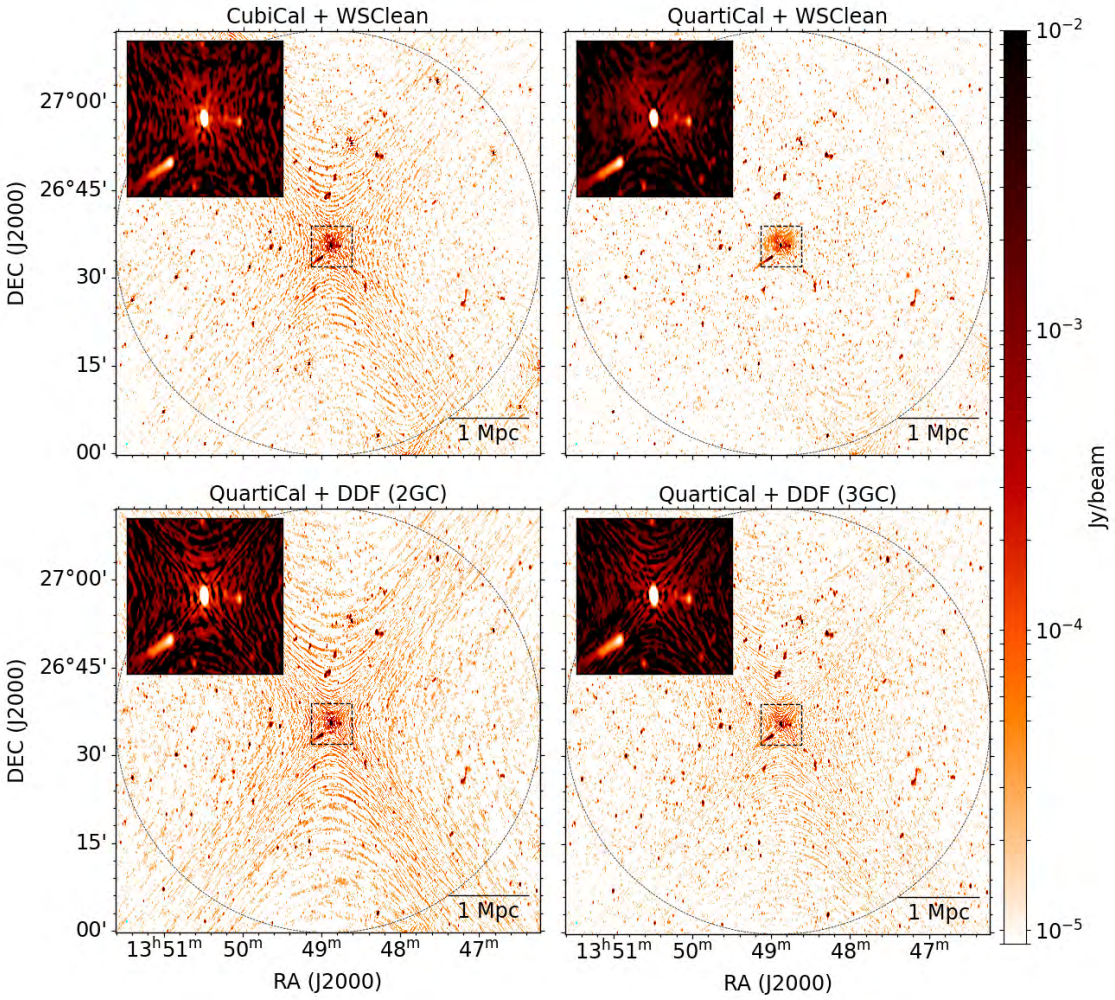


Figure 4.8: ACO 1795 best images. Each panel shows the best image for each combination of calibrator software and imager I tried. The black dashed circle shows the MeerKAT primary beam. The black dashed square indicates the central 500 kpc box shown in the insets. All images are on the same colour scale and convolved to a (15″, 7″, 0°) beam. The global rms noise from *top left* to *bottom right* is: 8.2, 6.7, 11.2, 8.7 $\mu$Jy/beam, respectively. The local rms noise in each inset from top left to bottom right is: 78.5, 34.9, 91.0, 58.5 $\mu$Jy/beam, respectively.

masked direct continuation. Some significant improvements over the CubiCal counterparts were found; however, residual sidelobe modelling errors remained so that any nearby diffuse emission was still fatally obscured by the artefacts. Thereafter, I performed the same 3GC procedure on the QuartiCal-derived visibilities as for the rest of the observations.

Figure 4.8 shows the best images I could produce for each of WSClean and DDFacet, with a global and local rms noise for each mentioned in the caption; all images are convolved to the

Table 4.5: ACO 1795 Image statistics. Columns: Image, local noise inside a 500 kpc box centred on the BCG, global noise, and global dynamic ranges calculated with respect to the root mean square and minimum pixel values, respectively.

| Image | Local rms ($\mu$Jy/beam) | Global rms ($\mu$Jy/beam) | Global DR$^{(1)}$ (max/rms) | Global DR$^{(2)}$ $\|\|max/min\|\|$ |
|---|---|---|---|---|
| CubiCal + WSClean | 78.5 | 8.2 | 95387 | 471 |
| QuartiCal + WSClean | 34.9 | 6.7 | 114933 | 1295 |
| QuartiCal + DDF (2GC) | 91.0 | 11.2 | 61098 | 615 |
| QuartiCal + DDF (3GC) | 58.5 | 8.7 | 91087 | 1173 |

same resolution for ease of comparison. Panels a) and b) are imaged with WSClean, while c) and d) are imaged with DDF (all panels had the same cross-cal procedure, as described in Section 4.2.1). Panel a) shows the final image after self-calibrating using CubiCal with two rounds of delay solutions and a final round of complex-gain solutions, and similar masking and solution intervals as described in Section 4.2.1. Panel b) is the final image after using QuartiCal, as explained above. Panel c) shows panel b) imaged with DDF until just before kMS solutions were derived (Step 3 of Section 4.2.2). Then, panel d) shows panel c) after the 3GC procedure described in Section 4.2.2. These images cannot produce valid scientific results at the cluster core because of the residual artefacts. However, I can compare them to each other. From panel b), I can see that the QuartiCal solutions provided a more physically accurate sky reconstruction than CubiCal when imaged with WSClean. The QuartiCal solutions eliminated much of the extended artefacts and resulted in the best image statistics, as seen in Table 4.5. This table lists, for each image, a local and global rms noise for a box of size 500 kpc centred on the BCG and the entire FoV, respectively, and the global $DR^{(1)}$ and $DR^{(2)}$ values. However, imaging the QuartiCal-derived data set with DDFacet and its SSD2 deconvolver at 2GC produced the worst image. After 3GC solutions were applied, the DDFacet image improved but not beyond that of the WSClean image.

Concluding our calibration analysis of ACO 1795, since 3GC could not significantly improve upon the severe artefacts centred around the BCG, this suggests that these artefacts are not direction-dependent in nature; reaffirming that second-order leakage effects may indeed be causing them. The calibration of this source may have improved if a proper primary calibrator had been

observed. Further investigation is required to determine if synergy between MeerKAT/SKA-Mid and LOFAR is possible for this cluster. This section presents a case that a detailed comparison between the calibration and imaging results of CubiCal vs QuartiCal and WSClean vs DDFacet would be fascinating; however, this is beyond the scope of this work, and I leave ACO 1795 out of all further work in this thesis.

## 4.5 Flux suppression

As mentioned in Section 3.3.3, 3GC is known to cause flux suppression/absorption. To evaluate the extent to which our 3GC solutions caused any flux suppression/absorption, I need to generate a catalogue of the 2GC and 3GC field sources and compare how closely the flux densities match. To accurately compare the sources, the images need to be at the same resolution. From Figures 4.4-4.7, I see that the 2GC and 3GC beam sizes are very similar; however, to ensure a like-to-like comparison, I first convolved each 3GC image to the beam size of the corresponding 2GC image. Thereafter, I ran the PyBDSF[24] source-finder with default settings on these images and spatially cross-matched these catalogues using the TOPCAT[25] application such that only sources with a positional offset of at most the image resolution are selected. I then de-selected the sources whose 2GC flux density was less than one mJy (the approximate threshold at which PyBDSF can reliably detect real sources). I overlaid the reduced catalogues onto the respective images to visually inspect and ensure that no artefacts were accidentally catalogued. I plotted the flux densities of the remaining sources and performed a linear least squares regression in log-log space using the Bivariate Correlated Errors and Intrinsic Scatter (BCES) Python package[26]. I used this package because it incorporates into the fitting the associated measurement uncertainties of both variables and the intrinsic scatter of the data. Additionally, performing the fit in log-log space allowed an

[24]https://github.com/lofar-astron/PyBDSF
[25]http://www.star.bris.ac.uk/ mbt/topcat/
[26]https://github.com/rsnemmen/BCES

accurate representation of the spread in the source intensities. I present the fit in the form

$$\log_{10}(y) = (A \pm \Delta A)\log_{10}(x) + (B \pm \Delta B), \tag{4.1}$$

where $x$ and $y$ represent the 2GC and 3GC source flux densities, respectively. However, measurement uncertainties do not directly transform into log-log space, but by error propagation, follow the relation:

$$\log_{10}(\Delta a) = 0.434\frac{\Delta a}{a}, \tag{4.2}$$

where $a$ is the measurement and $\Delta a$ is the associated uncertainty. The line-of-best-fit that minimises the orthogonal distances of the measurement uncertainties is

$$\log_{10}(y) = (1.08 \pm 0.02)\log_{10}(x) + (-0.20 \pm 0.05), \tag{4.3}$$

and is shown in the left panel of Figure 4.9. Since the slope A 1, some flux suppression/absorption occurred during the 3GC procedure, with an average difference of 8%. Most of this difference is attributed to the extreme suppression experienced by a handful of sources in the ACO 3444 and ACO 1413 fields; further investigation into what causes these outliers is needed. However, this did not affect our science case as the flux measurements given in Chapter 5 are consistent across 2GC and 3GC.

## 4.6 Fluxscale uncertainty

All scientific measurements should have a corresponding uncertainty associated with them. Since the intrinsic mini-halo signals are corrupted along their journey to the instrument correlators, as described in Section 2.1.1, I performed multiple calibration steps to limit the effect of erroneous data. However, the calibration cannot be perfect, and one astronomer's calibration procedure can yield slightly different measurements than another's. This, and the cumulative total of all other systematic errors, are quantified by the calibration's associated fluxscale uncertainty. To determine

an accurate calibration fluxscale uncertainty, I compare our 3GC flux densities to a fiducial data set and take the mean difference as the fluxscale uncertainty. I chose to compare our data against the NRAO VLA Sky Survey (NVSS) (Condon et al., 1998) data as these are commonly used to perform such a comparison in L-band. For each field, I convolved the intrinsic 3GC image to the same 45″ beam size as NVSS and then ran PyBDSF with default settings to generate a catalogue of sources. I spatially cross-matched (within 45″) these catalogues with the NVSS catalogue using Topcat and then selected only the sources within the MeerKAT primary beam that were approximate point sources. I determined whether a source was approximately a point source by calculating, for both the NVSS and MeerKAT catalogues, the ratio of its flux density (unit: Jy) to peak surface brightness (unit: Jy/beam, resulting in a value representing the number of beams within the source region) and selecting only those sources within a ±5% range of unity. After that, utilising the power-law dependency of flux density on frequency, I then scaled the MeerKAT 1.28 GHz flux densities of the remaining sources to 1.4 GHz using the relation:

$$S_{1.4\mathrm{GHz}} = S_{1.28\,\mathrm{GHz}} \left( \frac{1.4\,\mathrm{GHz}}{1.28\,\mathrm{GHz}} \right)^{\alpha}, \tag{4.4}$$

with $\alpha = -0.7$, the typical spectral index of a point source (e.g., Becker et al., 1995). I calculated the mean percentage difference between the MeerKAT and NVSS measurements and adopted this value as our fluxscale uncertainty. I find an average difference of 10%. The line-of-best-fit is shown in the right panel of Figure 4.9 and is very close to being one-to-one, with equation

$$\log_{10}(y) = (1.01 \pm 0.01) \log_{10}(x) + (0.00 \pm 0.02), \tag{4.5}$$

where $x$ and $y$ are the NVSS and MeerKAT flux densities, respectively. Since the flux densities are distributed around a slope and y-intercept of almost exactly one and zero, respectively, our calibration resulted in flux densities that are, on average, neither systematically higher nor lower than those of NVSS.

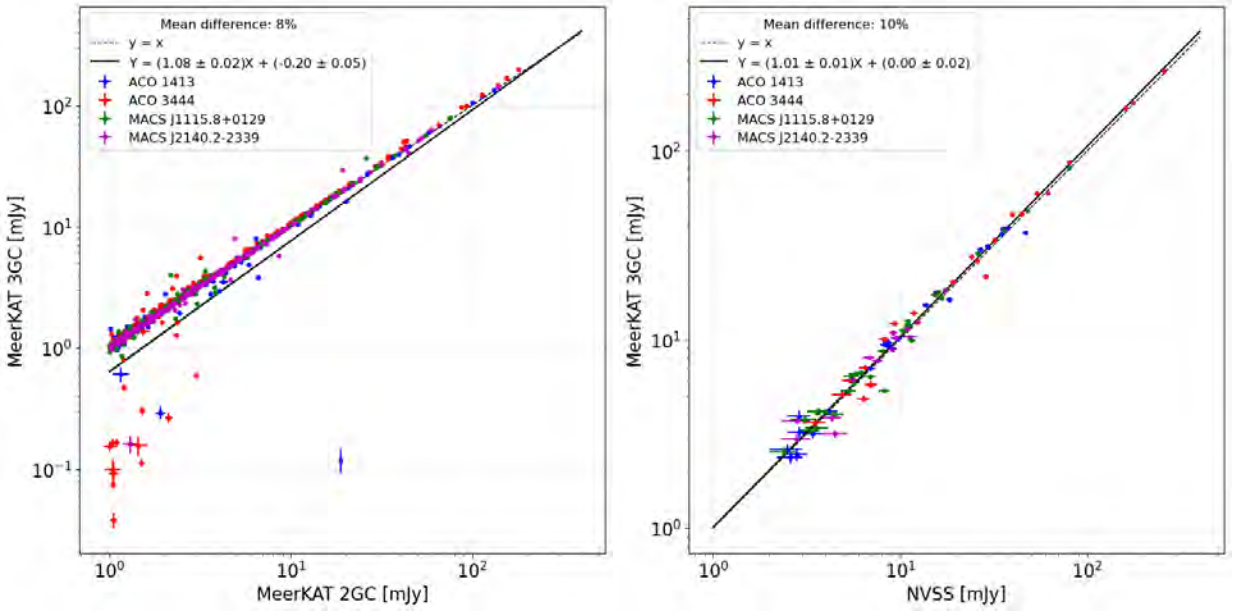


Figure 4.9: PyBDSF source flux densities. The line-of-best-fit is stated in the legend of each plot. The fits are in the same form as equation 4.1, but with $Y = \log_{10}(y)$ and $X = \log_{10}(x)$. The $2\sigma$ confidence intervals on the fits are obscured by the fitted lines. *Left:* MeerKAT 2GC vs 3GC. Anomalous flux suppression is indicated by the points that lie well below the line $y = x$. *Right:* NVSS vs MeerKAT 3GC. The mean difference between the $x$ and $y$ data points is 10%, which I take to be the fluxscale uncertainty.

## 4.7 Source subtraction

Here I describe the practical application of the source subtraction introduced in Section 3.4. I chose to perform the subtraction in the visibility plane, which requires the direct manipulation of the MS data. This is quickly done using Stimela [27] (Makhathini, 2018); a Python-based containerised scripting framework that offers access to radio interferometric imaging, calibration and data processing and analysis packages in the form of Python modules. Stimela offers a module called `msutils` that can perform arithmetic directly on the columns of an MS. I use this module and the kMS solutions derived in Step 4 of the Section 4.2.2 to generate both 2GC and 3GC source subtracted (SRC-SUB) images.

All imaging, deconvolution and masking parameters and rules mentioned in Section 4.2.2 were followed for the subtraction procedure except where otherwise stated. To generate the 3GC

[27] https://github.com/ratt-ru/Stimela

subtraction model, I applied derived kMS solutions and imaged the visibilities at a high-resolution (HR) using 'uniform' weighting (`Robust -2`). DDFacet can save the predicted model data of any imaging run into its own column, so I saved the HR point source model into `HR_MODEL_DATA`. Hence, the subtraction effectively amounts to the column-wise operation:

$$\texttt{CORRECTED\_DATA--HR\_MODEL\_DATA = DIFFUSE\_EMISSION.} \tag{4.6}$$

Additionally, during HR imaging, I applied a *uv*-cut to ensure that only the compact emission from the field was imaged and modelled. DDFacet offers the parameter `--Selection-UVRangeKm`, which takes as an argument in units of physical baseline length the minimum and maximum *uv* range to be considered. I set the maximum to be arbitrarily large and choose a physically motivated minimum *uv*-cut of 100 kpc at the cluster redshift, since this is the minimum size of a mini-halo as per the definition adopted from Giacintucci et al. (2017). Thus, for each cluster, utilising Rayleigh's criterion, I calculated the minimum of the *uv* range as

$$uv_{min}[km] = \frac{1.22 \times 180 \times 3600 \times c}{\pi \times \nu} \times \frac{scale}{100kpc}, \tag{4.7}$$

where c is the speed of light in km/s, $\nu$ is the MeerKAT central L-band observing frequency of $1283.79 \times 10^6$ Hz, and *scale* is the angular-to-linear scale quoted in Table 4.1. Applying this *uv* range ensures that any emission greater than 100 kpc in size is excluded in the high-resolution (HR) images, which had a final resolution of $\sim 4''$.

Much experimentation took place for the masking of the compact sources since only the masked emission would be included in the subtraction model. Again, I used `breizorro` to generate all external masks, and used a generic $4\sigma$ threshold for all clusters to mask the field sources in the HR images. A threshold any smaller than this resulted in significant image artefacts being masked, while a threshold any larger left much of the low surface brightness compact emission unmasked. I expect the under-subtraction of any emission not captured by the mask. To ensure that the mini-halo would not be affected by such emission, I manually added pixels to the mask

that corresponded to point-like sources near the mini-halo that were not picked up by the generic threshold. When needed, the Aladin Sky Atlas (Bonnarel et al., 2000; Boch & Fernique, 2014) was used to overlay various radio, infrared and optical catalogues onto the images to identify individual sources. I found that the HR model needed to be (re)-predicted after imaging, but without specifying a *uv*-cut to ensure that the short baselines that were cut are included in the prediction of the subtraction model – since I include these shorter baselines in the imaging the diffuse emission. Once this final model had been set and the subtraction performed, I imaged the resulting column at `Robust 0`, again giving ~8″ resolution images. I produced SRC-SUB images for both 2GC and 3GC images, with the only difference between the two being the application of the kMS solutions and the final masking thresholds, which were set to be the same as the final 2GC/3GC thresholds from Section 4.2.2.

The basic procedure is summarised below:

1. *Initial deconvolution at High-Resolution (HR),*
2. *HR mask,*
3. *Deeper deconvolution,*
4. *Predict HR model,*
5. *Subtract,*
6. *Initial deconvolution at standard resolution, and*
7. *Final deconvolution*

### 4.7.1 Evaluating the subtraction

Source subtraction and its effectiveness is difficult to quantify, and the DR values are meaningless after subtraction. The situation is even more complex when 3GC is involved. An example of the 2GC and 3GC HR and SRC-SUB images for ACO 1413 is shown in Figure 4.10 – note the higher noise in the HR images because of the uniform weighting. These images are centred on a source that was heavily over-subtracted, being one of the strongest sources in the field. It can be

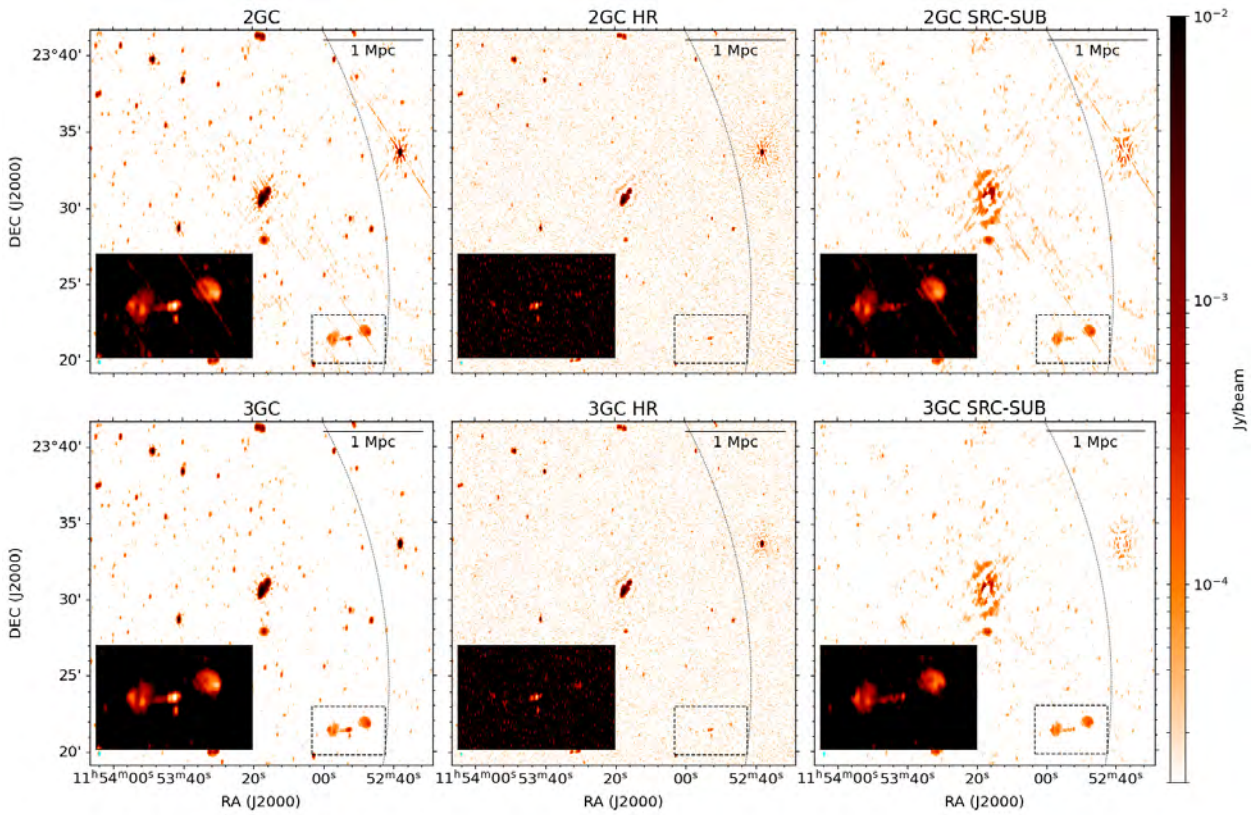


Figure 4.10: ACO 1413 2GC (*top*) vs 3GC (*bottom*) unsubtracted (*left*), HR (*middle*) and SRC-SUB (*right*) images. All images are centred on a source that was over-subtracted and as a result, experienced an amplification in artefacts and noise after subtraction. Beam sizes for the *left* and *right* images are the same as the left and right in Figure 4.4, respectively, and for the *middle* images is $(7.6'', 3.1'', -2.6°)$, and are displayed in the bottom left corner of each image. Local rms noise within the displayed cutouts from *top left* to *top right* is: 14.2, 23.4, 16.0 $\mu$Jy/beam. Local rms noise within the displayed cutouts from *bottom left* to *bottom right* is: 9.8, 22.6, 12.3 $\mu$Jy/beam. The insets show the same FR-II source as Figure 4.4. Green dashed contours show the -3$\sigma$ level in each image.

seen in the 2GC SRC-SUB image that the subtraction caused some additional artefacts and higher noise around this source. The 3GC solutions did not affect these artefacts; however, the improvements previously mentioned in Section 4.4 were conserved after source subtraction, as seen in the insets of each panel and the reduction in the amount of significantly negative regions after 3GC. Similar effects are seen in the other fields. Table 4.6 compares the global statistics of the 2GC and 3GC HR and point SRC-SUB images. I can see that, similar to the `Robust 0` counterparts, the HR images experienced a factor of two times improvement in $DR^{(2)}$ after 3GC, suggesting that the killMS solutions can improve the characterisation of the brightest source PSFs even when

Table 4.6: 2GC vs 3GC subtraction image statistics. Columns: cluster name, image type, global root mean square, and (only for HR images) global dynamic ranges calculated with respect to the root mean square and minimum pixel values.

| Cluster | Image | RMS ($\mu$Jy/beam) | | DR$^{(1)}$ (max/rms) | | DR$^{(2)}$ $\|\|max/min\|\|$ | |
|---|---|---|---|---|---|---|---|
| | | 2GC | 3GC | 2GC | 3GC | 2GC | 3GC |
| ACO 1413 | HR | 23.1 | 23.2 | 2896 | 2874 | 87 | 184 |
| | SRC-SUB | 8.5 | 7.9 | | | | |
| ACO 3444 | HR | 20.7 | 21.0 | 7233 | 7172 | 60 | 181 |
| | SRC-SUB | 6.8 | 6.1 | | | | |
| MACS J1115.8+0129 | HR | 27.4 | 27.5 | 924 | 924 | 28 | 35 |
| | SRC-SUB | 9.1 | 7.9 | | | | |
| MACS J2140.2-2339 | HR | 22.2 | 22.4 | 2558 | 2529 | 75 | 124 |
| | SRC-SUB | 7.3 | 7.1 | | | | |

imaged at a different resolution to what they were derived from. However, the global HR image noise remained comparable across 2GC and 3GC because the kMS solutions also caused a slight noise amplification in facets running along the first negative sidelobe of the primary beam. Further investigation into what causes this effect is needed.

Comparing Tables 4.4 and 4.6, we can see that the subtraction increased the global image noise values by 4% on average. However, with the 7% improvement due to the calibration, the 3GC SRC-SUB images are slightly deeper than the 2GC unsubtracted images. Since we performed source subtraction to remove the contaminating sources embedded within the radio mini-halos, comparisons for each mini-halo before and after point source subtraction are given in Chapter 6 as this is specific to our science case. In hindsight, perhaps the source subtraction could have been improved if I had only imaged a central region of the FoV. In this way, imaging would have taken much less time, and some of the artefacts closer to the primary beam sidelobes could have been avoided so that more detailed masking and modelling could have been performed.

## 4.8 Imaging considerations for an in-band spectral analysis

The spectral analysis of continuum data requires access to the sub-band images that make up the final MFS images. However, these sub-band images need a sufficient signal-to-noise ratio

(SNR) for science to be conducted directly on them. To this end, I re-imaged the 3GC unsubtracted and SRC-SUB data with three equal sub-bands, centred at 998.52, 1283.79 and 1569.05 MHz, and with a third-order spectral polynomial (effectively repeating Steps 5-7 of the 3GC and source subtraction procedures). To ensure all sub-bands are imaged in the same *uv* range and thus all sample the same spatial scales, I applied, in DDFacet, an inner and outer taper to each dataset of $\sim 5''$ and $\sim 14''$. The resulting sub-band images were convolved to a $15''$ circular beam. The ACO 1413 SRC-SUB images were exceptions to this and were convolved to $30''$ due to significant over-subtraction in the high-band. All other imaging parameters were the same between the unsubtracted and subtracted re-runs (the only difference being the column imaged). Then, to determine the in-band integrated spectra of the BCGs, I also similarly re-imaged the HR images (effectively repeating Steps 1-3 of the subtraction procedure) with an inner taper corresponding to the *uv*-cut and an outer taper $\sim 15''$ respectively. The resulting sub-band images were convolved to $7''$, except for ACO 1413, which has a poor spatial resolution due to its high northern declination and so needed to be convolved to $12''$.

# Chapter 5

# Radio Mini-Halo Results and Discussion

Here I present the results specific to our science case extracted from the data reduction presented in Chapter 4. This Chapter is based on the work presented in Sections 4 and 5 of Trehaeven et al. (2023). I use the high-fidelity images to calculate measurements that describe the physical mini-halo systems. I find a 10% fluxscale uncertainty for our calibration, which was fully discussed in Section 4.6. Below I describe the measurement-taking process for the parameters that physically describe the mini-halo (flux density, size, spectral index and radio power). The results are given in Table 5.1 and the images in Section **??**.

## 5.1 Flux density and size

The native-resolution (~8″) images show the detailed structure of the mini-halos. However, to characterise the overall structure and radiative strength, I convolved the 3GC SRC-SUB images to a 15″ circular beam shown in panel c) of Figures 5.2-5.5 and derive physical measurements from within the +3$\sigma$ contours of these smoothed images. I calculated the flux density by summing up all the pixel values (in units of Jy/beam) within these +3$\sigma$ contours and multiplying this by the number of restored beams contained within the contours (resulting in units of Jy). I verified our manual calculations by comparing them to the flux density calculated by CASA's `imstat` for the same region. I follow Cassano et al. (2013) in calculating the uncertainty on the flux density, using

:

$$\sigma_{MH} = \sqrt{(\sigma_{cal} S_{MH})^2 + \left(rms\sqrt{N_{beam}}\right)^2 + \sigma_{sub}^2}, \tag{5.1}$$

where $\sigma_{cal}$ is the fluxscale uncertainty (determined to be 10% for these observations, see Section 4.6), $S_{MH}$ is the measured mini-halo flux density, rms is the local root mean square value of the respective image and is scaled by $N_{beam}$ (the number of image beams contained within the mini-halo region). The last term quantifies the uncertainty due to the subtraction of the contaminating sources, given by:

$$\sigma_{sub}^2 = \sum_{s=1}^{N} \left(I_{MH,s} \times N_{beam,s}\right)^2, \tag{5.2}$$

where $I_{MH,s}$ is the mean surface brightness of the mini-halo within the $s^{th}$ source region and $N_{beam,s}$ is the number of beams within that region. Since mini-halos usually have non-spherical morphology, I follow Cassano et al. (2007) in measuring the average diameter of the diffuse emission as

$$D_{MH} = \sqrt{D_{min} \times D_{max}}, \tag{5.3}$$

where $D_{min}$ and $D_{max}$ are the minimum and maximum diameters of the $+3\sigma$ contours. Note that $D_{max}$ is the same as the largest linear size (LLS). I measure the BCG flux and associated uncertainty in the same manner but derived from the HR images with zero subtraction uncertainty. Table 5.1 shows the resulting measurements.

## 5.2 Integrated spectra, spectral index maps and radio powers

No spectral index maps are available for the mini-halos in our sample, so I generate them for the first time with this MeerKAT data. I used the 3GC sub-band images to analyse both the unsubtracted and SRC-SUB in-band spectral properties of each mini-halo; see Section 4.8 for how the spectral index maps were imaged.

The source subtraction was not controlled across the sub-bands; as such, the spectral index measurements near and within the BCG region in the subtracted images could be inaccurate. In

Table 5.1: Source measurements. Taken from Trehaeven et al. (accepted). Columns: cluster name, source, flux density at 1.28 GHz, average mini-halo diameter (to the nearest kpc), largest linear size (to the nearest kpc), spectral index, k-corrected radio power at 1.4 GHz.
* Sub-band maps convolved to 30″.
** Spectral index of the unresolved source S1+S2.
*** A large subtraction uncertainty in the flux density measurements due to the strong AGN causes a large uncertainty in the integrated spectrum.

| Cluster | Source | $S_{1.28\,\mathrm{GHz}}$ (mJy) | $D_{\mathrm{MH}}$ (kpc) | LLS (kpc) | $\alpha$ | $P_{1.4\,\mathrm{GHz}}$ ($\times 10^{24}$ W/Hz) |
|---|---|---|---|---|---|---|
| ACO 1413 | Mini-halo | 2.05 ± 0.27 | 185 | 211 | 1.52 ± 0.46* | 0.104 ± 0.014 |
| | BCG (S1) | 0.37 ± 0.05 | | | 0.89 ± 0.26** | 0.018 ± 0.003 |
| | S2 | 2.86 ± 0.29 | | | 0.89 ± 0.26** | 0.143 ± 0.015 |
| ACO 3444 | Mini-halo | 12.10 ± 1.71 | 372 | 412 | 1.53 ± 0.44 | 2.40 ± 0.40 |
| | BCG | 2.25 ± 0.24 | | | 0.61 ± 0.27 | 0.38 ± 0.04 |
| MACS J1115.8+0129 | Mini-halo | 7.91 ± 2.59 | 375 | 499 | 1.00 ± 1.10*** | 3.00 ± 1.20 |
| | BCG | 8.73 ± 0.88 | | | 0.78 ± 0.26 | 3.15 ± 0.40 |
| MACS J2140.2-2339 | Mini-halo | 2.61 ± 0.31 | 296 | 390 | 1.21 ± 0.36 | 0.79 ± 0.11 |
| | BCG | 1.43 ± 0.15 | | | 0.72 ± 0.31 | 0.39 ± 0.05 |

addition, the surface brightness subtraction uncertainty can easily be accounted for in the integrated spectra, but characterising such effects on the spectral index of a steep spectrum source after subtracting an embedded flatter spectrum source is beyond the scope of this work. Hence, I choose to take the average spectral index of the mini-halos as the integrated spectra of the subtracted data but display the unsubtracted spectral index maps. I note that for the SRC-SUB spectral index images to be of any use, the spectral properties of the compact and diffuse sources would most likely need to be evaluated across the sub-bands during the subtraction procedure to ensure that the underlying spectral distribution of the diffuse sources is conserved – which is beyond the scope of this work.

Due to the sensitivity loss compared to the MFS images, I increase the detection threshold to $5\sigma$, except for the ACO 1413 SRC-SUB images, in which I leave the threshold as $3\sigma$ to salvage a detection after the over-subtraction in the high-band. After measuring the mini-halo flux densities in each of the three sub-bands, I performed a power-law least squares regression with the `curve_fit` method of the `scipy.optimise` class across the central frequencies (998.52, 1283.79

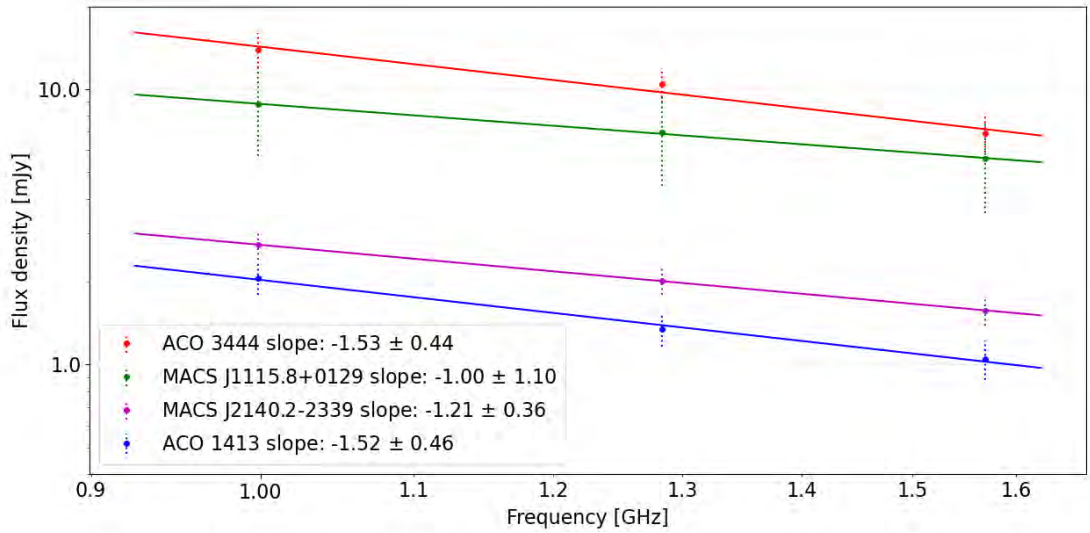


Figure 5.1: Mini-halo integrated spectra. All sub-band images were convolved to 15″ and flux densities measured within the 5$\sigma$ contour, except for ACO 1413, which were convolved to 30″ and measured within 3$\sigma$. Taken from Trehaeven et al. (2023).

and 1569.05 MHz) to produce in-band integrated spectra, which are shown in Figure 5.1. I can use this simplified fitting method as I do not have measurement uncertainties on the x-data. Then, as an initial test to produce manually derived spectral index maps, I fit the same relation to each pixel across the unsubtracted sub-band images, all at a 5$\sigma$ cutoff threshold relative to the respective local sub-band image noise and a 10% calibration uncertainty. These maps were then verified by generating automated maps using the Broadband Radio Astronomy Tools application (`brats`[1] Harwood et al., 2015, 2013). `brats` provides a variety of tools for the spectral analysis of radio data. I inputted the unsubtracted low and high sub-band images with the same cutoff and uncertainty as for the manual test. Both methods yield similar maps, but I use the `brats` maps as its uncertainty calculation is more robust. These maps are shown in panels d) and e) of Figures 5.2-5.5, and are the first spectral index maps for these mini-halos. I note that the indices spatially coinciding with the embedded sources are likely some weighted average between the embedded source and the underlying mini-halo, but disentangling the two components is beyond the scope of this work.

We used the slopes of the integrated spectra to calculate the k-corrected radio power of each individual mini-halo and BCG. K-correction 'corrects' for the fact that the object and observer are

[1]http://www.askanastronomer.co.uk/brats/

in different reference frames. It is typical in the literature to calculate the radio power of sources at 1.4 GHz, so I first scaled the measured flux densities using equation 4.4. We then calculate the 1.4 GHz k-corrected radio power by

$$P_{1.4\,\mathrm{GHz}} = \frac{4\pi(D_L)^2 S_{1.4\,\mathrm{GHz}}}{(1+z)^{\alpha+1}}, \tag{5.4}$$

where $D_L$ is the luminosity distance at redshift z, the denominator is the k-correction factor, and $\alpha$ is the slope of the integrated spectra. Error propagation was performed using the Python `uncertainties` package[2]. Table 5.1 shows the spectral index and radio power of each source.

## 5.3 Spectral tomography

As an aside, since the BCGs are embedded inside the mini-halo, I tried applying the technique of spectral tomography introduced by Katz-Stone & Rudnick (1997), which is used to identify and isolate overlapping spectral structures within extended objects. I experimented with this technique, knowing that I already have overlapping structures of differing spectral indexes, to see if any further spectral information could be gained. I found that no further scientific judgements can be deduced from the results of this technique; instead, they can serve to verify the results of the standard spectral mapping presented above. I describe the process below.

Spectral tomography involves generating a cube of radio continuum images, each with a different spectral component subtracted away. Mathematically, the following operation is performed at discrete intervals of $\alpha_t$:

$$I_{tom}(\alpha_t) = I_{low} - -\left(\frac{\nu_{low}}{\nu_{high}}\right)^{\alpha_t} I_{high}, \tag{5.5}$$

where $I$ is the surface brightness of the respective tomographic, low sub-band and high sub-band maps, $\nu$ is the central frequency of the respective low and high sub-band maps and $\alpha_t$ is the trial spectral index value corresponding to that image in the cube. I used the trial range 0-2 with steps

[2]https://pythonhosted.org/uncertainties/

of 0.01 to make the cubes such that each cube had 201 images (or slices) with $\alpha_t$ stepping in units of 0.01. When the $\alpha_t$ is correct, the spatial region corresponding to that value is perfectly subtracted, and the surface brightness goes to zero. To make the visualisation much easier, I condensed the cubes into a single image by iterating through the slices and selecting the spectral index that minimised the absolute value of $I_{tom}$ on a pixel-by-pixel basis.

For each cluster, the maps from both methods are almost identical, with a maximum spectral index difference of $< 0.01$ in any mutual pixel, adding validity to our spectral index maps, which will be presented in Chapter 6. The maps of the SRC-SUB mini-halos are equally identical. I leave the tomographic results out of the following discussions since they do not add new insights into the spectral analyses.

## 5.4 Mini-halo images

Here I present the images I used to derive the measurements mentioned above. For each mini-halo, in Figures 5.2-5.5, I show in panels (a) and (b) central cutouts of our standard resolution (`Robust 0`, ~8″) 3GC images before and after point source subtraction, respectively; (c) lower resolution (LR, 15″) images of the SRC-SUB cutout from which the mini-halo flux densities and sizes were derived, and (d) and (e) in-band spectral index and associated uncertainty maps of the unsubtracted central cutouts. The caption describes what is being displayed and a discussion and the interpretation of the results is given in the next Section.

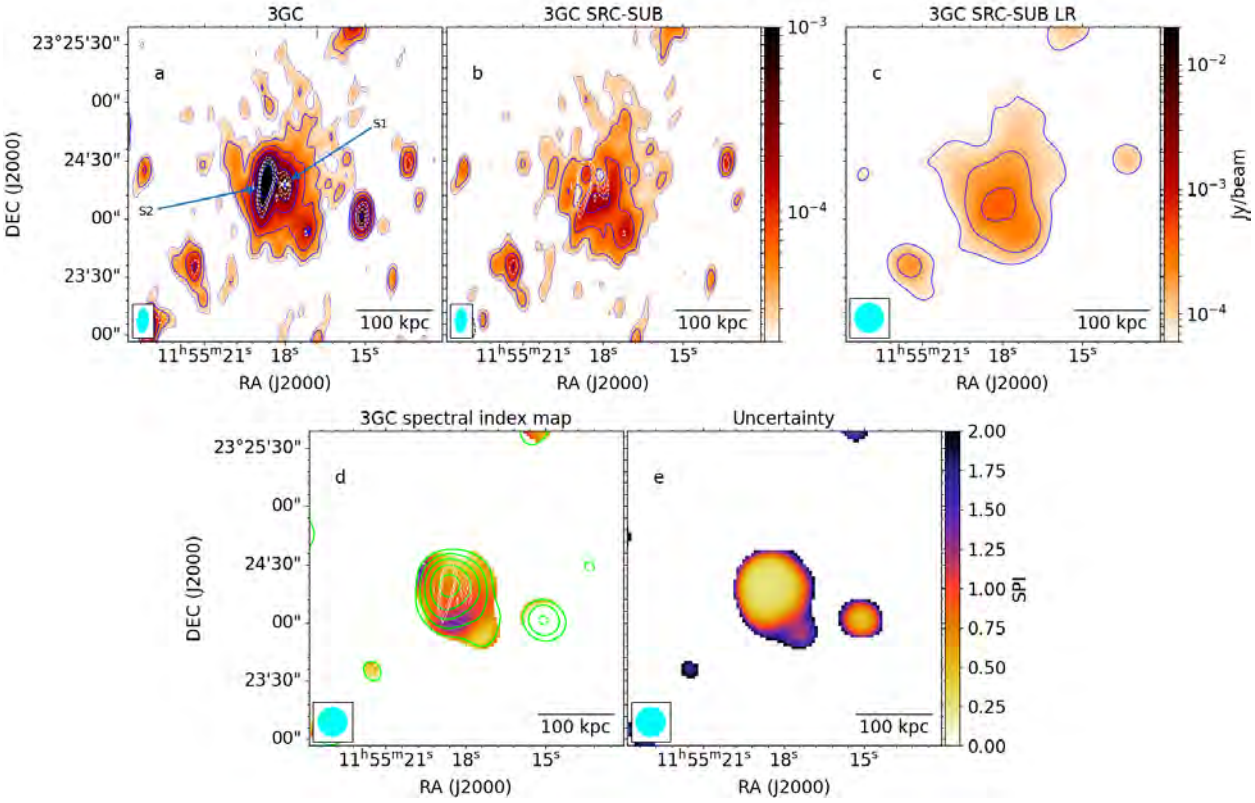


Figure 5.2: ACO 1413 mini-halo. a) beam size (12.2″, 5.9″, −4.5°), local rms $1\sigma$ = 11.2 $\mu$Jy/beam, S1 marks the BCG, S2 and a small blue cross indicate other projected galaxies. b) SRC-SUB image, beam size and colour scale same as a), local rms $1\sigma$ = 12.2 $\mu$Jy/beam. c) SRC-SUB 15″ LR image, local rms $1\sigma$ = 25.1 $\mu$Jy/beam. d) unsubtracted spectral index map, and e) uncertainty map. The beam is shown in cyan in the bottom left corner of the images. Dashed blue contours show the $2\sigma$ level, and the solid blue contours start at $3\sigma$ and increase by a factor of 2. Dashed black contours show the $-3\sigma$ level. White contours show the emission from the HR image, which has beam size (7.6″, 3.1″, −2.6°) and local rms $1\sigma$ = 23.0 $\mu$Jy/beam. Green contours in d) show the surface brightness of the SRC-SUB mid-band image, starting at $5\sigma$ and increasing by a factor of 2, where $1\sigma$ = 25.7 $\mu$Jy/beam. The white plus indicates the BCG position. Taken from Trehaeven et al. (2023).

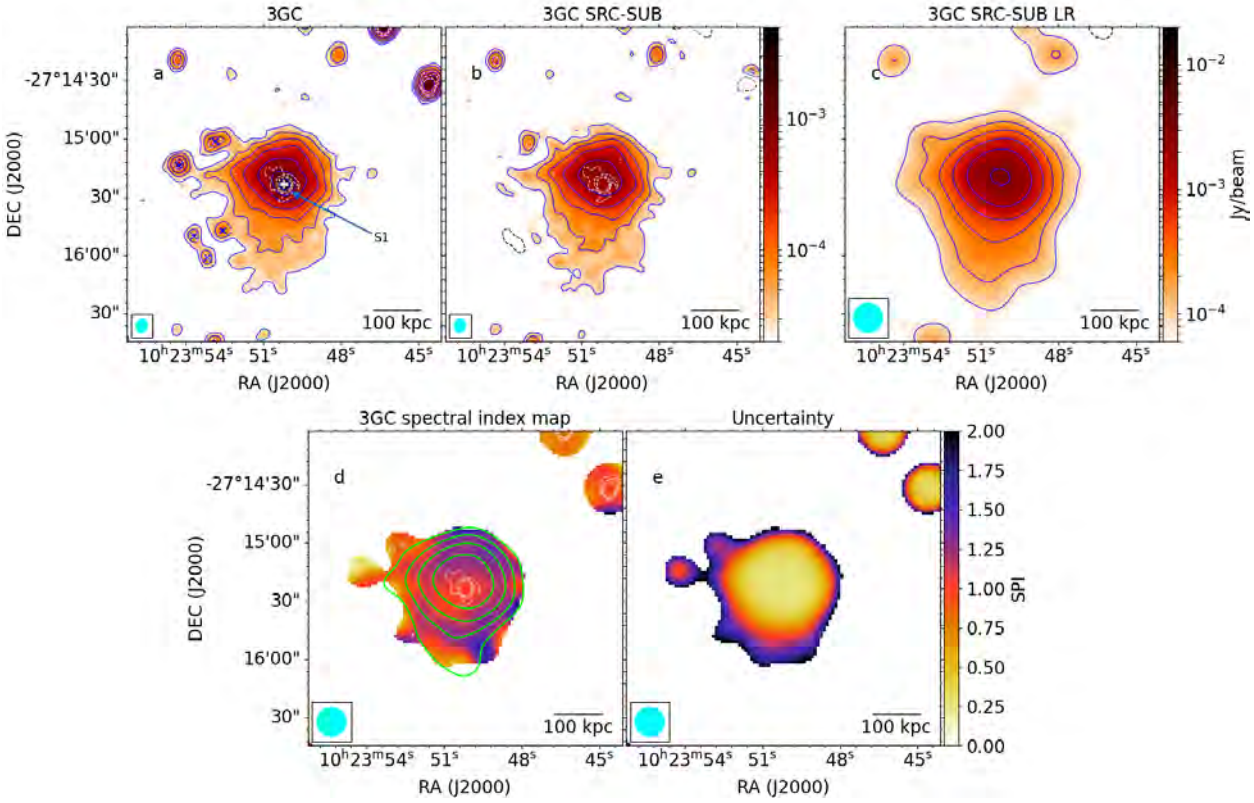


Figure 5.3: ACO 3444 mini-halo. a) beam size ($6.8''$, $5.9''$, $-16.0°$), local rms $1\sigma$ = 8.5 $\mu$Jy/beam, S1 marks the BCG, blue crosses indicate individual sources that were manually masked at HR. b) SRC-SUB image, beam size and colour scale same as a), local rms $1\sigma$ = 9.3 $\mu$Jy/beam. c) SRC-SUB $15''$ LR image, local rms $1\sigma$ = 27.8 $\mu$Jy/beam. d) unsubtracted spectral index map, and e) uncertainty map. The beam is shown in cyan in the bottom left corner of the images. Blue contours start at $3\sigma$ and increase by a factor of 2. Dashed black contours show the $3\sigma$ level. White contours show the emission from the HR image, which has beam size ($3.9''$, $3.2''$, $-9.6°$) and local rms $1\sigma$ = 20.9 $\mu$Jy/beam. Green contours in d) show the surface brightness of the SRC-SUB mid-band image, starting at $5\sigma$ and increasing by a factor of 2, where $1\sigma$ = 34.6 $\mu$Jy/beam. The white plus indicates the BCG position. Taken from Trehaeven et al. (2023).

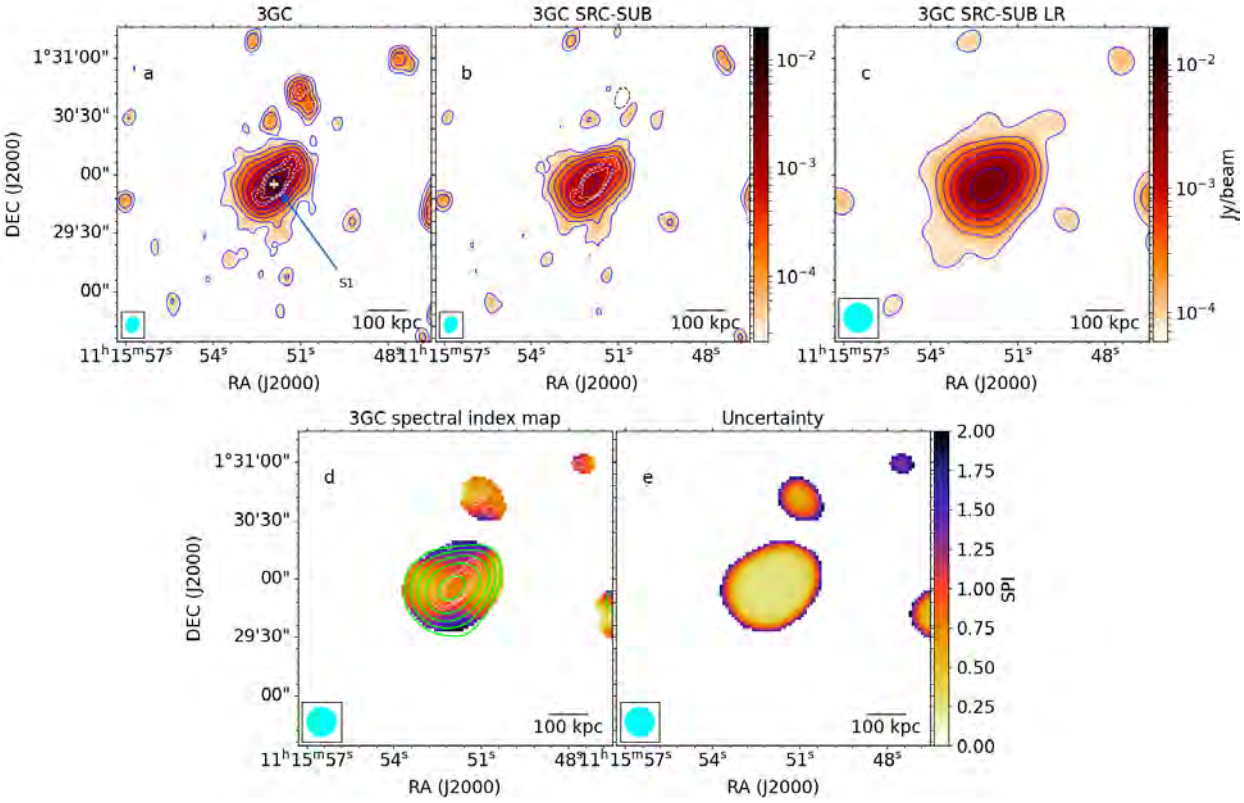


Figure 5.4: MACS J1115.8+0129 mini-halo. a) beam size $(8.5'', 6.5'', -16.2°)$, local rms $1\sigma$ = 10.2 $\mu$Jy/beam, S1 marks the BCG. b) SRC-SUB image, beam size and colour scale same as a), local rms $1\sigma$ = 10.9 $\mu$Jy/beam. c) SRC-SUB 15″ LR image, local rms $1\sigma$ = 24.6 $\mu$Jy/beam. d) unsubtracted spectral index map, and e) uncertainty map. The beam is shown in cyan in the bottom left corner of the images. Blue contours start at $+3\sigma$ and increase by a factor of 2. Dashed black contours show the $3\sigma$ level. White contours show the sources from the HR image, which has beam size $(4.5'', 4.0'', -39.3°)$ and local rms $1\sigma$ = 28.6 $\mu$Jy/beam. Green contours in d) show the surface brightness of the SRC-SUB mid-band image and start at $5\sigma$ and increase by a factor of 2, where $1\sigma$ = 31.8 $\mu$Jy/beam. The white plus indicates the BCG position. Taken from Trehaeven et al. (2023).

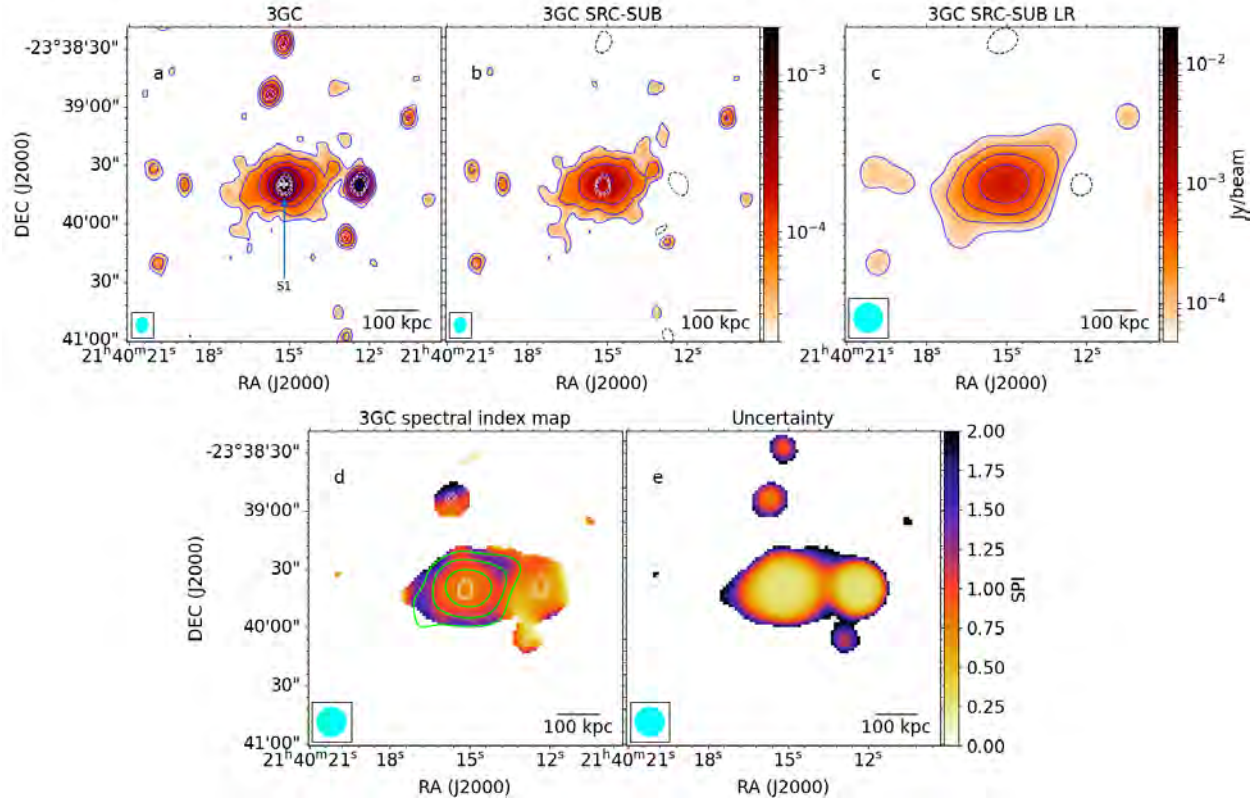


Figure 5.5: MACS J2140.2-2339 mini-halo. a) beam size $(7.8'', 6.2'', -8.6°)$, local rms $1\sigma$ = 8.0 $\mu$Jy/beam, S1 marks the BCG. b) SRC-SUB image, beam size and colour scale same as a), local rms $1\sigma$ = 8.7 $\mu$Jy/beam. c) SRC-SUB 15″ LR image, local rms $1\sigma$ = 20.4 $\mu$Jy/beam. d) unsubtracted spectral index map, and e) uncertainty map. The beam is shown in cyan in the bottom left corner of the images. Blue contours start at $+3\sigma$ and increase by a factor of 2. Dashed black contours show the $3\sigma$ level. White contours show the sources from the HR image, which has beam size $(4.3'', 3.2'', -7.1°)$ and local rms $1\sigma$ = 20.0 $\mu$Jy/beam. Green contours in d) show the surface brightness of the SRC-SUB mid-band image and start at $5\sigma$ and increase by a factor of 2, where $1\sigma$ = 22.8 $\mu$Jy/beam. The white plus indicates the BCG position. Taken from Trehaeven et al. (2023).

# Chapter 6

# Discussion

Here, I discuss our radio results in the context of our science case. This Chapter is based on the work presented in Sections 4 and 5 of Trehaeven et al. (2023). The 3GC procedure improved the image quality in most of our sample by reducing artefacts and lowering the background rms noise level allowing for more significant diffuse emission to be detected. Then, 2GC/3GC visibility-plane point source subtraction was applied to our sample to image the central mini-halos without bias from the BCG, and consistent results were found. Then, integrated spectra and spectral index maps of the point SRC-SUB and unsubtracted mini-halos were produced, respectively. Some of the presented measurements are the first to be measured for that object. Lastly, I see how our new measurements affect the current mini-halo vs BCG radio power correlation.

## 6.1 ACO 1413

Firstly, the presence of a mini-halo in ACO 1413 was suggested by Govoni et al. (2009) after studying VLA 1.4 GHz C-configuration data (maximum baseline 3.4 km with L-band resolution 14″). Giacintucci et al. (2017); Botteon et al. (2018) later classified ACO 1413 as a (borderline) nCC cluster using multiple *Chandra* observations, making it the first (and only) nCC cluster to host a (candidate) mini-halo. Savini et al. (2019) later confirmed the mini-halo presence with a 144 MHz LOFAR observation. The BCG has optical counterpart MCG+04-28-097.

Figure 5.2 shows the various mini-halo images for this cluster. Savini et al. (2019) first noted that two sources are embedded in this mini-halo, visible in panel a), marked as S1 and S2, where S1 is the BCG and S2 is identified as the radio source FIRST J115518.6+232422. I place a small blue cross in this panel southwest of the embedded sources to mark a localised peak identified as galaxy 2MASS J11551712+2323527, which is blended with the mini-halo. Panel b) shows the mini-halo with an irregular morphology, having holes of decreased surface brightness immediately adjacent to peaks in the diffuse emission. However, these holes are most likely due to the subtraction because they coincide with the subtracted sources and are not seen in either the VLA, LOFAR SRC-SUB, or the MeerKAT unsubtracted images. The mini-halo is orientated in the north-south direction, similar to the BCG, with the north having fainter filamentary-like emission only detected at $2\sigma$ at this resolution. Once smoothed, panel c), the morphology is comparable to that shown in Figure 6 of Savini et al. (2019). I measure a flux density of $S_{1.28\,\mathrm{GHz}} = 2.1 \pm 0.27$ mJy and an average diameter of 185 kpc with LLS of 211 kpc for this mini-halo. Using the measured in-band spectral index of $1.5 \pm 0.46$ (see below), the 1.4 GHz k-corrected radio power is $P_{1.4\,\mathrm{GHz}} = (1.04 \pm 0.140) \times 10^{23}$ W/Hz. This is the faintest mini-halo in our sample.

This mini-halo's spectral analysis is limited in sensitivity and resolution due to the clusters high declination giving a very elongated restoring beam and its unreliable source subtraction across the sub-bands. Concerning the latter issue, a ~50 kpc region of negative surface brightness was found at the location of source S2 in the high-band SRC-SUB image, where the corresponding low- and mid-band images showed non-negative surface brightnesses. Hence, to recover a measurement of the in-band spectrum, I convolved the subtracted images to $30''$ and computed the flux density inside the $3\sigma$ contours. I thus obtained an average spectral index of $\alpha_{1\,\mathrm{GHz}}^{1.5\,\mathrm{GHz}} = 1.5 \pm 0.46$, which is consistent with the value of ~1.3 (no uncertainty given) determined by Savini et al. (2019). Due to the poorer spatial resolution of these observations, sources S1 and S2 blended in the HR sub-band images to give one unresolved source at a $12''$ resolution. Hence, the spectral index quoted in Table 5.1 of $\alpha_{1\,\mathrm{GHz}}^{1.5\,\mathrm{GHz}} = 0.89 \pm 0.26$ is of this combined source (consistent with the typical index of 0.7 for compact radio sources). Panels d) and e) of Figure 5.2 show the cluster core region's radio

spectral index and uncertainty maps at a 15″ resolution. Sources S1 and S2 obscure the spectral distribution of the underlying mini-halo – and this is the case for all our spectral index maps.

Nevertheless, the spectral index of the entire radio core region is reliable within the central diameter of ∼100 kpc. Outside the embedded source regions, a possible gradient from north to south is visible, with a steeper spectrum of ∼1.3 in the south and a flatter spectrum of ∼0.4 in the north, perhaps suggesting that the northern arms mentioned above could be the result of some particle (re)-acceleration. The southern region may be a glimpse of the underlying mini-halo as it is not contaminated by any embedded sources and is roughly consistent with the SRC-SUB integrated spectrum. The blended source mentioned above causes a flatter spectrum to be visible in the southwest of the core. However, the larger uncertainty makes the spectral index in this region unconstrained.

## 6.2 ACO 3444

A candidate mini-halo in ACO 3444 was first reported by Venturi et al. (2007) based on a 610 MHz GMRT observation. Giacintucci et al. (2017, 2019) provided confirmation through analysis of archival VLA 1.4 GHz DnC+BnA configuration data – images restored to 5″ and 11″. The BCG has optical counterpart, 2MASX J10235019-2715232.

In panel a) of Figure 5.3, the central BCG is clearly visible, marked S1; however, also visible are five compact sources on the eastern edge of the mini-halo marked with blue crosses. These were identified from NED as respective infrared sources: WISEA J102352.68-271500.5, WISEA J102354.25-271513.4, WISEA J102352.62-271547.4, WISEA J102353.72-271548.8, and WISEA J102353.26-271601.1. The generic $4\sigma$ HR mask did not pick up these sources, so to subtract their radio emission, I manually added the $3\sigma$-significant pixels to the mask in Step 2 from Section 4.2.2. The last two sources were over-subtracted to significantly negative surface brightness. Thus, I urge caution when manually adding pixels to a mask, but this does not affect our mini-halo measurement. In panel b), the mini-halo extends further south than what was observed with the

VLA, similar to the GMRT observation. When convolved to the same 11″ resolution used in Figure 5b of Giacintucci et al. (2019), the MeerKAT image shows the mini-halo extending ∼100 kpc further south. This shows the ability of the MeerKAT to detect fainter L-band emission at a higher significance, especially considering that the VLA observation had twice as much on-target exposure time. Since the extension is partially seen in Figure A4 of Venturi et al. (2007), it may have a particularly steep spectrum. Panel c) shows some of the residual diffuse emission associated with the northern-most infrared source mentioned above blending with the mini-halo. However, its contribution to the measured flux density because the excess emission is of very low surface brightness ($\sim 10^{-4}$ Jy/beam), and did not affect the measured size because it is not aligned with the directions of $D_{max}$ and $D_{min}$. I determine a flux density of $S_{1.28\,\mathrm{GHz}} = 12.1 \pm 1.56$ mJy, and an average diameter of 372 kpc with LLS of 412 kpc. The extension adds another ∼130 kpc onto the diameter reported by Giacintucci et al. (2019) and ∼60 kpc onto the Venturi et al. (2007) LLS; while the flux density is consistent with that presented in Giacintucci et al. (2019). This makes sense because of the extension's low surface brightness. Using the measured in-band spectral index (see below), the k-corrected radio power is $P_{1.4\,\mathrm{GHz}} = (2.40 \pm 0.4) \times 10^{24}$ W/Hz, consistent with Giacintucci et al. (2019). However, the BCG flux density is significantly higher at both 2GC and 3GC, so the variation in measurements may result from differences in HR imaging.

In the spectral analysis of this core region, much of the southern extension is not reliably detected and progressively recedes in the higher parts of the band (a point that also suggests a steep spectrum). The integrated spectra for the remaining region gives $\alpha_{1\,\mathrm{GHz}}^{1.5\,\mathrm{GHz}} = 1.5 \pm 0.44$, and $\alpha_{1\,\mathrm{GHz}}^{1.5\,\mathrm{GHz}} = 0.61 \pm 0.27$ for the BCG (their first L-band measurements). In panel d) of Figure5.3, due to the contaminating infrared sources, much of the eastern edge of the mini-halo has a flat spectrum, while most of the remaining region outside the BCG has an index consistent with the integrated spectrum.

## 6.3 MACS J1115.8+0129

Pandey-Pommier et al. (2016) reported in MACS J1115.8+0129 the presence of a mini-halo via the analysis of low-frequency GMRT observations. Giovannini et al. (2020) later confirmed its presence through a short JVLA 1.5 GHz D-configuration observation (maximum baseline 1.03 km with L-band resolution 46″). In this poor-resolution data, the central source blended with the diffuse emission and hence the properties of any diffuse structures could not be determined. The authors give the total flux density of the entire compact+diffuse emission. They compare their total flux density to that of the high-resolution FIRST counterpart and cite the difference as evidence for a radio mini-halo. Thus, I present the first direct image of this mini-halo. The BCG has optical counterpart SDSS J111551.90+012955.0.

Figure 5.4a, b show the 3GC and 3GC SRC-SUB images for this cluster. The BCG is shown to have strong radio lobes smoothly orientated in the north-west/south-east direction, and with their removal, the mini-halo is also orientated in this direction. This connection may have implications on the production mechanism, which will be explored in Chapter 7. I note that there appears to be a hint of a radio arm or tail extending from the south, seemingly misaligned with the mini-halo emission. Such structures are seen in mini-halo simulations (ZuHone et al., 2013, 2015) as a result of the spiralling motion of the sloshing CC gas, although these are generally much more elongated and curved than that shown in panels a) and b). A further investigation into this feature is required before any conclusions or assumptions can be drawn. In panel c), the convolution blends feature with the rest of the mini-halo. In addition, some nearby excess low surface brightness radio emission joins with the mini-halo such that the LLS measurement is increased; thus, the sizes quoted in Table 5.1 for this mini-halo may be overestimated. The presence of the strong AGN causes the subtraction uncertainty on the measured mini-halo flux density to be very large, thus resulting in an even larger spectral index and radio power uncertainties (to the extent that the spectral index is unconstrained). I determine a flux density of $S_{1.28\,\mathrm{GHz}} = 7.91 \pm 2.55$ mJy (its first direct measurement), and an average diameter of 375 kpc with LLS of 499 kpc (first measurement).

The flux density of the BCG is consistent with that determined from the FIRST image presented by Giovannini et al. (2020), as is the sum of the radio core emissions (mini-halo+BCG). The scaled k-corrected radio power of the mini-halo is $P_{1.4\,\mathrm{GHz}} = (3.00 \pm 1.20) \times 10^{24}$ W/Hz, making it the most powerful in our sample and its first direct measurement.

The mini-halo integrated spectrum gives $\alpha_{1\,\mathrm{GHz}}^{1.5\,\mathrm{GHz}} = 1.0 \pm 1.1$ (the uncertainty being far too large to make any reasonable judgements on this measurement) while the BCG has $\alpha_{1\,\mathrm{GHz}}^{1.5\,\mathrm{GHz}} = 0.78 \pm 0.26$. Figure 5.4d, e show the unsubtracted spectral index map and associated uncertainty, showing a very interesting spectral distribution. Coupled with the AGN jet-like emission is a significant spectral flattening shown horizontally across the mini-halo; interestingly, the flattest spectral indices are not spatially coincident with any AGN emission, suggesting that a complex dynamical process is at play. The flattest indices of ∼0.5 are shown to be directly east and west of the AGN core, and the steepest of ∼1.5 directly north and south, while the AGN is orientated diagonally in-between these sets of indices.

## 6.4 MACS J2140.2-2339

MACS J2140.2-2339 is a highly X-ray luminous CC, massive cluster at redshift z = 0.313 (Ebeling et al., 2010), having $L_{X,500} = 11.1 \times 10^{44}$ erg s$^{-1}$ and $M_{500} = 4.7 \times 10^{14} M_{\odot}$. Radio observations of this cluster are scarce. Yu et al. (2018) produced a high-resolution image of the cluster BCG using a 1.5 GHz JVLA observation in A-configuration (maximum baseline 36.4 km with L-band resolution 1.3″). They measured a BCG flux density of $1.4 \pm 0.03$ mJy and quoted a $3.8 \pm 0.5$ mJy flux density from the NVSS counterpart. Giovannini et al. (2020) observed this cluster with a short JVLA 1.5 GHz observation in D-configuration, similar to MACS J1115.8+0129; however, a useful image could not be produced due to strong RFI. They cite the difference in flux density between the NVSS and JVLA measurements of Yu et al. (2018) as evidence for possible extended radio emission around the BCG. The MeerKAT's southern location, instrumentation and array layout make it the ideal telescope to observe this source and disentangle the compact and possible

diffuse radio emission. The BCG has optical counterpart 2MASX J21401517-2339398.

Figures 5.5a, b compare the 3GC vs 3GC SRC-SUB images. Diffuse emission is clearly evident around the BCG and satisfies all the criteria defining a radio mini-halo set out in Giacintucci et al. (2017). Thus, I classify this source as a new mini-halo detection. A high-redshift galaxy (CLASH MS2137-2353 830, z = 5.9, Bradley et al., 2014) is seen on the western edge of the mini-halo; however, it and the BCG are clearly removed after subtraction. The mini-halo then seems to be smoothly orientated in the east-west direction while having no AGN jet-like emission to influence its morphology; I compare these characteristics to that of MACS J1115.8+0129 in Chapter 7. There seems to be a hint of a pair of radio arms symmetrically opposite the core.

Figure 5.5c shows the 15″ LR 3GC SRC-SUB image. I determine a flux density of $S_{1.28\,\mathrm{GHz}} = 2.6 \pm 0.31$ mJy, consistent with the difference between the LR and HR measurements of Yu et al. (2018). I determine an average diameter of 296 kpc with an LLS of 390 kpc. The scaled k-corrected mini-halo radio power is $P_{1.28\,\mathrm{GHz}} = (0.79 \pm 0.11) \times 10^{24}$ W/Hz. The measured BCG flux density is consistent with that given in Yu et al. (2018).

The mini-halo integrated spectra gives $\alpha_{1\,\mathrm{GHz}}^{1.5\,\mathrm{GHz}} = 1.21 \pm 0.36$, while the BCG gives $\alpha_{1\,\mathrm{GHz}}^{1.5\,\mathrm{GHz}} = 0.72 \pm 0.31$. Figures 5.5d, e show the unsubtracted spectral index map and associated uncertainty. The BCG and western source obscure much of the underlying mini-halo spectral distribution. However, I can see that the spectral index monotonically increases radially outwards from ∼0.75 to ∼1.5.

Below I examine how our new measurements fit into and affect the mini-halo vs BCG radio power for the currently known sample.

## 6.5 Mini-halo vs BCG radio power

Govoni et al. (2009) first noted a tentative positive correlation between the mini-halo and BCG radio powers of five relaxed galaxy clusters. Later, Giacintucci et al. (2019) used an updated sample (23) to confirm the positive correlation but found that the strength was weak-to-moderate. There

are several statistical methods to test the strength of a particular correlation. The relationship between mini-halo and BCG power is expected to be monotonic, meaning that if one increases (decreases), the other also increases (decreases). The Spearman's Rank Correlation Coefficient is used to test such a correlation and was used by the authors mentioned above. The result of the test is a coefficient $r_S$ lying in the range [-1,1]; the magnitude of the coefficient describes the strength of the correlation, where -1, 0, 1 describe a perfectly negative, the absence of any, and perfectly positive monotonic relationship respectively. Along with the coefficient, the test outputs a probability $\rho_S$ measuring how likely uncorrelated quantities are to produce a coefficient at least as extreme as the one outputted (i.e. a false positive).

We add our measurements to the sample presented in Giacintucci et al. (2019), which includes ACO 3444, to see where our sample lies within the broader sample of confirmed mini-halos. I note that a few new mini-halos have been detected since the findings of Giacintucci et al. (2019), particularly in Richard-Laferrière et al. (2020); Knowles et al. (2022), but in these cases, the BCG power was either decomposed in a manner that is outside the scope of this work or not given. Nevertheless, I calculate the Spearman's coefficient for our combined sample of 26 confirmed mini-halos using the `scipy spearmanr` function. Similar to a study presented in Richard-Laferrière et al. (2020), I describe the relationship by performing a least squares regression, similar to that shown in Section 4.5, where now $x$ and $y$ represent mini-halo and BCG radio powers, respectively. Figure 6.1 shows the mini-halo versus BCG radio powers for the updated sample, with the associated fit.

From Figure 6.1, I can see that our measurements comfortably lie within the middle-to-low range of the known sample and follow the general positive-monotonic trend. The ACO 3444 mini-halo power is almost the same as that presented in Giacintucci et al. (2019), but the BCG measurement presented here is slightly higher. ACO 1413 is found to have the second smallest mini-halo and BCG powers from this sample. The Spearman test gives a coefficient of $r_S = 0.50$ and probability of no correlation $\rho_S = 0.007$, suggesting a moderately positive correlation between the two variables with $< 1\%$ probability of a false positive – a slightly stronger correlation than that determined by Giacintucci et al. (2019) ($r_S = 0.43$, $\rho_S = 0.05$). The line of best-fit that minimises

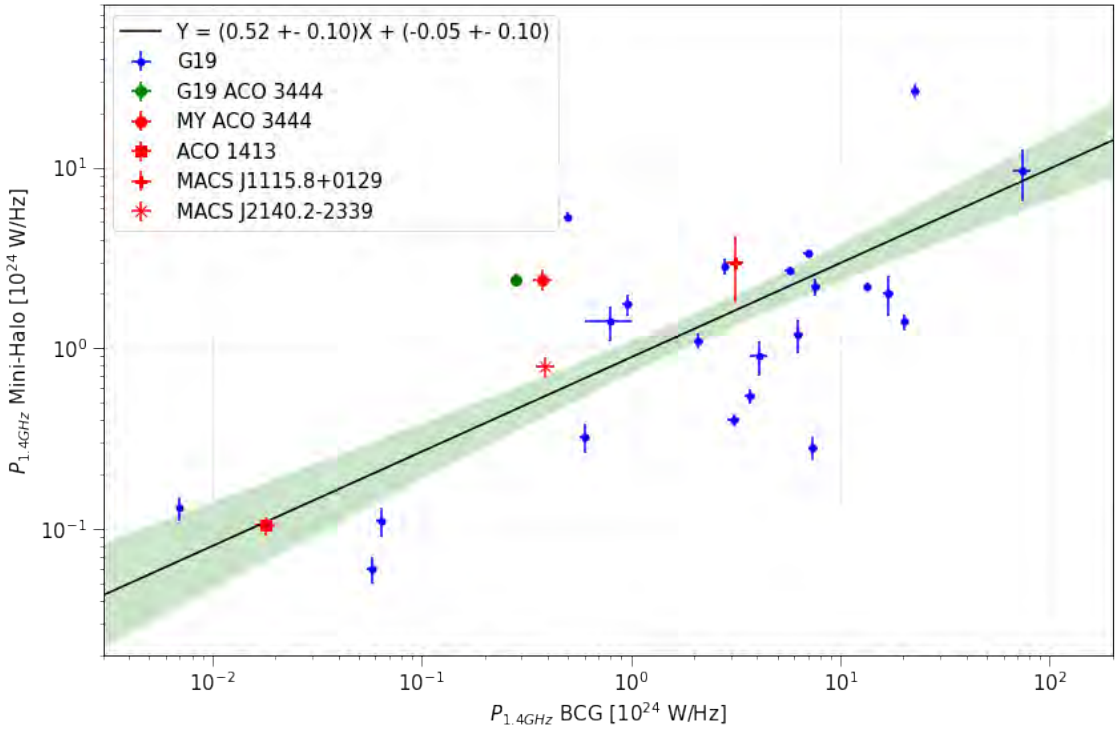


Figure 6.1: Mini-halo vs BCG 1.4 GHz radio power for a combined sample of 26 confirmed mini-halos from Savini et al. (2019) and this work. Blue points show the Savini et al. (2019) sample, where their ACO 3444 measurement is green, and red points show our sample. The line-of-best-fit for the combined sample is given in the legend, where $Y = \log_{10}(y)$ and $X = \log_{10}(x)$, and its $2\sigma$ confidence interval is shaded in green.

the orthogonal distances of the measurements is determined to be

$$\log_{10}(P^{MH}_{1.4\,\mathrm{GHz}}) = (0.52 \pm 0.10)\log_{10}(P^{BCG}_{1.4\,\mathrm{GHz}}) + (-0.05 \pm 0.10). \tag{6.1}$$

We note that, remembering that mini-halo formation theory suggests that the BCG is a likely source of either 'seed' electrons which are later (re)-accelerated or CR protons which collide with thermal protons to produce relativistic electrons as secondary particles, the line of best-fit that assumes the BCG radio power as the independent variable is consistent with the above relation.

Richard-Laferrière et al. (2020) performed a similar study but decomposed the BCG power into a core component which describes ongoing AGN accretion/feedback from the core and a steep component which describes the aged feedback or the jets/lobes and found a moderate positive correlation in each case. Such a decomposition is beyond the scope of this work. However, I

note that the Spearman coefficient presented in this work is slightly lower than that presented for the individual BCG components in Richard-Laferrière et al. (2020), especially that of the core ($r_S^{core} = 0.57$, $r_S^{steep} = 0.53$), suggesting that the core component directly affects the mini-halo to a higher degree than the steep component and the combination thereof.

As a final aside, I notice that for most of the sources in our sample, the mini-halo orientation roughly follows that of the BCG both before and after subtraction. This could be the result of the fundamental role that the BCG plays in the production of the mini-halo emission, possibly being the source of a population of seed relativistic electrons and/or protons which are then (re)-accelerated and (re)-distributed by turbulence and/or hadronic collisions (e.g., Brunetti & Jones, 2014). Since diffusion and other transport mechanisms can only spread relativistic electrons to a maximum of ~50 kpc within their radiative lifetime (Giacintucci et al., 2017) and the mini-halos extend well beyond this limit, I find it unlikely that the above connection is caused by a failure in the subtraction to properly disentangle the BCG and mini-halo emissions, but do not completely dismiss this possibility

# Chapter 7

# Multi-Wavelength Test Case: MACS J1115.8+0129 vs MACS J2140.2-2339

In this chapter, I combine the radio data from the previous chapter with X-ray data to present a multi-wavelength case study. In the interest of time, I focus our study on MACS J1115.8+0129 and MACS J2140.2-2339. I noticed that these two mini-halos both have a preferential orientation and follow the mini-halo-BCG radio power relation found in Section 6.5. However, one has strong AGN jet-like emission while the other does not. Is there a common feature or mechanism shaping these mini-halos? To investigate the overall gas dynamics, I present a point-to-point analysis of the cluster CC radio and X-ray surface brightnesses. Such analyses have become popular in recent publications because of the implications that the results can have on the relationship between the non-thermal and thermal components of the host cluster and, ultimately, the mini-halo production mechanisms.

## 7.1 Radio vs X-ray surface brightness

As mentioned in Chapter 2, two possible scenarios exist in the literature to explain the (re)-acceleration of CRe over the mini-halo extent, namely, turbulent (re)-acceleration models and/or hadronic collision models, but neither is entirely satisfactory. A common aspect they share is the

physical connection between the CRe and thermal plasma (Richard-Laferrière et al., 2020). In the first model, the plasma is a background medium that experiences the turbulence that (re)-energises the seed electrons to ultra-relativistic energies; in the second model, the plasma constitutes the targets for the hadronic collisions. This connection should mean that the thermal and non-thermal emissions occupy a similar volume and that a spatial correlation between the radio and X-ray surface brightnesses may exist. Such a correlation has been applied to the case of giant radio halos (e.g., Pfrommer et al., 2008; Brunetti & Jones, 2014), and is now being explored in mini-halos (e.g., Govoni et al., 2001; Timmerman et al., 2021). Simulations by ZuHone et al. (2013, 2015) show that these models produce radio surface brightness distributions that peak and fall with respect to the X-ray surface brightness at different rates when the different particle (re)-acceleration mechanisms are employed. Mathematically, this is expressed as different the power-law indices (k) between the radio ($I_R$) and X-ray ($I_X$) surface brightness:

$$I_R = A I_X^k, \tag{7.1}$$

which transforms into the form of equation 4.1 in log-log space.

It is generally expected (Dolag & Enßlin, 2000; Pfrommer et al., 2008) that hadronic models produce a non-thermal radio component that increases and decreases in intensity more rapidly than the X-ray distribution, expressed by a super-linear power-law index (i.e. $k > 1$). In turbulent (re)-acceleration models, the $I_R - I_X$ correlation is sensitive to the way turbulence is generated in the plasma and how relativistic particles are accelerated and transported in that turbulence. Therefore, a super- or sub-linear slope (i.e. $k < 1$ or $k > 1$) can be expected (Ignesti et al., 2020; Riseley et al., 2022a). Hence, by calculating the value of k for the CC region, I can understand and hopefully discriminate between the two models and test whether the hadronic model holds for or is broken ($k < 1$) by the data. However, it is important to consider the possibility of complex magnetic fields and CRp densities. It is possible for the dynamical interactions of the cluster core, its cold-fronts and the surrounding environment to create such phenomena and therefore yield unexpected correlation slopes (Ignesti et al., 2020; Timmerman et al., 2021, e.g., ). Simulations of

such exotic configurations have yet to be explored, so a measurement of $k < 1$ may not be sufficient to completely reject the hadronic model, in that case, (Riseley et al., 2022a).

Ignesti et al. (2020); Ignesti (2022); Biava et al. (2021); Timmerman et al. (2021); Riseley et al. (2022a) have performed point-to-point analyses for a total of eight mini-halos (almost a quarter of the known mini-halo sample). Always a strong positive correlation with k $\gtrsim$ 1 has been found, which tells us that the radio and X-ray emissions are likely physically connected and either the hadronic and/or turbulent (re)-acceleration models can be responsible in these cases. The shallowest slope has come from the Phoenix mini-halo presented in the Timmerman et al. (2021), $k = 0.84 \pm 0.23$, but its considerable uncertainty cannot rule out the possibility of a super-linear slope. I perform a similar analysis for MACS J1115.8+0129 and MACS J2140.2-2339, for which I first need to image the X-ray emission of the cluster core for each case.

## 7.2 Chandra observations and data analysis

Both clusters have archived Chandra observations on the Advanced CCD Imaging Spectrometer (ACIS) instrument. All observations used in this analysis are listed in Table 7.1. No detailed X-ray surface brightness analysis of these clusters can be found in the literature. So I use the Chandra Interactive Analysis of Observations (CIAO, Fruscione et al., 2006) package[1], version 4.14, to reprocess the data. I describe the data analysis below:

We searched for, downloaded and performed initial reprocessing of the individual Chandra observations using the `find_chandra_obsid`, `download_chandra_obsid` and `chandra_repro` tools. Then, for each observation, I created a light curve of the initial event counts versus time using the `dmextract` tool, grouping the counts in periods of 100 seconds. From these light curves, I deflared each observation to remove periods of abnormally high (or low) counts using a $3\sigma$ clip in the `lc_sigma_clip` routine of the `deflare` tool. Figure 7.1 shows an example of an outputted light curve – all blue points are removed from the dataset, and the resulting clean exposure times

[1] `https://cxc.cfa.harvard.edu/ciao/`

Table 7.1: Chandra X-ray archival observation details. Columns: cluster name, observation ID, observation exposure time, clean exposure time.

| Name | ObsID | Exposure time (ks) | Clean exposure time (ks) |
|---|---|---|---|
| MACS J1115.8+0129 | 3275, 9375 | 15.9, 39.6 | 13.9, 39.3 |
| MACS J2140.2-2339 | 928, 4974, 5250 | 43.6, 57.4, 40.5 | 35.4, 48.5, 36.1 |

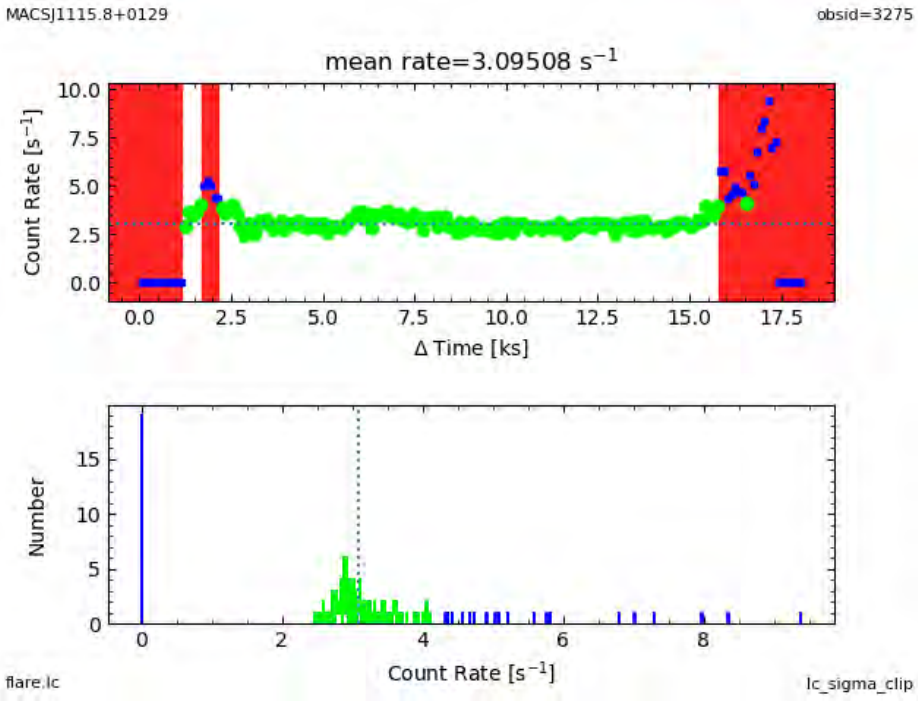


Figure 7.1: Deflare plot for OBSID 3275. *Top:* light curve of count rate versus time. Red regions show the time intervals that are removed from the dataset. *Bottom:* histogram of count rates. The vertical dotted line in the bottom plot shows the position of the mean count rate. Green and blue represent the data determined to be within and outside of the $3\sigma$ range of the mean count rate.

for each observation are given in Table 7.1.

We merged the cleaned data from each observation using the `merge_obs` tool, which automatically reprojected and combined them to create count (units: number of photons) and exposure (units: cm$^2$seconds) maps for each target. The resulting images had an effective pixel scale of 0.492″ (corresponding to the standard ACIS pixel size) in the energy band 0.5-2 keV, and combining the PSF maps by weighting each pixel by the fraction of its cleaned exposure time to the total merged clean exposure. Then, in preparation for point source detection (and their eventual removal), I minimised the PSF maps at each pixel using the `dmimgfilt` tool. I then used these

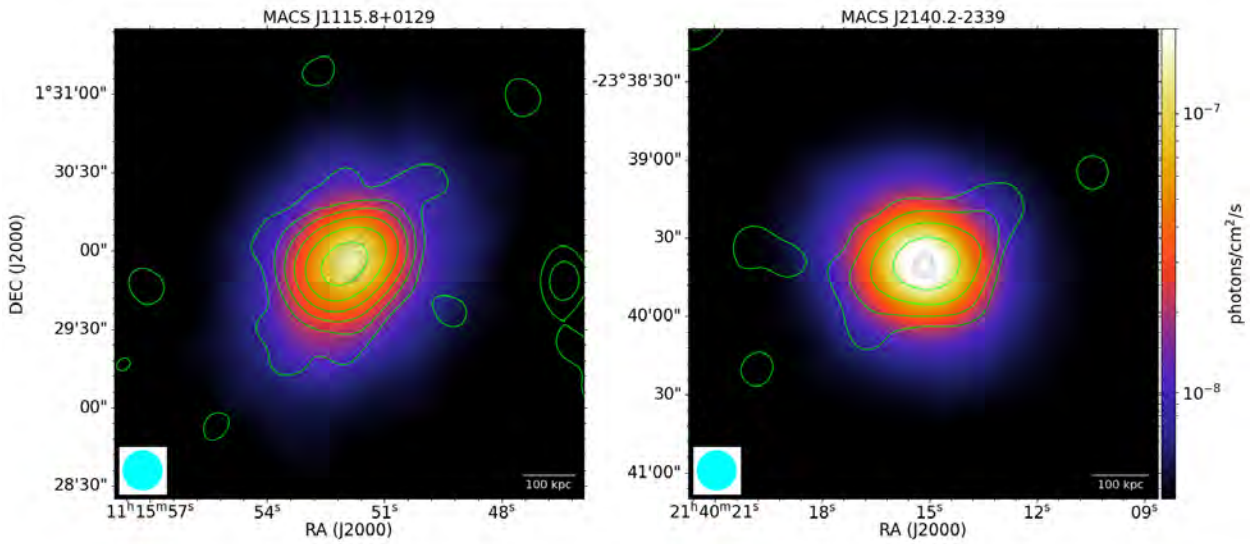


Figure 7.2: X-ray surface brightness for MACS J1115.8+0129 (*left*) and MACS J2140.2-2339 (*right*). The colour scale is stretched onto an arcsinh function. Green contours show the mini-halo from Figures 5.4c and 5.5c, respectively, with the radio beam in the bottom left corner. Dashed black contours show the HR point sources given by dashed white contours in Figures 5.4a and 5.5a.

PSF maps in the `wavdetect` tool to detect point sources in the count images on scales of 2, 4 and 8 pixels. I removed from the outputted source region files any regions corresponding to the BCGs and other detections within the core X-ray emission to preserve the core region for the point-to-point analysis. Then using the `dmfilth` tool and its 'DIST' interpolation method, I replaced the count values in the remaining point source regions with a distribution of pixel values from a background region containing no detected point sources. Finally, to produce exposure-corrected images in units of photons/cm$^2$/s, I divided the SRC-SUB count maps by the exposure maps. To allow for the comparison of the emissions on the same spatial scales, I convolved and regridded the final X-ray images using CASA's `imgrid` task to match the resolution and world co-ordinates (wcs) with the corresponding radio images. Figure 7.2 shows these images for both clusters with radio contours overlaid. I decided to neglect the contribution of the Chandra background noise to the individual observations because it should be sufficiently small to not significantly affect the analysis.

The above procedure is summarised below:

1. *Find, download and reprocess each observation,*
2. *Deflare,*
3. *Merge observations,*
4. *Make minimised merged PSF map,*
5. *Detect sources,*
6. *Remove BCG from the source list,*
7. *Interpolate over remaining sources, and*
8. *Divide resulting counts image by exposure map*

## 7.3 Point-to-point analysis

We used the Point-to-point TRend Extractor program, `PT-REX`[2] (Ignesti, 2022), to perform the point-to-point analysis. The program automates the study of spatial correlations between different emissions by generating a mesh of cells, calculating the surface brightness of each emission in each cell above a certain threshold and fitting the data points to equation 7.1. If contaminating sources are present in the field, the program can generate a mask from a given region file to exclude them from the analysis. Most importantly, it can perform any specified number of Monte Carlo iterations of the analysis, each time shifting the mesh by a random number of pixels within the given region to obtain a distribution of all possible spatial correlations, thereby eliminating any bias caused by the choice of sampling grid. All that is required as input is the SRC-SUB radio and X-ray counts and exposure images, a mask, the source region file and the radio surface brightness rms and detection threshold.

To ensure adequate SNR in both the radio and X-ray while still allowing for maximum statistics, I chose cells of size 11 pixels a side – corresponding to the number of pixels that make up

[2]https://github.com/AIgnesti/PT-REX

the area of one radio beam. I further chose the threshold to be three times the local radio rms and arbitrarily masked the entire field outside the local neighbourhood as shown by the grey shaded regions in Figure 7.3. I chose to perform the fit using the BCES orthogonal method that `PT-REX` provides as default (similar to Section 4.5). I perform 500 Monte Carlo iterations and take the mean and standard deviation of the resulting distribution as the final value of k and its (statistical) uncertainty.

Once the program has loaded the images, mask and source region file, it generates a square grid of cells starting from a random pixel position within the given source region – an example is shown in Figure 7.3. Each Monte Carlo iteration generates a new single mesh (SM) within the same region but initialised at a different random position. Then, for each iteration, for each cell, it calculates the radio surface brightness by dividing the CASA `imstat` flux density measurement by the cell area, and rejects the cell if its surface brightness is less than the threshold specified or if any of the cell is spatially coincident with the mask. The radio uncertainty is calculated as the statistical uncertainty of the cell emission (similar to the second term of equation 5.1) divided by the beam area. The X-ray component is calculated for the remaining cells by taking the sum of the count values divided by the mean of the exposure map (the same as Step 8 above) and dividing by the cell area. The X-ray uncertainty is assumed to follow a Poisson distribution and is calculated as the square root of the counts, divided by the exposure and the cell area. A final sanity check is performed to ensure that the radio and X-ray surface brightness are both non-negative and constrained by the corresponding uncertainties. Once all cells in a single mesh have been considered, its measurements are fitted like in Section 4.5. The k value determined for a single Monte Carlo iteration is drawn from the normal distribution having a mean and standard deviation of the fitted value. The next Monte Carlo iteration is processed until all iterations have been completed. The final slope of the spatial correlation is taken as the mean and standard deviation of the drawn samples of k.

The above procedure is summarised below:

1. *Provide all required inputs,*

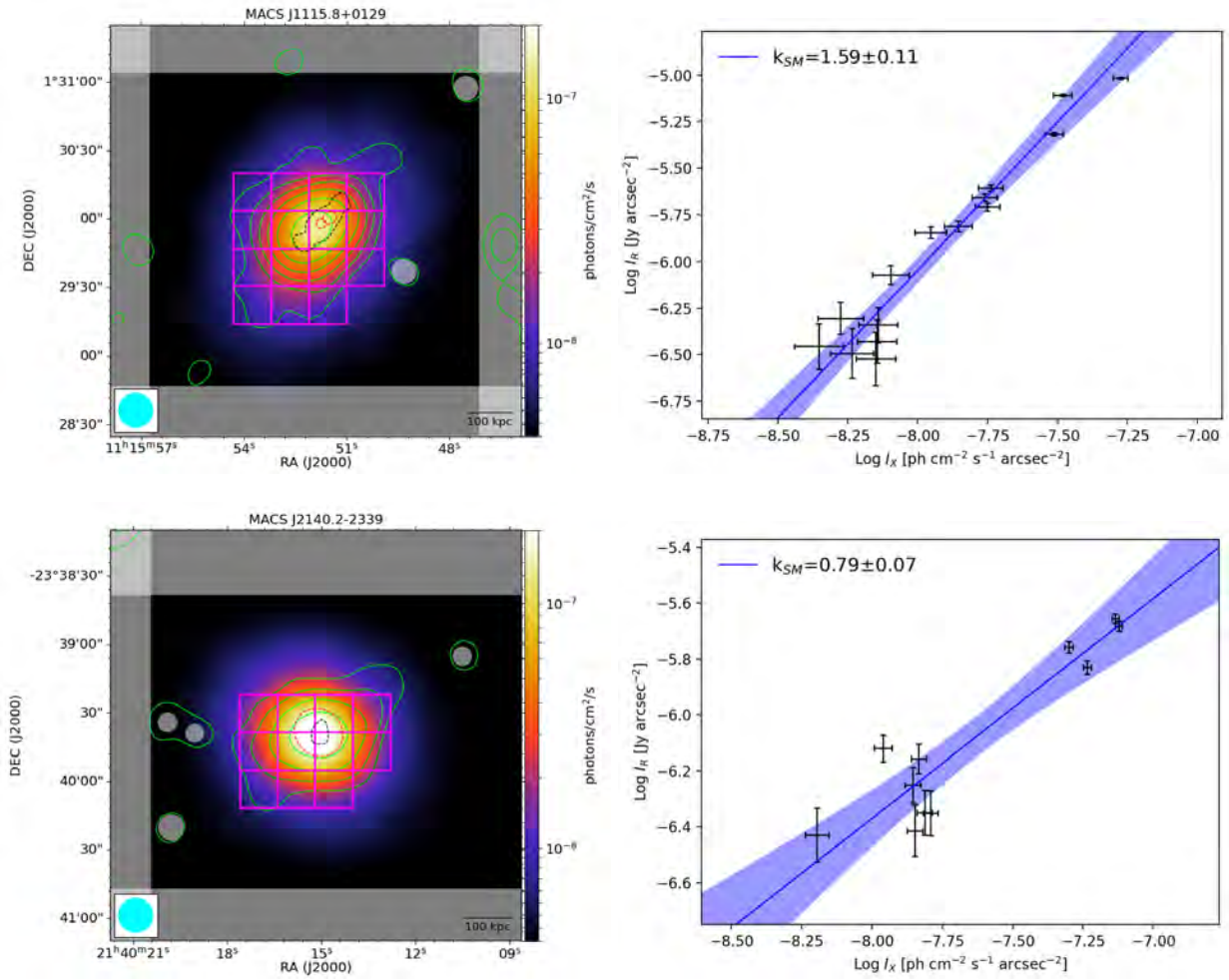


Figure 7.3: MACS J1115.8+0129 (*top*) and MACS J2140.2-2339 (*bottom*) SM examples. *Top Left:* same as Figure 7.2 (*left*) plus an example SM overlaid in magenta and the X-ray `wavdetect` source regions in red shown to be much smaller than the radio AGN. All regions masked out of the analysis are shaded in grey. *Top Right:* each point corresponds to the measurements within a cell on the *left*. The blue line shows the best fit, and the blue shaded area shows the $2\sigma$ confidence interval. *Bottom* is the same as *top* but for MACS J2140.2-2339. Here, the `wavdetect` region is much larger than the radio AGN contour, affecting four cells.

2. *Generate randomly initialised SM,*

3. *Calculate radio and X-ray surface brightness and uncertainties for all valid cells,*

4. *Fit data points,*

5. *Draw the value of $k_{SM}$,*

6. *Repeat Steps 2-5, and*

7. *Final Monte Carlo slope, $k_{MC}$, calculated as mean and standard deviation of resulting $k_{SM}$ distribution.*

For illustrative purposes, an example of a grid configuration and the resulting radio to X-ray surface brightness plane for a single Monte Carlo iteration for both clusters is shown in Figure 7.3. In these setups, the MACS J1115.8+0129 measurements have a Spearman coefficient and false-positive probability of $r_S = 0.94$ and $\rho_S = 2 \times 10^{-7}$, respectively, and MACS J2140.2-2339 has $r_S = 0.74$ and $\rho_S = 1 \times 10^{-2}$, respectively. MACS J1115.8+0129 has a stronger correlation which may be explained by the fact that the X-ray and radio emission seems to be orientated in the same direction while there is a slight anti-alignment in the MACS J2140.2-2339 emission. Additionally, I see that the radio emission in MACS J1115.8+0129 peaks at a higher surface brightness than in MACS J2140.2-2339, in which the X-ray peaks higher. In this regard, the super-linear slope for the former and a sub-linear slope for the latter makes sense as it confirms that the radio is more peaked than the X-ray in MACS J1115.8+0129, and vice versa for MACS J2140.2-2339 – most likely due to the difference in alignments mentioned above. The results of the full Monte Carlo runs are discussed below.

## 7.4 Results and discussion

The results of the final PT-REX runs for both clusters are shown in Figure 7.4. They are consistent with the SM example of Figure 7.3. The slope of the spatial correlations, $k_{MC}$, is super-linear for MACS J1115.8+0129 and sub-linear for MACS J2140.2-2339, which may point to a fundamental difference in production mechanism between the two mini-halos. The former has $k_{MC} = 1.51 \pm 0.08$ – with an average grid size of $16.3 \pm 1.3$ cells – suggesting that I cannot discriminate between the particle (re)-acceleration mechanisms in this case. However, the latter has $k_{MC} = 0.73 \pm 0.09$ – with an average grid size of $12.9 \pm 1.0$ cells – suggesting that it is unlikely for the hadronic model to play a significant role in this case.

Investigating the skewness of the distribution can lead to a more in-depth understanding of the

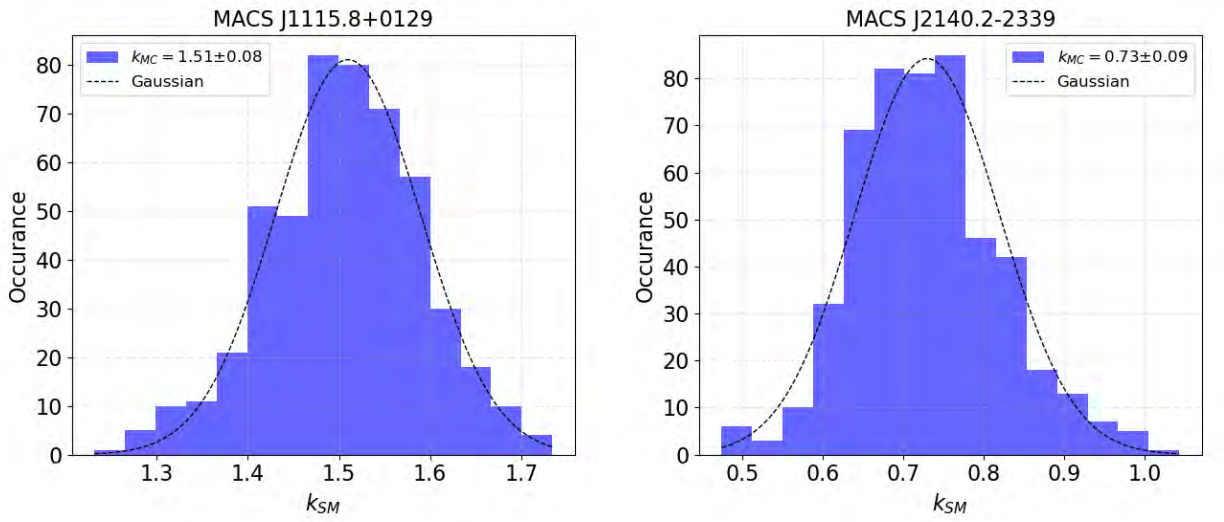


Figure 7.4: PT-REX results for MACS J1115.8+0129 (*left*) and MACS J2140.2-2339 (*right*). Plots are of a histogram showing the SM values for each Monte Carlo iteration. The mean and standard deviation of the distribution is given in the legend as $k \pm \Delta k$, and a Gaussian with those same values overlaid.

underlying emissions. Ignesti (2022) suggests that a negatively skewed distribution may indicate the presence of a secondary halo component of low radio surface brightness and/or strong X-ray point sources embedded in the radio emission. In contrast, positive skewness could be induced by the presence of point sources strong in both the radio and X-ray. The distributions for MACS J1115.8+0129 and MACS J2140.2-2339 show some asymmetry but not enough to draw any further definitive conclusions about the underlying emissions.

### 7.4.1 Limitations

Considering time constraints, I chose to quote only the statistical uncertainty of the slopes.

#### In the radio

We neglected the subtraction uncertainty since the embedded radio BCGs cover a total area of at most a single cell (less in the case of MACS J2140.2-2339), as seen by the dashed black contours in Figure 7.3). Hence, only one or two data points would be affected by the additional uncertainty

in each Monte Carlo iteration for each cluster – not enough to significantly affect the statistics. Nevertheless, when masking out the regions covered by the HR radio contours in each case, the fits remain, respectively, super-linear for MACS J1115.8+0129 (albeit with more considerable uncertainties) and sub-linear for MACS J2140.2-2339.

**In the X-ray**

Similar to the radio, I neglected the BCGs' contributions to the X-ray surface brightness (shown by dashed red contours in Figure 7.3). The source-detection, subtraction and interpolation of `wavdetect` and `dmfilth` used for the other field sources left the detected BCG region unusable for the point-to-point analysis, and accurately modelling the BCG's X-ray emission embedded within the larger thermal emission is beyond the scope of this work. However, given that the X-ray BCG region in MACS J1115.8+0129 covers a relatively small area, a similar argument can be made as in the radio for the inclusion of the BCG X-ray component (i.e. the affected area is too small to affect the statistics significantly. That said, the X-ray BCG regions, in this case, are suspiciously small. It may be possible that the source-finder did not find the true extent of the X-ray BCG because of the small number of counts in the comparatively shallow observations (the clean exposure time is around half that of MACS J2140.2-2339). Nevertheless, when masking the X-ray BCG regions from the analysis of MACS J1115.8+0129, the slope is consistent with that determined above.

For MACS J2140.2-2339, the diameter of the `wavdetect` BCG region is larger than the length of a single cell, big enough to cause three or four data points to be significantly affected in each iteration, which could be enough to affect the statistics due to the smaller grid size. When masking out this region, the slope remains sub-linear, albeit with much larger uncertainties. I expect to collaborate with the developers of `PT-REX` to include at least the radio subtraction uncertainty in the program.

# Chapter 8

# Summary, Conclusions and Future Work

In this Masters thesis, I described the data reduction used to produce 3GC, primary beam corrected, point source subtracted continuum images of a sample of five galaxy clusters observed by MeerKAT in L-band and presented the initial radio mini-halo science results derived therefrom. To give context to the reduction procedures used, I gave comprehensive overviews of the theoretical and observational history and open questions concerning mini-halos in Chapter 2 and the radio astronomy techniques needed to observe them in Chapter 3. Then in Chapter 4, I introduced the sample and described our use of CARACal (a new radio continuum pipeline with accompanying software specifically optimised for MeerKAT data) to reduce the observations through 1GC and 2GC, and killMS and DDFacet for 3GC. I discussed the improvements after 3GC and found a 7% improvement in global rms noise and a factor of three times improvement in $DR^{(2)}$ over 2GC. Unfortunately, I could not produce a science-worthy image for the galaxy cluster ACO 1795 due to residual sidelobe modelling errors originating from the bright BCG. I evaluated the fluxscale and the extent of flux suppression/absorption due to 3GC. Finally, I described the visibility-plane point source subtraction performed to disentangle the embedded radio galaxies from the underlying mini-halo emission and the effects thereof on the image quality, ultimately reducing the global image noise by 4%. Chapter 5 presented the mini-halo sizes, flux densities, radio powers, in-band spectral indices of the source subtracted mini-halos and in-band spectral index maps of the unsubtracted mini-halos. Chapter 6 discussed these results in the context of the known literature and

showed the images that were used to derive these properties; the highlights being the detection of a ∼100 kpc southerly extension to the ACO 3444 mini-halo and a new mini-halo in the cluster MACS J2140.2-2339. Finally, I presented a multi-wavelength case study between two complementary mini-halos from our sample. I showed by a point-to-point spatial correlation test that they might be formed by different particle (re)-acceleration mechanisms.

Further investigation is required into the following areas: (1) if observations of ACO 1795 by MeerKAT can produce valid scientific continuum images given the +50° difference in declination between the cluster and telescope, discussed in Section 4.4; (2) the cause of the occasional extreme flux suppression after 3GC, discussed in Section 4.5; (3) the cause of the noise amplification along the first negative sidelobe of the primary beam when imaging at HR, discussed in Section 4.7.1; (4) the spiral-like radio arms extending from the MACS J1115.8+0129 and MACS J2140.2-2339 mini-halos, as discussed in Sections 6.2 and 6.3; and (5), how to accurately model and subtract the BCG X-ray component from the thermal emission and include the subtraction uncertainties in both the radio and X-ray into the point-to-point spatial correlation, discussed in Section 7.4.1.

A proposal for MeerKAT UHF-band (544-1088 MHz) follow-up observations to those presented in this work was accepted during MeerKAT's third Open Time Call in mid-2022. These observations have been conducted with 4.5 hours of on-target time for each target in the sample. I also included polarisation calibrator scans to investigate the presence of any previously unknown polarisation properties. I intend to use this data to improve and extend the spectral analysis conducted in this work to characterise the mini-halos over a 1 GHz frequency range homogeneously. This includes, but is not limited to, confirming (or otherwise) the presence of the possible spectral gradient in ACO 1413 (Section 6.1), possibly detailing the spectral properties of the southern extension in ACO 3444 (Section 6.2); and, trying to understand what causes the spectral steepening in MACS J1115.8+0129 (Section 6.3). In this manner, I hope to constrain the mini-halo spectral index distributions further to try to understand and discriminate between the proposed production mechanisms discussed in Sections 2.1 and 2.2. I hope to combine the L-band, UHF-band and Chandra X-ray observations to extend the surface brightness spatial correlation test presented in

Chapter 7 to the rest of the sample and determine whether the slope of the correlation (k) changes significantly between the two central radio frequencies. Then, with an improved spectral study, I hope to perform a similar spatial correlation test, but between the radio spectral index and X-ray surface brightness, as discussed in Section 2.4. Last but not least, I hope to investigate the radial profile of radio vs X-ray surface brightness to determine whether there are any ultra-steep-spectrum secondary components to the mini-halos, as discussed in Section 2.5.

Our aim in this work was to convince the reader that further scientific investigation of radio mini-halos by MeerKAT is a worthwhile and exciting endeavour. With the description of our high-fidelity calibration and imaging, exciting initial science results, and follow-up observations already in hand, I have achieved our aims.

# Appendix A

# Software parameters

Here I list all the parameter specifications used in the calibration and imaging softwares mentioned in the main body of work; namely, CARACal, killMS, DDFacet and Quartical. All parameters were set to default except for those listed.

A note on WSClean. WSClean was only used outside of the CARACal pipeline when imaging ACO 1795 in conjunction with QuartiCal, and in these cases, parameters were set to mirror that of the CARACal values in order for the CubiCal vs Quartical imaging to be consistent.

Table A.1: CARACal parameters. Columns: parameter, value, notes. I used the continuum default script, found at `https://github.com/caracal-pipeline/caracal/blob/master/caracal/sample_configurations/meerkat-continuum-defaults.yml`, with the following exceptions.

| Parameter | Value | Notes |
|---|---|---|
| –flag-flag_mask-enable | False | All fields |
| –flag-flag_rfi-flagger | tricolour | All fields |
| –flag-flag_rfi-tricolour-mode | manual | All fields |
| –flag-flag_rfi-tricolour-strategy | stalin.yaml / gorbachev.yaml | Calibrator fields / Target fields |
| –transform-split_field-chan_avg | 5 | Target only |
| –selfcal-ncpu | 5 | |
| –selfcal-img_npix | 6000 | |
| –selfcal-img_cell | 1.5 | |
| –selfcal-img_niter | 1000000 | |
| –selfcal-img_nchans | 5 | |
| –selfcal-img_robust | 0 | |
| –selfcal-cal_niter | 3 | |
| –selfcal-cal_timeslots_chunk | -1 | |
| –selfcal-cal_cubical-madmax_flag_thr | [0, 10, 5, 3] | ACO 1795 only |
| –selfcal-start_iter | 1 | |
| –selfcal-img_specfit_nrcoeff | 2 | ACO 1795: 4 |
| –selfcal-img_multiscale | True | |
| –selfcal-img_nrdeconvsubimg | 1024 | |
| –selfcal-img_nwlayers_factor | 3 | |
| –selfcal-image-cleanmask_thr | [30, 15, 8, 3] | ACO 1795: [20, 10, 5, 3] |
| –selfcal-image-clean_cutoff | [0.5, 0.5, 0.5, 0.5] | |
| –selfcal-image-col | [DATA, CORRECTED_DATA, CORRECTED_DATA, CORRECTED_DATA] | |
| –selfcal-calibrate-model | [1, 2, 3] | |
| –selfcal-calibrate-gain_matrix_type | [GainDiagPhase, GainDiagPhase, GainDiagPhase] | ACO 1795: [Fslope, Fslope, Gain2x2] |
| –selfcal-calibrate-gsols_chan | [0, 0, 0] | |
| –selfcal-calibrate-gsols_timeslots | [30, 15, 3] | ACO 1795: [60, 30, 15] |

Table A.2: QuartiCal parameters. Columns: parameter, value, notes. I used the default values except for those stated below. Parameter values that change per self-calibration round are separated by "|".

| Parameter | Value | Notes |
|---|---|---|
| input_ms.sigma_column | None \| SIGMA_SPECTRUM \| SIGMA_SPECTRUM | |
| input_ms.time_chunk | 0 \|30\|60 | |
| input_ms.select_corr | [0,1,2,3] | |
| input_model.recipe | MODEL_DATA | |
| input_model.source_chunks | 5 | |
| solver.terms | [K, G] | |
| solver.iter_recipe | [50,50,50,50] | |
| solver.products | [corrected_data, corrected_weight] | |
| solver.columns | [CORRECTED_DATA, WEIGHT_SPECTRUM] | |
| K.type | delay | |
| K.time_interval | 1 | |
| K.freq_interval | 0 | |
| G.type | complex | |
| G.time_interval | 0 \|30\|60 | |
| G.freq_interval | 1 | |

Table A.3: killMS parameters. Columns: parameter, value, notes. I used the default values except for those stated below.

| Parameter | Value | Notes |
|---|---|---|
| –ImageSkyModel-BaseImageName | Base name of final 2GC DDFacet outputs | Ensures all corresponding parameters are set to mirror that of DDFacet |
| –Solutions-OutSolsName | DD0 | |
| –Solvers-SolverType | KAFCA | |
| –Solvers-dt | 5 | |
| –Solvers-NChanSols | 10 | |

Table A.4: DDFacet parameters. Columns: parameter, value, notes. I used the default values except for those stated below.

| Parameter | Value | Notes |
|---|---|---|
| –Data-ColName | CORRECTED_DATA or Subtracted data | Depending on which is be to imaged |
| –Data-ChunkHours | 1 | MACS J1115.8+0129: 0.25 due to higher dump rate |
| –Predict-InitDicoModel | previous DicoModel | First run: None |
| –Selection-UVRangeKm | [0:2000] | HR imaging: [uvcut:2000] |
| –Output-Mode | Predict | Only when re-predicting the HR subtraction model |
| –Output-Name | name | |
| –Output-Cubes | all | Spectral analysis only |
| –Output-Images | all | |
| –Image-NPix | 6000 | |
| –Image-Cell | 1.5 | |
| –Facets-NFacets | 20 | |
| –Facets-CatNodes | clustering file outputted by `MakeModel.py` | |
| –Facets-DiamMax | 0.1265625 | |
| –Facets-DiamMin | 0.01265625 | |
| –Weight-Briggs | -2 | HR imaging only |
| –Weight-EnableSigmoidTaper | 1 | Spectral analysis only |
| –Weight-SigmoidTaperInnerCutoff | ~ 700 | Spectral analysis only Equivalent to 5-6’ |
| –Weight-SigmoidTaperOuterCutoff | ~ 17000 | Spectral analysis only Equivalent to 14-15” |
| –Weight-SigmoidTaperInnerRolloff Strength | 1 | Spectral analysis only |
| –Weight-SigmoidTaperOuterRolloff Strength | 1 | Spectral analysis only |
| –Parallel-NCPU | 50 | |
| –Cache-Reset | 0 | First run: 1 |
| –Cache-PSF | force | First run: auto |
| –Cache-Dirty | forceresidual | First run: auto |
| –Beam-Model | FITS | |
| –Beam-NBand | 10 | |
| –Beam-CenterNorm | 1 | |
| –Beam-Smooth | 1 | |
| –Beam-FITSFile | `eidos` primary beam models | |
| –Beam-FITSFeed | xy | |

Table A.5: DDFacet parameters continued. Columns: parameter, value, notes. I used the default values except for those stated below.

| Parameter | Value | Notes |
|---|---|---|
| –BeamFITSFeedSwap | True | |
| –Beam-FITSParAngleIncDeg | 0.5 | |
| –Beam-ApplyPJones | 1 | |
| –Beam-FlipVisibilityHands | 1 | |
| –Freq-NBand | 10 | Spectral analysis: 3 |
| –Freq-NDegridBand | 15 | Spectral analysis: 6 |
| –DDESolutions-DDSols | DD0 | None if imaging at 2GC |
| –Deconv-Mode | SSD2 | |
| –Deconv-MaxMajorIter | 1 | First run: 2 |
| –Deconv-RMSFactor | 3.0 | |
| –Deconv-PeakFactor | 0.01 | |
| –Deconv-NumRMSSamples | 0 | |
| –Mask-External | `breizorro` mask derived from previous run | First run: None |
| –Mask-Auto | False | First run: True |
| –Mask-SigTh | 5 | HR imaging: 3 |
| –SSD2-PolyFreqOrder | 4 | Spectral analysis: 3 |

# Bibliography

Abolfathi B., et al., 2018, , 235, 42

Ackermann M., et al., 2014, , 787, 18

Ahnen M. L., et al., 2016, , 589, A33

Andrade-Santos F., et al., 2017, , 843, 76

Asad K. M. B., et al., 2021, , 502, 2970

Ascasibar Y., Markevitch M., 2006, , 650, 102

Becker R. H., White R. L., Helfand D. J., 1995, , 450, 559

Biava N., et al., 2021, , 508, 3995

Biava N., Brienza M., Bonafede A., Gitti M., 2022, in 44th COSPAR Scientific Assembly. Held 16-24 July. p. 2330

Boch T., Fernique P., 2014, in Manset N., Forshay P., eds, Astronomical Society of the Pacific Conference Series Vol. 485, Astronomical Data Analysis Software and Systems XXIII. p. 277

Bonafede A., et al., 2014, , 444, L44

Bonafede A., et al., 2022, , 933, 218

Bonnarel F., et al., 2000, , 143, 33

Botteon A., Gastaldello F., Brunetti G., 2018, , 476, 5591

Botteon A., et al., 2020, , 499, L11

Bradley L. D., et al., 2014, , 792, 76

Bridle A. H., Schwab F. R., 1999, in Taylor G. B., Carilli C. L., Perley R. A., eds, Astronomical Society of the Pacific Conference Series Vol. 180, Synthesis Imaging in Radio Astronomy II. p. 371

Briggs D. S., 1995, in American Astronomical Society Meeting Abstracts. p. 112.02

Brüggen M., Bykov A., Ryu D., Röttgering H., 2012, , 166, 187

Brunetti G., Jones T. W., 2014, International Journal of Modern Physics D, 23, 1430007

Brunetti G., Setti G., Feretti L., Giovannini G., 2001, , 320, 365

Camilo F., et al., 2018, , 856, 180

Carilli C. L., Perley R. A., Dreher J. W., Leahy J. P., 1991, , 383, 554

Cassano R., Brunetti G., Setti G., Govoni F., Dolag K., 2007, , 378, 1565

Cassano R., et al., 2013, , 777, 141

Chambers K. C., et al., 2016, arXiv e-prints, p. arXiv:1612.05560

Clark B. G., 1980, , 89, 377

Condon J. J., Cotton W. D., Greisen E. W., Yin Q. F., Perley R. A., Taylor G. B., Broderick J. J., 1998, , 115, 1693

Conway J. E., Cornwell T. J., Wilkinson P. N., 1990, , 246, 490

Di Gennaro G., et al., 2021, Nature Astronomy, 5, 268

Dolag K., Enßlin T. A., 2000, , 362, 151

Donnert J., Dolag K., Brunetti G., Cassano R., Bonafede A., 2010a, , 401, 47

Donnert J., Dolag K., Cassano R., Brunetti G., 2010b, , 407, 1565

Donnert J., Dolag K., Brunetti G., Cassano R., 2013, , 429, 3564

Donnert J., Vazza F., Brüggen M., ZuHone J., 2018, , 214, 122

Ebeling H., Edge A. C., Mantz A., Barrett E., Henry J. P., Ma C. J., van Speybroeck L., 2010, , 407, 83

F.R.S. L. R., 1879, The London, Edinburgh, and Dublin Philosophical Magazine and Journal of Science, 8, 261

F.R.S. J. L. D., 1897, The London, Edinburgh, and Dublin Philosophical Magazine and Journal of Science, 44, 503

Feretti L., Giovannini G., Govoni F., Murgia M., 2012, , 20, 54

Forman W., Jones C., 1982, , 20, 547

Fruscione A., et al., 2006, in Silva D. R., Doxsey R. E., eds, Society of Photo-Optical Instrumentation Engineers (SPIE) Conference Series Vol. 6270, Society of Photo-Optical Instrumentation Engineers (SPIE) Conference Series. p. 62701V, doi:10.1117/12.671760

Gendron-Marsolais M., et al., 2017, , 469, 3872

Giacintucci S., Markevitch M., Venturi T., Clarke T. E., Cassano R., Mazzotta P., 2014a, , 781, 9

Giacintucci S., Markevitch M., Brunetti G., ZuHone J. A., Venturi T., Mazzotta P., Bourdin H., 2014b, , 795, 73

Giacintucci S., Markevitch M., Cassano R., Venturi T., Clarke T. E., Brunetti G., 2017, , 841, 71

Giacintucci S., Markevitch M., Cassano R., Venturi T., Clarke T. E., Kale R., Cuciti V., 2019, , 880, 70

Giovannini G., et al., 2020, , 640, A108

Gitti M., et al., 2015, in Advancing Astrophysics with the Square Kilometre Array (AASKA14). p. 76 (arXiv:1412.5664)

Gitti M., Brunetti G., Cassano R., Ettori S., 2018, , 617, A11

Govoni F., Feretti L., 2004, International Journal of Modern Physics D, 13, 1549

Govoni F., Enßlin T. A., Feretti L., Giovannini G., 2001, , 369, 441

Govoni F., Murgia M., Markevitch M., Feretti L., Giovannini G., Taylor G. B., Carretti E., 2009, , 499, 371

Grobler T. L., Nunhokee C. D., Smirnov O. M., van Zyl A. J., de Bruyn A. G., 2014, Monthly Notices of the Royal Astronomical Society, 439, 4030

Hamaker J. P., Bregman J. D., Sault R. J., 1996, , 117, 137

Harwood J. J., Hardcastle M. J., Croston J. H., Goodger J. L., 2013, Monthly Notices of the Royal Astronomical Society, 435, 3353

Harwood J. J., Hardcastle M. J., Croston J. H., 2015, Monthly Notices of the Royal Astronomical Society, 454, 3403

Högbom J. A., 1974, , 15, 417

Hubble E. P., 1926, , 64, 321

Hugo B. V., Perkins S., Merry B., Mauch T., Smirnov O. M., 2022, arXiv e-prints, p. arXiv:2206.09179

Ignesti A., 2022, , 92, 101732

Ignesti A., Brunetti G., Gitti M., Giacintucci S., 2020, , 640, A37

Ignesti A., et al., 2022, , 659, A20

Intema H. T., van der Tol S., Cotton W. D., Cohen A. S., van Bemmel I. M., Röttgering H. J. A., 2009, , 501, 1185

Jacob S., Pfrommer C., 2017a, , 467, 1449

Jacob S., Pfrommer C., 2017b, , 467, 1478

Johnston-Hollitt M., et al., 2015, in Advancing Astrophysics with the Square Kilometre Array (AASKA14). p. 92 (arXiv:1506.00808)

Jonas J., MeerKAT Team 2016, in MeerKAT Science: On the Pathway to the SKA. p. 1

Jones R. C., 1941, J. Opt. Soc. Am., 31, 488

Józsa G. I. G., et al., 2020, CARACal: Containerized Automated Radio Astronomy Calibration pipeline (ascl:2006.014)

Julier S. J., Uhlmann J. K., 1997, in Kadar I., ed., Society of Photo-Optical Instrumentation Engineers (SPIE) Conference Series Vol. 3068, Signal Processing, Sensor Fusion, and Target Recognition VI. pp 182–193, doi:10.1117/12.280797

Kale R., Parekh V., 2016, , 459, 2940

Kale R., Shende K. M., Parekh V., 2019, , 486, L80

Kalman R. E., 1960, Journal of Basic Engineering, 82, 35

Katz-Stone D. M., Rudnick L., 1997, , 479, 258

Katz-Stone D. M., Rudnick L., Anderson M. C., 1993, , 407, 549

Kenyon J. S., Smirnov O. M., Grobler T. L., Perkins S. J., 2018, , 478, 2399

Knowles K., et al., 2016, , 459, 4240

Knowles K., et al., 2022, , 657, A56

Kokotanekov G., Wise M. W., de Vries M., Intema H. T., 2018, , 618, A152

Kreutz-Delgado K., 2009, arXiv e-prints, p. arXiv:0906.4835

Laganá T. F., Durret F., Lopes P. A. A., 2019, , 484, 2807

Large M. I., Mathewson D. S., Haslam C. G. T., 1959, , 183, 1663

Leccardi A., Rossetti M., Molendi S., 2010, , 510, A82

Makhathini S., 2018, PhD thesis, Rhodes University, Drosty Rd, Grahamstown, 6139, Eastern Cape, South Africa

Markevitch M., Vikhlinin A., 2007, , 443, 1

Mauch T., et al., 2020, , 888, 61

Maughan B. J., Giles P. A., Randall S. W., Jones C., Forman W. R., 2012, , 421, 1583

Mazzotta P., Giacintucci S., 2008, , 675, L9

McDonald M., et al., 2017, , 843, 28

McMullin J. P., Waters B., Schiebel D., Young W., Golap K., 2007, in Shaw R. A., Hill F., Bell D. J., eds, Astronomical Society of the Pacific Conference Series Vol. 376, Astronomical Data Analysis Software and Systems XVI. p. 127

Medezinski E., Umetsu K., Okabe N., Nonino M., Molnar S., Massey R., Dupke R., Merten J., 2016, , 817, 24

Messier C., 1781, Catalogue des Nébuleuses et des Amas d'Étoiles (Catalog of Nebulae and Star Clusters), Connoissance des Temps ou des Mouvements Célestes, for 1784, p. 227-267

Noordam J. E., Smirnov O. M., 2010, , 524, A61

Offringa A. R., Smirnov O., 2017, , 471, 301

Offringa A. R., et al., 2014, , 444, 606

Osinga E., et al., 2022, , 665, A71

Pandey-Pommier M., Richard J., Combes F., Edge A., Guiderdoni B., Narasimha D., Bagchi J., Jacob J., 2016, in Reylé C., Richard J., Cambrésy L., Deleuil M., Pécontal E., Tresse L., Vauglin I., eds, SF2A-2016: Proceedings of the Annual meeting of the French Society of Astronomy and Astrophysics. pp 367–372 (arXiv:1612.00225)

Pasini T., et al., 2022, , 663, A105

Pearce C. J. J., et al., 2017, , 845, 81

Pearson T. J., Readhead A. C. S., 1984, , 22, 97

Perley R. A., Butler B. J., 2017, , 230, 7

Pfrommer C., Enßlin T. A., 2004, , 413, 17

Pfrommer C., Enßlin T. A., Springel V., 2008, , 385, 1211

Piffaretti R., Arnaud M., Pratt G. W., Pointecouteau E., Melin J. B., 2011, , 534, A109

Pinzke A., Oh S. P., Pfrommer C., 2017, , 465, 4800

Planck Collaboration et al., 2014, , 571, A29

Raja R., et al., 2020, , 493, L28

Rajpurohit K., et al., 2021a, , 646, A56

Rajpurohit K., et al., 2021b, , 654, A41

Rajpurohit K., et al., 2022, arXiv e-prints, p. arXiv:2209.03288

Richard-Laferrière A., et al., 2020, , 499, 2934

Riseley C. J., et al., 2022a, , 512, 4210

Riseley C. J., et al., 2022b, , 515, 1871

Ruszkowski M., Oh S. P., 2010, , 713, 1332

Rybicki G. B., Lightman A. P., 1986, Radiative Processes in Astrophysics

Sault R. J., Conway J. E., 1999, in Taylor G. B., Carilli C. L., Perley R. A., eds, Astronomical Society of the Pacific Conference Series Vol. 180, Synthesis Imaging in Radio Astronomy II. p. 419

Savini F., et al., 2018, , 478, 2234

Savini F., et al., 2019, , 622, A24

Schwab F. R., 1984, , 89, 1076

Sikhosana S. P., Knowles K., Hilton M., Moodley K., Murgia M., 2022, arXiv e-prints, p. arXiv:2207.05492

Smirnov O. M., 2011a, , 527, A106

Smirnov O. M., 2011b, , 527, A107

Smirnov O. M., 2011c, , 527, A108

Smirnov O. M., 2011d, , 531, A159

Smirnov O. M., Tasse C., 2015, , 449, 2668

Sob U. M., Bester H. L., Smirnov O. M., Kenyon J. S., Grobler T. L., 2019, Monthly Notices of the Royal Astronomical Society, 491, 1026

Tasse C., 2014a, arXiv e-prints, p. arXiv:1410.8706

Tasse C., 2014b, , 566, A127

Tasse C., et al., 2018, , 611, A87

Taylor G. B., Fabian A. C., Allen S. W., 2002, , 334, 769

Timmerman R., van Weeren R. J., McDonald M., Ignesti A., McNamara B. R., Hlavacek-Larrondo J., Röttgering H. J. A., 2021, , 646, A38

Trehaeven K. S., et al., 2023, , 520, 4410

Vazza F., Brunetti G., Brüggen M., Bonafede A., 2018, , 474, 1672

Vazza F., Wittor D., Brunetti G., Brüggen M., 2021, , 653, A23

Venturi T., Giacintucci S., Brunetti G., Cassano R., Bardelli S., Dallacasa D., Setti G., 2007, , 463, 937

Venturi T., et al., 2017, , 603, A125

Wan E., Van Der Merwe R., 2000, in Proceedings of the IEEE 2000 Adaptive Systems for Signal Processing, Communications, and Control Symposium (Cat. No.00EX373). pp 153–158, doi:10.1109/ASSPCC.2000.882463

Wijnholds S. J., Grobler T. L., Smirnov O. M., 2016, Monthly Notices of the Royal Astronomical Society, 457, 2331

Willson M. A. G., 1970, , 151, 1

Wirtinger W., 1927, Mathematische Annalen, 97, 357

Yatawatta S., Zaroubi S., de Bruyn G., Koopmans L., Noordam J., 2008, arXiv e-prints, p. arXiv:0810.5751

Yu H., et al., 2018, , 853, 100

Zernike F., 1938, Physica, 5, 785

ZuHone J., Su Y., 2022, arXiv e-prints, p. arXiv:2202.06712

ZuHone J. A., Markevitch M., Brunetti G., Giacintucci S., 2013, , 762, 78

ZuHone J. A., Brunetti G., Giacintucci S., Markevitch M., 2015, , 801, 146

de Gasperin F., et al., 2022, , 659, A146

de Villiers M. S., Cotton W. D., 2022, , 163, 135

van Weeren R. J., de Gasperin F., Akamatsu H., Brüggen M., Feretti L., Kang H., Stroe A., Zandanel F., 2019, , 215, 16